

Diss. ETH No. 15903

# NUMERICAL SIMULATION OF DISPERSE TWO-PHASE FLOWS

- I. Settling and Break-up of Suspension Drops
- II. Particle Settling in Homogeneous Turbulence

A dissertation submitted to the  
SWISS FEDERAL INSTITUTE OF TECHNOLOGY  
ZÜRICH  
for the degree of  
Doctor of Technical Sciences

presented by

Thorsten Bosse

Dipl.-Ing., University of Karlsruhe  
born on March 2, 1973  
citizen of Germany

accepted on the recommendation of

Prof. Dr. L. Kleiser, examiner  
Prof. Dr. E. Meiburg, co-examiner  
Dr. habil. C. Härtel, co-examiner

Hartung-Gorre Verlag Konstanz, Germany

2005

Reprint of Diss. ETH No. 15903

**Bibliographic Information published by  
Die Deutsche Bibliothek**

Die Deutsche Bibliothek lists this publication in the Deutsche Nationalbibliografie; detailed bibliographic data is available in the internet at <<http://dnb.ddb.de>>.

Copyright © 2005 by Thorsten Bosse

First edition 2005

HARTUNG-GORRE VERLAG KONSTANZ/Germany

ISBN 3-86628-002-5

# Abstract

This dissertation is concerned with the numerical investigation of particle-laden flows. The simulations are based on a pseudo-spectral method to solve the fluid equations combined with a Lagrangian point-particle model for the particulate phase (Eulerian–Lagrangian approach). Two flow configurations of increasing complexity are studied with the aim of unraveling some fundamental properties of particle settling in disperse two-phase flows.

The first configuration is a suspension drop (initially spherical swarm of particles) settling in a fluid under the influence of gravity. The focus is on a range of moderate drop Reynolds numbers  $1 \leq Re_d \leq 100$  where the suspension drop deforms into a torus that eventually becomes unstable and breaks up into a number of secondary blobs. The flow remains laminar, which allows for a systematic variation of several parameters. The influence of the Reynolds number, the number of particles inside the drop, the initial particle positions and some numerical quantities are studied in detail.

The second configuration is an initially random suspension of particles in homogeneous turbulence. Here, the focus is on the enhancement of the mean particle settling velocity in a turbulent carrier fluid compared to the settling velocity of a single particle in still fluid. Results are presented for both one-way coupling (the fluid flow is not affected by the presence of the particles) and two-way coupling (the particles exert a feedback force on the fluid). The mechanism responsible for an additional increase in settling velocity in the case of two-way coupling is analyzed. Moreover, a careful comparison with recent experimental results is performed for a microscale Reynolds number  $Re_\lambda = 75$  of the turbulent carrier fluid.

# Kurzfassung

Die vorliegende Dissertation befasst sich mit der numerischen Simulation von partikelbeladenen Strömungen. In den Simulationen wird eine Pseudospektralmethode für die Lösung der Fluidströmungsgleichungen verwendet. Die Partikel werden als punktförmige Massen modelliert und individuell im Lagrange'schen Sinn auf ihrem Weg durch das Trägerfluid verfolgt (Euler–Lagrange–Verfahren). Zwei Strömungskonfigurationen von zunehmender Komplexität werden untersucht mit dem Ziel,

grundlegende Eigenschaften des Absinkens von Partikeln in dispersen Zweiphasenströmungen zu erklären.

Im ersten Fall wird das Absinken eines Suspensionstropfens, d. h. einer zu Beginn kugelförmigen Ansammlung von Partikeln, unter dem Einfluss der Gravitation simuliert. Der Schwerpunkt der Untersuchung liegt auf einem Bereich von moderaten Tropfen-Reynoldszahlen  $1 \leq Re_d \leq 100$ , in dem der Suspensionstropfen sich gewöhnlich in einen Torus verformt, der beim weiteren Absinken instabil wird und schließlich in mehrere sekundäre Tropfen aufbricht. Die Strömung bleibt dabei laminar, wodurch der Rechenaufwand entsprechend beschränkt ist und eine systematische Variation von mehreren Parametern erlaubt. Im Speziellen wird die Abhängigkeit von der Reynoldszahl, der Anzahl der Partikel im Tropfen, der Partikelpositionen zu Beginn der Rechnung und einigen numerischen Einflussgrößen untersucht.

Im zweiten Fall wird eine Suspension von zu Beginn zufallsverteilten Partikeln in einem homogen turbulenten Strömungsfeld betrachtet. Das Interesse richtet sich hier auf die Erhöhung der mittleren Partikelsinkgeschwindigkeit in turbulenter Strömung, verglichen mit der Sinkgeschwindigkeit eines einzelnen Partikels in ruhendem Fluid. Ergebnisse werden präsentiert für die Fälle der Einweg-Kopplung, bei der das Fluid von den Partikeln unbeeinflusst bleibt, und der Zweiweg-Kopplung, bei der die Partikel eine auf das Fluid rückwirkende Kraft ausüben. Der Mechanismus, der zu einer zusätzlichen Erhöhung der Sinkgeschwindigkeit in letzterem Fall führt, wird analysiert. Außerdem wird ein Vergleich der Ergebnisse mit neueren experimentellen Daten aus der Literatur für eine Reynoldszahl basierend auf dem Taylor-Mikromaß von  $Re_\lambda = 75$  vorgenommen.

## Acknowledgements

Prof. Leonhard Kleiser has guided me as a supervisor throughout my PhD project at the Institute of Fluid Dynamics (IFD). I would like to express my sincere thanks to him for his constant support and for putting a lot of confidence in me and my work.

My special thanks go to Dr. habil. Carlos Härtel for numerous fruitful and very instructive discussions, particularly at the beginning of my research. He has always been available for me – even after he had left our research group at the IFD – and finally acted as a co-examiner of my dissertation. His comments on my publications have been very helpful.

Prof. Eckart Meiburg is the third person I am especially indebted to. He has provided me with the wonderful opportunity to spend almost five months as a visiting researcher in his group at the University of California at Santa Barbara (UCSB). This was a great experience for me not only professionally but also personally. During my research visit we had many in-depth discussions that helped me a lot in defining the further course and objectives of my project. Prof. Meiburg also acted as a co-examiner of my dissertation.

My time as a PhD student in Zurich would have been much less interesting and satisfying without all my friends. To name just a few, I would like to give my thanks to Uli, Holger, Franzi, Felix (thanks for proof-reading!), Andri, Conni, Axel, Dirk, Katrin, Nanna, Grit, Yvonne, Vanessa, Tjarko, and Arne the artist.

Last not least, I am grateful to F. C. for helping me to once in a while step beyond the obvious and feel the beauty of it all.

This work was supported by the ETH research grant (TH-Forschungsgesuch) 18/2000–1. Additional financial support for the research visit in Prof. Meiburg's group at UCSB was provided by an ETH-UCSB scholarship. Simulations were performed at the Swiss National Supercomputing Centre (CSCS) at Manno, Switzerland.

Zürich, December 2004

Thorsten Bosse

# Contents

---

<b>Nomenclature</b>	<b>III</b>	
<b>1</b>	<b>Introduction</b>	<b>1</b>
1.1	Simulation of particle–laden flows . . . . .	1
1.2	Objectives and outline . . . . .	4
1.2.1	Settling and break–up of suspension drops . . . . .	5
1.2.2	Particle settling in homogeneous turbulence . . . . .	6
<b>2</b>	<b>Simulation approach</b>	<b>11</b>
2.1	Governing equations . . . . .	11
2.1.1	Particle equations . . . . .	11
2.1.2	Fluid equations . . . . .	13
2.2	Numerical method . . . . .	14
2.2.1	Discretization and time integration . . . . .	14
2.2.2	Two–way coupling and interpolation . . . . .	16
2.2.3	Computational particles . . . . .	17
2.3	Dimensionless parameters . . . . .	19
2.3.1	Suspension drops . . . . .	19
2.3.2	Particle settling in homogeneous turbulence . . . . .	20
2.4	Forcing of stationary turbulence . . . . .	23
2.4.1	Implementation . . . . .	23
2.4.2	Validation . . . . .	25
<b>3</b>	<b>Settling and break–up of suspension drops</b>	<b>31</b>
3.1	Low Reynolds numbers ( $Re_d \ll 1$ ) . . . . .	32
3.2	Moderate Reynolds numbers ( $1 \leq Re_d \leq 100$ ) . . . . .	37
3.2.1	Reynolds number dependence . . . . .	37
3.2.2	Influence of the initial particle distribution . . . . .	47
3.2.3	Influence of the number of particles . . . . .	50
3.2.4	Influence of the periodic boundaries . . . . .	54
3.2.5	Influence of interpolation . . . . .	56
3.2.6	Influence of the grid resolution . . . . .	57
3.2.7	Spectral analysis of settling drop and torus . . . . .	58

<b>4 Particle settling in homogeneous turbulence</b>	<b>65</b>
4.1 One-way coupling . . . . .	66
4.2 Two-way coupling . . . . .	74
4.3 Comparison with experimental data . . . . .	89
<b>5 Summary and conclusions</b>	<b>95</b>
<b>A Time stepping procedure</b>	<b>99</b>
A.1 RK3CN scheme . . . . .	99
A.2 RK3 scheme . . . . .	100
A.3 Stability criterion for time step . . . . .	101
<b>B Interpolation</b>	<b>103</b>
<b>C Determination of forcing parameters</b>	<b>105</b>
<b>D Definitions of turbulent quantities</b>	<b>107</b>
<b>E Settling of single particles</b>	<b>111</b>
<b>Bibliography</b>	<b>117</b>
<b>Curriculum vitae</b>	<b>126</b>

# Nomenclature

---

## Roman symbols

$A_s$	amplitude of initial radial particle shift
$c$	drop volume fraction
$d$	particle diameter
$D(k)$	three-dimensional dissipation spectrum
$D_c$	global “dispersion function”
$E(k)$	three-dimensional energy spectrum
$E_{11}(k_1)$	one-dim. longitudinal spectrum in direction 1
$E_{22}(k_2)$	one-dim. longitudinal spectrum in direction 2
$E_{33}(k_3)$	one-dim. longitudinal spectrum in direction 3
$f_i^{(p)}$	two-way coupling term (particle feedback force)
$\hat{\mathbf{f}}, \hat{\mathbf{f}}_k$	Fourier coefficient of two-way coupling term
$F_{i,j}^{(p)}$	feedback force of particle $j$
$Fr$	Froude number
$Fr_d$	Froude number based on drop properties
$g_i, \mathbf{g}, g$	gravitational acceleration, magnitude
$\mathbf{k}_i, \mathbf{k}, k$	wavenumber vector, magnitude
$k_0, k_{max}$	magnitude of smallest and largest wavenumber
$K_F$	upper bound of forced wavenumber band
$l_e$	eddy length scale
$l_I$	integral length scale
$l_s$	number of periods in circumferential direction
$L$	side length of computational box
$L_{ref}$	reference length
$m_f$	mass of fluid displaced by a particle
$m_p$	particle mass
$M$	ratio of real to computational particles
$\mathbf{n}_i, \mathbf{n}$	integer wavenumber vector
$n_p^c$	number of computational particles
$n_p^r$	number of real particles
$n_p^b$	local number of particles (per grid cell)
$N$	number of grid points in each spatial direction
$N_b$	number of boxes/grid cells within comput. domain
$p, p^{(m)}$	pressure, modified pressure
$\hat{p}$	Fourier coefficient of pressure

---

$P_c$	probability function of particle distribution
$P_{binom}$	probability function of binomial distribution
$q$	total turbulent kinetic energy
$q_i$	kinetic energy associated with velocity component $i$
$r$	particle radius
$r_i, \mathbf{r}$	radial distance from the particle center
$R$	initial suspension drop radius
$R_p^m$	mean particle distance from the center of mass
$Re_d$	drop Reynolds number
$Re_f$	forcing Reynolds number
$Re_p$	particle Reynolds number
$Re_T$	turbulence Reynolds number
$Re_\lambda$	Taylor microscale Reynolds number
$s_i, \mathbf{s}, \hat{\mathbf{s}}_k$	vector of nonlinear terms in NS equation
$St$	Stokes number
$St_d$	Stokes number based on drop properties
$St_\eta$	Stokes number based on particle properties and Kolmogorov time
$t$	time
$t_e$	eddy turnover time
$t_{e,0}$	eddy turnover time for one-way coupling
$t_I$	integral time scale
$t_\eta$	Kolmogorov time
$T_{d-t}$	time required for drop to deform into torus
$T_L$	forcing time scale
$T_{ref}$	reference time
$u_i, \mathbf{u}$	fluid velocity
$\hat{u}_i, \hat{\mathbf{u}}, \hat{\mathbf{u}}_k$	Fourier coefficients of fluid velocity
$\tilde{u}_i$	fluid velocity of undisturbed flow
$u_L$	solution of Ornstein–Uhlenbeck process
$u_\eta$	Kolmogorov velocity
$u'$	fluid root-mean-square (RMS) velocity
$U_d$	characteristic drop settling velocity
$U_p$	Stokes settling velocity of a single particle
$U_{ref}$	reference velocity
$U_t$	terminal velocity of single particle or bubble
$V_3$	particle settling velocity averaged over all particles and time
$v_d$	drop settling velocity

---

$v_d^0$	drop settling velocity in infinite fluid
$v_i$	particle velocity
$V_c$	grid cell volume
$V_p$	particle volume
$V_{pc}$	ratio of particle volume to grid cell volume
$w_i$	relative velocity between particle and fluid
$w_{i,j}$	weighting factor for particle $j$ in direction $i$
$x_i, \mathbf{x}$	position vector (grid points)
$Y_i$	particle position

### Greek symbols

$\delta_{ij}$	Kronecker symbol
$\delta(x)$	Dirac delta function
$\Delta r$	initial particle shift in $(x_1, x_2)$ -plane
$\Delta V_3$	increase of mean particle settling velocity
$\Delta x_i$	grid spacing in direction $i$
$\epsilon$	energy dissipation rate
$\epsilon_L$	forcing parameter
$\epsilon$	ratio of particle radius to drop radius
$\epsilon_{ijk}$	permutation symbol
$\eta$	Kolmogorov length
$\theta$	azimuthal angle in $(x_1, x_2)$ -plane
$\lambda$	Taylor microscale
$\mu$	dynamic viscosity
$\nu$	kinematic viscosity
$\xi(t)$	standardized Gaussian variable
$\varrho$	fluid density
$\varrho_p$	particle density
$\bar{\varrho}$	mean suspension drop (bulk) density
$\Phi_m$	overall particle mass loading
$\Phi_v$	overall particle volume fraction
$\Phi_v^l$	local particle volume fraction
$\sigma$	standard deviation
$\tau$	characteristic fluid time scale
$\tau_p$	particle response time
$\omega_i$	vorticity
$\Omega$	scalar vorticity

## Other symbols

$\Re[\cdot]$ , $\Im[\cdot]$	real, imaginary part
$\langle \cdot \rangle$	average over all particles

## Subscripts

$\cdot_c$	concentration
$\cdot_d$	drop
$\cdot_f$	forcing
$\cdot_i$	spatial direction
$\cdot_p$	particle
$\cdot_s$	initial shift

## Superscripts

$\cdot^b$	box, grid cell
$\cdot^l$	local
$\cdot^{(p)}$	particle feedback force
$\cdot^T$	transpose
$\cdot^{(0)}$	initial value
$\overline{(\cdot)}$	mean (space- and/or time-averaged) quantity
$\cdot^{(\square)}$	top hat function
$\cdot^{(\wedge)}$	tent function

## Abbreviations

AL	Aliseda <i>et al.</i> (2002)
BS	forcing by backscaling scheme
CFD	computational fluid dynamics
CUB	cubic Lagrangian polynomial
DNS	direct numerical simulation
ESPO	Eswaran & Pope (1988)
HIT	homogeneous isotropic turbulence (name of computer code developed in the work presented)
LIN	linear interpolation
N&B	Nitsche & Batchelor (1997)
NS	Navier–Stokes (equation)
OU	Ornstein Uhlenbeck (process)

RMS

root mean square

SPE

spectral summation (interpolation)

W&M

Wang & Maxey (1993)

# Chapter 1

---

## Introduction

### 1.1 Simulation of particle-laden flows

The research work presented in this dissertation is concerned with the numerical simulation of particle-laden flows. These flows are usually denoted as disperse two-phase flows, since they contain a discontinuous phase distributed throughout the flowing medium. In general, the dispersed phase may assume the form of small solid particles, droplets, or bubbles and the carrier fluid can be a liquid or a gas.

Disperse two-phase flows are encountered in a variety of natural processes and engineering applications. In fact, taking a closer look at the natural occurrences of flows of all kinds reveals that most of these involve more than a single phase. Examples range from large-scale phenomena, such as dust particle transport in the atmosphere or particle sedimentation in river beds, to small-scale phenomena such as atherosclerotic deposits in human blood vessels. Engineering applications are numerous in the pharmaceutical and chemical industries including mixing, drying, and transport processes.

This wide variety of occurrences and applications makes two-phase flows an active field of current scientific endeavors in both academic and industrial research. Compared to single-phase flows involving pure fluids, the additional difficulty in treating multiphase flows arises from the interaction between the different phases. In general, this interaction involves the mutual exchange of mass, momentum, and energy. For example, during the expansion of the compressed steam in a steam turbine the water may start condensing out into small water droplets. In this process the condensation energy is released into the carrier fluid, i. e. an energy transfer occurs between the phases. Also, the droplets may grow due to further condensation on their way through the turbine, which involves a mass transfer between the liquid and the gaseous phase. The dynamical interplay between the carrier fluid and the droplets that are carried along with the flow is the consequence of a mutual exchange of momentum. A thorough understanding of these phenomena is important from a practical point of view, since the water droplets may hit the

turbine blades leading to severe corrosion and a decrease in the overall efficiency of the process.

The enhanced complexity of multiphase flow systems makes their numerical treatment particularly challenging. With the growing availability of powerful computer resources within the last few decades numerical simulations have come into reach as a valuable tool in predicting fluid flows of practical interest. The theoretical foundations, on the other hand, reach back as far as to the nineteenth century. For example, in 1851 Stokes published his famous article on the creeping flow around a rigid sphere (Stokes, 1851). A number of particle models are based on this so-called Stokes solution or, at least, incorporate as a key feature the drag force on the sphere derived from this solution. Within the field of computational fluid dynamics (CFD) the study of multiphase flows, however, is a relatively young branch. The reason for this is that the difficulties arising from the interaction of the different phases, as illustrated above, have to be tackled in addition to all other obstacles faced in the numerical treatment of single-phase flows. This makes the simulation of multiphase systems including particle-laden flows especially cumbersome and computationally expensive.

Nevertheless, great efforts have been directed towards developing numerical methods for the simulation of disperse two-phase flows. These methods are usually designed for specific classes of particle-laden flows depending on the flow configuration and the parameters, such as the size, the form and the number of the particles, the flow regime being laminar or turbulent, or the properties of the carrier fluid being compressible or incompressible. *Direct (fully resolved) numerical simulations* aim at resolving the flow field around the dispersed phase and treat the particles as (moving) boundaries to the fluid, see e.g. Hu (1996), Hu *et al.* (2001), Pan *et al.* (2001), Glowinski *et al.* (2001), Glowinski (2003). This approach, however, is limited to relatively small numbers of particles.

Examples in which larger numbers of particles can be simulated – often based on some averaging technique applied to the ensemble of particles – include the *trajectory approach* (Crowe *et al.* (1977), Kohnen *et al.* (1994), Elghobashi & Truesdell (1992)) and the *two-fluid formulation* (Simonin *et al.* (1993), Elghobashi & Druzhinin (1998)). The former methodology tracks the individual particles in a Lagrangian manner, whereas in the latter the particulate phase is considered a second fluid, to which numerical techniques for continuous media are applied.

The strict mathematical derivation of the governing equations for

such two-phase flows has been accomplished by different authors (e.g. Drew (1983), Drew & Lahey Jr (1993), Zhang & Prosperetti (1997), Prosperetti (1997)) and usually results in a closure problem due to the unavoidable averaging of certain phase properties. To date there are no generally valid constitutive relations available to close these equations. Thus, one has to resort to further simplifications or different principal approaches.

For the case of creeping flow conditions around the particles, *Stokesian dynamics* simulations have successfully been performed (Brady & Bossis (1988), Durlowsky & Brady (1989)). As an alternative to classical simulation methods based on the Navier–Stokes equations *Discrete or Lattice Boltzmann methods (LBM)* have emerged as a powerful technique for the computational modeling of a wide variety of flow problems including multiphase flow in complex geometries (Shan & Chen (1993), Chen & Doolen (1998)). These methods are based on a simplified Boltzmann equation and naturally accommodate a variety of boundary conditions such as the pressure drop across the interface between two fluids and wetting effects at a fluid-solid interface. LBM have successfully been applied to the prediction of particulate flows by a number of researchers, e.g. Ladd (1994a), Ladd (1994b), Aidun & Lu (1995), Behrend (1995).

A variant of the Eulerian approach for the particulate phase was recently proposed by Balachandar and co-workers (Ferry & Balachandar (2001), Ferry *et al.* (2003), Rani & Balachandar (2004)). For particles with a small response time  $\tau_p$  compared to a characteristic fluid time scale, the particle velocity field is expressed as an expansion in  $\tau_p$ . This so-called equilibrium Eulerian method avoids the need to solve additional partial differential equations for the particulate phase, and therefore is much faster than the standard Eulerian method.

In an attempt to bridge the gap between point-force models and fully resolved particles Maxey and co-workers developed a force-coupling method for particles of the order of or larger than the smallest scales of fluid motion (Maxey & Patel (2001), Lomholt & Maxey (2003), Dance & Maxey (2003)). Each particle is represented here by a finite, localized body force distribution based on a force multipole expansion of the disturbed fluid velocity in the vicinity of each particle. The approach has been applied to both zero and finite Reynolds number suspensions (Climent & Maxey (2003)).

Another promising approach especially suited for large numbers of particles is based on *particle probability density functions* (Reeks (1991)).

Here, the particulate phase is modeled in a purely statistical manner eliminating the need to deterministically track individual particles.

For a detailed discussion of the fundamentals of particle-laden flows and further references the reader is referred to the books by Crowe *et al.* (1998) and Clift *et al.* (1978).

## 1.2 Objectives and outline

This dissertation is embedded into the ongoing research activities at the Institute of Fluid Dynamics (IFD) at the Swiss Federal Institute of Technology (ETH) in Zürich. Previous research studies in the field of incompressible single- and two-phase flows include the numerical investigation of density-driven and particle-driven gravity currents. The lock-exchange problem of two fluids of different density was extensively studied based on the Boussinesq approximation for the Navier-Stokes equations (Härtel *et al.* (2000b), Härtel *et al.* (2000a), Härtel (2001)). Particle-driven gravity currents were analyzed by means of high resolution simulations with the aim of revealing fundamental properties of such flows (Necker *et al.* (2002), Necker *et al.* (2003)). Here, the particles were modeled in an Eulerian approach using a transport equation for the local particle concentration.

Continuing this line of research activities the work presented hereafter aims at studying disperse two-phase flows, in which the interaction between the phases is more complex. The particles are modeled in a Lagrangian approach, each interacting individually with the surrounding fluid. More specifically, this dissertation aims at contributing to an enhanced understanding of particle settling in suspensions since this issue is central to all flows in which the dispersed phase has a larger density than the surrounding fluid. To this end, two configurations of particle suspensions of increasing complexity are investigated:

- (i) Settling and break-up of suspension drops under gravity,
- (ii) Particle settling in homogeneous turbulence.

An outline and the motivation for each project will be given separately below. In both projects a special class of particulate two-phase flows is considered, in which the particles are much smaller than the smallest relevant scales of the fluid motion. This allows for the particles to be modeled as point-forces without resolving their finite size. The important advantage of this simplification is that the fluid equations are solved for the entire computational domain, thus avoiding the use of phase-

averaged two-phase equations and the associated closure problem. The presence of the particles and their dynamical effect on the carrier fluid are accounted for by an additional source term in the Navier–Stokes equations. Each particle is tracked individually along its trajectory. The fluid is assumed incompressible such that a (thermal) energy transfer between the phases is negligible. Since the particles are considered rigid spheres, there is no exchange of mass between the phases and the particle–fluid interaction is entirely described by a momentum exchange due to the relative motion between particles and fluid. This computational approach is sometimes called the Eulerian–Lagrangian method using the point–particle approximation and is similar to the trajectory approach mentioned above.

### 1.2.1 Settling and break-up of suspension drops

A simple yet fundamental example of particle sedimentation is the behavior of a suspension drop settling in a fluid under the influence of gravity. A suspension drop is an initially spherical swarm of small particles that are suspended in initially quiescent fluid (the term 'drop' is used as a synonym for 'suspension drop' hereafter). Only recently the phenomena observed when a suspension drop settles under gravity have gained an increased interest. Nitsche & Batchelor (1997) numerically investigated spherical suspension drops falling under creeping flow conditions. In this case the drop essentially retains its spherical shape while a few particles leak into a tail emanating from the rear of the drop. Nitsche & Batchelor focused on the substructural effects of hydrodynamic diffusion and dispersion. They give a theoretical argument for the drop settling velocity and provide a semi-empirical correlation for the rate of particle leakage from the blob. Machu *et al.* (2001) did computer simulations and experiments of single suspension drops and pairs of trailing drops. They pointed out the crucial role of the initial drop shape. Under Stokes flow conditions an initially pear-like shape, for example, causes the suspension drop to deform into a torus that eventually becomes unstable and breaks up into secondary blobs. These blobs deform into tori themselves resulting in a cascade process of blob deformations and break-ups. This behavior of suspension drops is analogous to that of liquid drops settling in a fluid of smaller density. As opposed to suspension drops, a considerable amount of research work has been devoted to single and trailing liquid drops and fluid rings including theoretical studies (e.g.

Kojima *et al.* (1984)), numerical investigations (e. g. Koh & Leal (1989), Pozrikidis (1990)), and experiments (e. g. Baumann *et al.* (1992)). For a comprehensive review of previous work in this field the reader is referred to Machu *et al.* (2001). Walther & Koumoutsakos (2001) performed simulations of falling suspension drops using a particle vortex method. Their results served primarily for validation purposes of their numerical method.

Nitsche & Batchelor (1997) as well as Machu *et al.* (2001) used Stokeslets in their simulations, i. e. the flow field was assembled as a superposition of Stokes flow disturbances caused by the particles. This approach is limited to the Stokes flow regime with vanishing drop Reynolds numbers ( $Re_d \ll 1$ , with  $Re_d$  based on the drop radius and a characteristic drop settling velocity). To our best knowledge, systematic studies for higher Reynolds numbers are not available in the literature.

The primary objective of this first project is to investigate the settling behavior of suspension drops in a range of moderate Reynolds numbers ( $1 \leq Re_d \leq 100$ ). Since the flow around the suspension drop remains laminar, the systematic variation of different parameters – necessary for a thorough understanding of the underlying physics – is computationally affordable. We aim at clarifying the Reynolds number dependence of the instability leading to torus break-up. Moreover, we examine in detail the role of the (initial) particle distribution and the number of particles inside the drop, as well as the effect of initial shape perturbations. These issues have not been addressed in previous studies.

### 1.2.2 Particle settling in homogeneous turbulence

The second project focuses on the settling properties of a random particle suspension in a turbulent environment. With respect to the fluid motion this flow situation is more complex than in the first project and closer to practical applications, since most technical flows are turbulent exhibiting a wide range of length and time scales.

A lot of research work has been devoted to particle dispersion in turbulent flows. The first studies in this field, mostly analytical in nature, reach back half a century. Yudine (1959) was the first to postulate the “crossing trajectories effect” by which a heavy particle, due to its finite free-fall velocity, changes its fluid neighborhood more rapidly than a light particle that essentially follows the path of fluid points. As a result the autocorrelation of the heavy particle’s velocity decreases compared

to that of the light particle and the dispersion coefficient is reduced. As shown by Csanady (1963) this reduction is approximately equal to the inverse of the free-fall velocity. Reeks (1977) and Pismen & Nir (1978) demonstrated that in the absence of gravity the long-time particle diffusion coefficient is in general greater than that of the fluid. The more recent analytical work by Wang & Stock (1993) explains some of the inconsistencies of previous theoretical and experimental studies and provides algebraic equations for long-time particle dispersion coefficients, time scales, and velocity scales.

The theoretical considerations have been paralleled by experimental and numerical studies. Murray (1970) experimentally investigated the settling velocity and vertical diffusion of particles in oscillating water flows. Snyder & Lumley (1971) focused on the measurement of particle velocity autocorrelations in grid-generated turbulence. Wells & Stock (1983) confirmed in their experiments the crossing trajectories effect being responsible for a decrease of the long-time particle dispersion coefficient. Further experimental studies were concerned with turbulence modulation by particles (Parthasarathy & Faeth (1990), Schreck & Kleis (1993)) and preferential concentration of solid particles in microgravity conditions (Fallon & Rogers (2002)). Turbulence modification (or modulation) occurs when the particle loading is large enough such that the collective dynamical effect of the particles alters the flow properties.

The first numerical study on particle diffusion was conducted by Riley & Patterson (1974). They used a  $32^3$  computational grid and 432 particles at a microscale Reynolds number of  $Re_\lambda = 23$  to show that the particle velocity autocorrelation coefficient increases with increasing particle response time in the absence of gravity. The preferential accumulation of particles in random flow fields and turbulence was analyzed in a number of studies including Maxey (1987a), Squires & Eaton (1991a), Squires & Eaton (1991b), and Elghobashi & Truesdell (1992). Heavy particles were shown to accumulate preferentially in regions of high strain rate and low vorticity. Studying the settling velocity of particles in homogeneous, isotropic turbulence Wang & Maxey (1993) found an increase of the mean settling velocity compared to the terminal velocity of a single particle in still fluid. They explained their findings as a consequence of the “preferential sweeping effect” by which the particles are swept preferably towards regions of downward fluid motion when encountering an eddy.

Squires & Eaton (1990) were among the first to account for the par-

ticles' effect on the turbulence properties ("two-way coupling") in their direct numerical simulations (DNS).<sup>1</sup> They examined the modulation of stationary homogeneous turbulence at particle mass loading ratios  $\Phi_m \leq 1.0$  and found an increase of the turbulent kinetic energy at high wavenumbers relative to the energy at low wavenumbers. Elghobashi & Truesdell (1993) and Truesdell & Elghobashi (1993) investigated decaying homogeneous turbulence laden with heavy particles at volumetric loading ratios of  $\Phi_v \leq 5 \cdot 10^{-4}$ . Under gravity the particles were found to transfer momentum to the small-scale motion increasing the energy content at high wavenumbers. This reduces the decay rate of energy as compared to either the particle-free case or the zero-gravity particle-laden case. These findings were confirmed, extended and further analyzed in a number of subsequent studies including Boivin *et al.* (1998), Druzhinin & Elghobashi (1999), and Ferrante & Elghobashi (2003).

Despite these quite exhaustive studies of particle dispersion and turbulence modification by particles with and without gravity, there have been only a few investigations focusing on the mean particle settling rate in homogeneous turbulence. The aforementioned paper by Wang & Maxey (1993) is central among these revealing the basic mechanism of preferential sweeping that leads to an increase in the mean settling velocity. Yang & Lei (1998) did direct numerical simulations and large-eddy simulations of particles settling in homogeneous, isotropic turbulence. Their results are in good agreement with those by Wang & Maxey. However, both investigations were limited to dilute suspensions with small particle volume fractions where the particles do not have any effect on the carrier fluid ("one-way coupling"). In a recent experiment Aliseda *et al.* (2002) measured the enhancement of the particle settling velocity in grid-generated homogeneous turbulence and found significant quantitative differences in their results compared to the simulations by Wang & Maxey.

These discrepancies call for a systematic numerical study of two-way coupling effects with respect to the mean particle settling velocity in homogeneous turbulence. This is the focus of the second project of this dissertation. The mechanism leading to an additional enhancement of the settling velocity compared with the one-way coupled regime will be

---

<sup>1</sup>Here, direct numerical simulation refers to the full resolution of all relevant scales of the fluid motion rather than to the resolution of a finite-sized particle. In this sense the simulations presented herein using the point-force approximation are also DNS studies.

analyzed in detail for different particle volume fractions in the range  $10^{-6} \leq \Phi_v \leq 10^{-3}$ . This range, in which a transition of one-way to two-way coupling effects is to be expected, has not been investigated systematically in previous studies. These addressed rather high particle volume fractions ( $\Phi_v \gtrsim 10^{-4}$ ) at the upper limit of the range studied herein. Particle dispersion characteristics, such as the correlation between vorticity and regions of particle accumulation, will be analyzed for both one-way and two-way coupling. The results by Wang & Maxey (1993) will serve for validation purposes in the one-way coupled case. Moreover, it will be shown that a modulation of the turbulent properties of the carrier fluid by the particles sets in for volume fractions as low as  $\Phi_v \approx 10^{-5}$ .

Furthermore, a careful comparison with the experimental findings by Aliseda *et al.* (2002) will be performed by matching the simulation parameters as closely as possible to those in the experiment. This last step is primarily done in response to an obvious lack of close adjustments of experiments and simulations to the same set of parameters, which is generally observed in the available literature.

Seite Leer /  
Blank leaf

# Chapter 2

---

## Simulation approach

### 2.1 Governing equations

#### 2.1.1 Particle equations

The transient equation of motion for particles, bubbles, and droplets has been the subject of theoretical and experimental considerations for about 150 years. Although remarkable progress in deriving adequate mathematical and empirical descriptions has been made, there is still broad and justified concern as for the validity of these equations. The review by Michaelides (1997) historically traces the development of particle equations of motion and points out crucial theoretical and numerical limitations. In the present dissertation the well-established particle equation derived by Maxey & Riley (1983) is used for the computation of particle velocities and paths.

We consider a dilute particle suspension, in which the particle concentration is small enough for inter-particle collisions to be neglected. Moreover, the particles are assumed to be much smaller than the smallest relevant scales of the fluid motion. This allows for the particles to be modeled as point forces without resolving their finite size. The trajectory of a single particle is given by

$$\frac{dY_i(t)}{dt} = v_i(t), \quad (2.1)$$

where  $Y_i(t)$  is the particle position,  $v_i(t)$  the particle velocity,  $Y_i(0) = Y_i^{(0)}$  its initial position, and  $i = 1, 2, 3$  denotes the three spatial directions in Cartesian space. The particle equation of motion simplified for small heavy particles reads (Ferrante & Elghobashi (2003))

$$m_p \frac{dv_i(t)}{dt} = 6\pi\mu r \left( u_i(\vec{Y}(t), t) - v_i(t) \right) + (m_p - m_f) g_i \quad (2.2)$$

with  $m_p$  being the particle mass,  $m_f$  the mass of the fluid displaced by a particle,  $\mu$  the dynamic viscosity,  $r$  the particle radius,  $u_i(\vec{Y}(t), t)$  the

fluid velocity at the instantaneous particle position, and  $g_i$  the gravitational acceleration. The first and second term on the right-hand side correspond to Stokes drag and net gravitational force, respectively. Assuming very small particles and relatively long fluid time scales, Eq. (2.2) can further be simplified by neglecting particle inertia (Maxey *et al.*, 1997). In this case the particle motion is governed by a quasi-steady equilibrium between drag forces on the particle's surface and forces due to gravity,

$$v_i(t) = u_i(\vec{Y}(t), t) + \tau_p g_i \left(1 - \frac{\varrho}{\varrho_p}\right) \quad (2.3)$$

with the particle response time

$$\tau_p = \frac{m_p}{6\pi\mu r} = \frac{2}{9} \frac{r}{\nu} \frac{\varrho_p}{\varrho}. \quad (2.4)$$

Here  $\nu$  denotes the kinematic viscosity of the fluid,  $\varrho$  its density, and  $\varrho_p$  the particle density.

In order to non-dimensionalize Eqs. (2.2) and (2.3) a reference length  $L_{ref}$  and a reference velocity  $U_{ref}$  are introduced yielding the dimensionless equations of motion

$$\frac{dv_i}{dt} = \frac{1}{St} \left( u_i(\vec{Y}(t), t) - v_i(t) \right) - \frac{1}{Fr^2} \left(1 - \frac{\varrho}{\varrho_p}\right) \delta_{i3}, \quad (2.5)$$

and for inertialess particles

$$v_i(t) = u_i(\vec{Y}(t), t) - \frac{St}{Fr^2} \left(1 - \frac{\varrho}{\varrho_p}\right) \delta_{i3}. \quad (2.6)$$

Here, all variables are considered dimensionless although not specifically labeled as such. The Stokes number is defined as

$$St = \frac{\tau_p}{T_{ref}} = \frac{m_p}{6\pi\mu r} \frac{U_{ref}}{L_{ref}}, \quad (2.7)$$

and the Froude number is

$$Fr = \frac{U_{ref}}{\sqrt{g L_{ref}}}. \quad (2.8)$$

The specific choice of the reference quantities depends on the physical problem studied and will therefore be discussed separately for single particles, suspension drops, and particles in homogeneous turbulence (see section 2.3 and Appendix E). In Appendix E some considerations are given about the settling of single particles based on Eq. (2.5).

### 2.1.2 Fluid equations

In order to study the interaction between the particulate phase and the carrier fluid, the mutual exchange of momentum has to be accounted for. This is accomplished by an additional source term in the fluid momentum equation, which represents the particles' feedback force. Thus, the fluid motion is governed by the continuity equation,

$$\frac{\partial u_i}{\partial x_i} = 0, \quad (2.9)$$

and the incompressible Navier–Stokes equation in rotational form augmented by a particle feedback source term,

$$\frac{\partial u_i}{\partial t} + \underbrace{\epsilon_{ijk} u_j \omega_k}_{=: S_i} = -\frac{\partial p^{(m)}}{\partial x_i} + \nu \frac{\partial^2 u_i}{\partial x_l \partial x_l} + \frac{1}{\varrho} f_i^{(p)} \quad (2.10)$$

with

$$f_i^{(p)} = - \sum_{j=1}^{n_p^r} F_{i,j}^{(p)} \delta(x_i - Y_{i,j}). \quad (2.11)$$

Here,  $p^{(m)} = (p/\varrho + \frac{1}{2} u_l u_l)$  is a modified pressure and  $n_p^r$  is the number of (real) particles. According to Newton's third law "actio = reactio" the feedback force of the  $j$ -th individual particle  $F_{i,j}^{(p)}$  is equal to the surface forces exerted on the particle by the fluid. In the case of small, heavy particles, cf. Eq. (2.2), the feedback force corresponds to the Stokes drag force yielding

$$f_i^{(p)} = - \frac{6\pi \mu r \varrho_p}{m_p} \sum_{j=1}^{n_p^r} \left( u_{i,j}(\vec{Y}_j) - v_{i,j} \right) \delta(x_i - Y_{i,j}). \quad (2.12)$$

The Dirac  $\delta$ -function indicates that the feedback force of particle  $j$  is applied as a point force at the instantaneous particle position  $Y_{i,j}(t)$ .

The singularity representation of the two-way coupling term, Eq. (2.12), provides a theoretical basis for the implementation of the point-force approximation in the framework of the Eulerian–Lagrangian approach. Depending on the details of the numerical procedure, the individual particle feedback forces are converted to a local force density, which approximates the two-way coupling term  $f_i^{(p)}$ .

In the same way as for the particle equations the fluid equations are cast in non-dimensional form using the reference length  $L_{ref}$  and the reference velocity  $U_{ref}$ . This yields

$$\frac{\partial u_i}{\partial t} + \underbrace{\epsilon_{ijk} u_j \omega_k}_{=: S_i} = -\frac{\partial p^{(m)}}{\partial x_i} + \frac{1}{Re} \frac{\partial^2 u_i}{\partial x_m \partial x_m} + f_i^{(p)} \quad (2.13)$$

with the particle source term

$$f_i^{(p)} = -\frac{\varrho_p}{\varrho} \frac{1}{St} \sum_{j=1}^{n_p^r} (u_{i,j}(\vec{Y}) - v_{i,j}) \delta(x_i - Y_{i,j}). \quad (2.14)$$

Here, all variables are considered dimensionless and the Reynolds number is defined as

$$Re = \frac{U_{ref} L_{ref}}{\nu}. \quad (2.15)$$

## 2.2 Numerical method

### 2.2.1 Discretization and time integration

The fluid equations are solved in an Eulerian framework using a Fourier pseudospectral method (see e.g. Orszag (1971), Schumann *et al.* (1980), Canuto *et al.* (1988)), whereas the particles are tracked in real space solving an equation of motion for each individual particle.

The computational domain is a box of side length  $L$  with periodic boundaries. The solution of the governing equations is obtained on a regular grid containing  $N$  equally spaced grid points in each spatial direction. The pseudospectral method requires each term in Eq. (2.10) to be Fourier-transformed. To this end the velocity and the pressure are expanded in three-dimensional, discrete Fourier series,

$$\mathbf{u}(\mathbf{x}, t) = \sum_{\mathbf{k}} \hat{\mathbf{u}}(\mathbf{k}, t) e^{i\mathbf{k} \cdot \mathbf{x}} \quad (2.16)$$

$$p(\mathbf{x}, t) = \sum_{\mathbf{k}} \hat{p}(\mathbf{k}, t) e^{i\mathbf{k} \cdot \mathbf{x}}, \quad (2.17)$$

where  $\hat{\cdot}$  denotes the Fourier coefficients and  $\mathbf{k}$  is the wavenumber vector

$$\mathbf{k} = k_0 \mathbf{n} = k_0(n_1, n_2, n_3)^T \quad (2.18)$$

with  $n_i = -N/2 + 1, \dots, 0, \dots, N/2 - 1$ . The smallest wavenumber is denoted by

$$k_0 = \frac{2\pi}{L}. \quad (2.19)$$

In each direction the largest wavenumber represented is

$$k_{max} = k_0 \left( \frac{N}{2} - 1 \right). \quad (2.20)$$

The Fourier coefficients in Eqs. (2.16) and (2.17) are obtained by the corresponding back transformations,

$$\hat{u}(\mathbf{k}, t) = \frac{1}{N^3} \sum_{\mathbf{x}} \mathbf{u}(\mathbf{x}, t) e^{-i\mathbf{k}\cdot\mathbf{x}} \quad (2.21)$$

$$\hat{p}(\mathbf{k}, t) = \frac{1}{N^3} \sum_{\mathbf{x}} p(\mathbf{x}, t) e^{-i\mathbf{k}\cdot\mathbf{x}}. \quad (2.22)$$

The transformation of Eqs. (2.9) and (2.10) to Fourier space yields, respectively,

$$\mathbf{k} \cdot \hat{\mathbf{u}}_{\mathbf{k}} = 0 \quad (2.23)$$

$$\frac{d\hat{\mathbf{u}}_{\mathbf{k}}}{dt} = -\frac{1}{k^2} \left( \mathbf{k} \times \left( \mathbf{k} \times [\hat{\mathbf{s}}_{\mathbf{k}} + \hat{\mathbf{f}}_{\mathbf{k}}] \right) \right) - \nu k^2 \hat{\mathbf{u}}_{\mathbf{k}}, \quad (2.24)$$

where the abbreviation  $\hat{\mathbf{u}}_{\mathbf{k}} := \hat{\mathbf{u}}(\mathbf{k}, t)$  is used, and  $k = |\mathbf{k}|$  denotes the magnitude of a wavenumber vector. The Fourier coefficients of the nonlinear terms  $\hat{\mathbf{s}}_{\mathbf{k}}$  and the two-way coupling term  $\hat{\mathbf{f}}_{\mathbf{k}}$  are formally given by

$$\begin{aligned} \hat{\mathbf{s}}_{\mathbf{k}} &:= \hat{\mathbf{s}}(\mathbf{k}, t) = \frac{1}{N^3} \sum_{\mathbf{x}} \mathbf{s}(\mathbf{x}, t) e^{-i\mathbf{k}\cdot\mathbf{x}} \\ \hat{\mathbf{f}}_{\mathbf{k}} &:= \hat{\mathbf{f}}(\mathbf{k}, t) = \frac{1}{N^3} \sum_{\mathbf{x}} \mathbf{f}(\mathbf{x}, t) e^{-i\mathbf{k}\cdot\mathbf{x}}. \end{aligned}$$

It should be noted that the Fourier transformation of the nonlinear terms in Eq. (2.10) results in a convolution integral, which is computationally expensive to resolve. To circumvent this problem the nonlinear terms are computed in physical space. This involves additional Fourier transforms to obtain the velocity vectors in physical space and the Fourier coefficients of the nonlinear and two-way coupling terms in Fourier space. To

avoid aliasing errors involved in these Fourier transformations, a dealiasing procedure according to the 3/2-rule is applied (see Canuto *et al.* (1988)).

For the continuity equation to be valid the velocity vectors must be perpendicular to the associated wavenumber vectors (cf. Eq. (2.23)). In this context we say that the velocity vectors are projected onto divergence-free space. This condition has been incorporated in the derivation of Eq. (2.24). Therefore, the latter is the only fluid equation to be solved by the numerical method.

For the time integration of the governing equations both a second-order Runge–Kutta Crank–Nicolson scheme (RK3CN) and a standard third-order Runge–Kutta scheme (RK3) were used alternatively. A CFL criterion was applied to compute the time step. The corresponding discretization of the equations is detailed in Appendix A.

## 2.2.2 Two-way coupling and interpolation

Usually the locations of the point-particles expressed by the Dirac  $\delta$ -function in Eq. (2.11) do not coincide with the grid points of the computational mesh. The implementation of the two-way coupling therefore requires to determine a local, average particle force density at the grid points. Generally, there is a number of different ways, in which this can be accomplished. One possibility is to distribute the feedback force of each particle onto a number of grid points surrounding the instantaneous particle position. In this case the numerical realization of the two-way coupling term  $f_i^{(p)}$  assumes the general form

$$f_i^{(p)} = \sum_{j=1}^{n_p^r} w_{i,j} F_{i,j}^{(p)}, \quad (2.25)$$

where  $w_{i,j}$  is a weighting factor that depends on the instantaneous particle position, and  $F_{i,j}^{(p)}$  is the feedback force of particle  $j$  converted to a force density. The weighting factor can be understood as the value of a function defining an “area of influence” of a particle, which is used to distribute the particle’s feedback force onto the surrounding grid points. The functions employed in the simulations presented are the *top hat* function  $w_i^{(\sqcap)}(\mathbf{x})$  and the *tent* function  $w_i^{(\wedge)}(\mathbf{x})$ . Using the former is equivalent to attributing the full feedback force of a particle to the closest grid point in its vicinity. Using the latter means to distribute the

feedback force to the eight closest grid points surrounding the instantaneous particle position (for details see Appendix B).

Using these weighting functions the two-way coupling term is implemented for small heavy particles as

$$f_i^{(p)} = - \frac{6\pi\mu r_p}{\varrho_f V_c} \sum_{j=1}^{n_p^r} w_{i,j} (u_{i,j}(\vec{Y}(t), t) - v_{i,j}(t)) . \quad (2.26)$$

Here,  $V_c$  is the reference volume to “convert” the point force into a force density that is dimensionally consistent with the discretized Navier-Stokes equations. The volume  $V_c$  corresponds to the integral over the weighting function  $w_i$  and is thus equal to the grid cell volume.

In non-dimensional form using  $U_{ref}$  and  $L_{ref}$  as the reference quantities Eq. (2.26) becomes

$$f_i^{(p)} = - \frac{\varrho_{pf} V_{pc}}{St} \sum_{j=1}^{n_p^r} w_{i,j} (u_{i,j}(\vec{Y}(t), t) - v_{i,j}(t)) , \quad (2.27)$$

where  $\varrho_{pf} = \varrho_p / \varrho_f$  is the ratio of particle density to fluid density and  $V_{pc} = V_p / V_c$  is the ratio of particle volume to grid cell volume.

To evaluate the velocity difference on the right-hand side of Eq. (2.27) the fluid velocity needs to be interpolated to the instantaneous particle position  $Y_i(t)$ . Several well-established interpolation techniques have been investigated in spectral simulations, see e.g. Yeung & Pope (1988) and Balachandar & Maxey (1989). In the simulations of this dissertation trilinear interpolation, cubic Lagrange polynomials, and spectral summation were used alternatively. The details of these techniques are also given in Appendix B.

### 2.2.3 Computational particles

In a typical particle-laden flow the number of particles is very large ( $n_p > 10^6$ ). Since for each particle a separate equation of motion is solved, a large number of particles involves increased computational time and required memory. Due to current computer limitations it is often not possible to compute the trajectories of all real particles. To circumvent this obstacle the point-particle approximation is augmented by introducing *computational* particles. Each computational particle is considered a representative of a cloud of particles, which are supposed

to be in uniform motion with the computational particle. The number of computational particles can be chosen much smaller than that of real particles thus ensuring an acceptable computational time.

With the concept of computational particles included the numerical algorithm previously described changes only slightly. The computational particles, which have the same properties as the real ones, are tracked along their trajectories according to Eqs. (2.5) or (2.6). If  $M$  denotes the ratio of real to computational particles,

$$M = \frac{n_p^r}{n_p^c}, \quad (2.28)$$

where  $M \geq 1$ , then the feedback force of each computational particle has to represent the forces of  $M$  real particles. Therefore, the two-way coupling term now reads

$$f_i^{(p)} = M \sum_{j=1}^{n_p^c} w_{i,j} F_{i,j}^{(p)}. \quad (2.29)$$

As shown by Elghobashi (2000) two criteria have to be fulfilled to ensure that (i) the point-force approximation adequately represents the local flow properties around each computational particle, and (ii) the power spectrum of the two-way coupling source term does not deviate from that due to the real particles:

**Criterion (i):** Since the feedback force of one computational particle amounts to  $M$  times that of a real particle, the small Reynolds number restriction requires that  $M Re_p \leq 1$ , or

$$Re_p \leq M^{-1}. \quad (2.30)$$

**Criterion (ii):** This condition defines an upper bound of the number of real particles represented by one computational particle,

$$1 \leq M \leq m^* , \quad m^* = \mathcal{O} \left( \frac{\Phi_v \eta^3}{r^3} \right) \quad (2.31)$$

with  $\Phi_v$  the particle volume fraction and  $\eta$  the dissipation length scale (i.e. the Kolmogorov length in a turbulent flow).

## 2.3 Dimensionless parameters

### 2.3.1 Suspension drops

There is a total of seven independent physical quantities that uniquely describe the properties of a suspension drop settling in a fluid under gravity. The fluid is characterized by its density  $\varrho$  and its dynamic viscosity  $\mu$ . A single spherical particle is characterized by two quantities, e. g. the particle mass  $m_p$  and the particle radius  $r$ . Alternatively, one or both of these two could be replaced by the particle density  $\varrho_p$  and the particle volume  $V_p$ . The drop is also characterized by two quantities, e. g. the bulk density  $\bar{\varrho}$  and the drop radius  $R$ . Alternatively, in the same way as for a single particle, the drop mass and the drop volume could be used instead. The force accelerating the suspension drop is characterized by the gravitational acceleration  $g$ . From these seven quantities any others can be derived, i. e. the number of (real) particles  $n_p^r$ , the ratio of particle radius to drop radius  $\epsilon = r/R$ , the initial particle volume fraction  $\Phi_v = n_p^r \epsilon^3$ , as well as the different dimensionless numbers discussed below. According to the Buckingham II Theorem the number of independent dimensionless groupings fully characterizing the system is three less than the total number of variables (given mass, length and time as base dimensions). Thus, we have to specify at least four dimensionless parameters. All others can be derived from those.

The drop Reynolds number is based on a characteristic drop settling velocity  $U_d$  and the drop radius  $R$ ,

$$Re_d = \frac{U_d R}{\nu}, \quad (2.32)$$

and reflects the ratio of inertial to viscous forces on the macroscopic length scale  $R$  of the suspension drop. Here, we follow Machu *et al.* (2001) who define  $U_d := (\bar{\varrho} - \varrho) R^2 g / (\varrho \nu)$  in analogy to the terminal settling velocity of a solid particle with density  $\bar{\varrho}$  and radius  $R$ .

The particle Reynolds number is based on the terminal settling velocity of a single particle,  $U_p = \tau_p g (1 - \varrho/\varrho_p)$ , and the particle radius,

$$Re_p = \frac{U_p r}{\nu} = \frac{2 \epsilon^3}{9 \Phi_v} Re_d. \quad (2.33)$$

The particle Reynolds number is required to be much less than unity for the equation of motion, Eq. (2.2), to be valid (Maxey & Riley, 1983).

It should be noted that, since the dimensionless parameters are coupled among each other, the drop Reynolds number cannot be made arbitrarily large without violating the particle Reynolds number restriction.

The Stokes number is the ratio of the particle response time to a characteristic time scale of the fluid motion. In accordance with Machu *et al.* we define

$$St_d = \tau_p \frac{U_d}{R} = \frac{2 \varrho_p}{9 \varrho} \epsilon^2 Re_d. \quad (2.34)$$

The Froude number reflects the ratio of inertial to gravitational forces and is defined here as

$$Fr_d = \frac{U_d}{\sqrt{g R}}. \quad (2.35)$$

A very large Froude number means that inertia dominates over gravity on the macroscopic scale of the suspension drop.

In general,  $Re_d$ ,  $St_d$ ,  $Fr_d$ , and  $\Phi_v$  will be specified as the four independent non-dimensional quantities. If Eq. (2.6) is used only the dimensionless settling velocity  $St_d/Fr_d^2$  needs to be given. In some cases additional parameters such as the number of particles will be provided for clarity.

As the reference quantities we choose  $U_{ref} = U_d$  and  $L_{ref} = R$ . Thus, the dimensionless parameters in the governing equations become

$$Re = Re_d, \quad St = St_d, \quad Fr = Fr_d. \quad (2.36)$$

### 2.3.2 Particle settling in homogeneous turbulence

In order to define the properties of a dilute suspension of particles settling in homogeneous turbulence under gravity we need to specify eight physical quantities. As in the previous case of settling suspension drops, the fluid is characterized by the dynamic viscosity  $\mu$  and the density  $\varrho$  and a spherical particle by its radius  $r$  and its density  $\varrho_p$ . The gravitational acceleration is given by  $g$ . In addition, we have to specify a geometric parameter characterizing the size of the largest eddies in the turbulent flow and a characteristic velocity. As shown below, we will choose the side length  $L$  of the periodic computational box and a velocity based on the forcing parameters, respectively (the forcing procedure required to maintain stationary turbulence will be discussed in section 2.4). Finally, to define the ensemble of particles we have to specify how many particles

are introduced into a volume of characteristic size  $L^3$ . From these eight quantities five non-dimensional parameters can be formed, which fully define the physical situation.

The turbulence is usually characterized by the Taylor microscale Reynolds number  $Re_\lambda$  (see Appendix D). This quantity is only known a posteriori as a simulation result. The parametrization of the forcing scheme, however, allows to choose input parameters such that a desired microscale Reynolds number and Kolmogorov length will approximately be achieved (as described in the subsequent section 2.4). Based on these forcing input parameters and the desired particle properties the non-dimensional parameters can be specified.

The reference length is

$$L_{ref} = \frac{L}{2\pi} = \frac{1}{k_0} \quad (2.37)$$

with  $k_0$  being the magnitude of the lowest wavenumber vector. The reference velocity is based on the forcing parameters and defined here as

$$U_{ref} = \varepsilon_L^{1/3} k_0^{-1/3}, \quad (2.38)$$

where  $\varepsilon_L$  is one of the forcing input parameters with dimensions  $[m^2/s^3]$  (see subsequent section 2.4). The reference time is accordingly given by

$$T_{ref} = \frac{L_{ref}}{U_{ref}} = \varepsilon_L^{-1/3} k_0^{-2/3}. \quad (2.39)$$

Based on these reference quantities the (forcing) Reynolds number is defined as

$$Re_f = \frac{U_{ref} L_{ref}}{\nu} = \frac{\varepsilon_L^{1/3} k_0^{-4/3}}{\nu}. \quad (2.40)$$

In simulations of particle-laden homogeneous turbulence it is common usage to characterize the particle properties by a Stokes number and by a dimensionless particle settling velocity rather than a Froude number (see e. g. Maxey *et al.* (1997)). To this end the particle equation of motion, Eq. (2.2), is rewritten in the form

$$\frac{dv_i(t)}{dt} = \frac{1}{\tau_p} \left[ (u_i(\vec{Y}(t), t) - v_i(t)) - \tau_p g_i \left( 1 - \frac{\varrho}{\varrho_p} \right) \right], \quad (2.41)$$

where the second term within the square brackets can be identified as the terminal settling velocity  $U_p$  of a single particle in still fluid, i. e. the

Stokes settling velocity. Since particles much smaller than the smallest relevant scales of the fluid motion are considered, it is reasonable to define the Stokes number as the ratio of the particle response time to the Kolmogorov time scale,

$$St_\eta = \frac{\tau_p}{t_\eta}. \quad (2.42)$$

Using the Kolmogorov length  $\eta$  and velocity  $u_\eta$  as the reference quantities Eq. (2.41) assumes the non-dimensional form

$$\frac{dv_i(t)}{dt} = \frac{1}{St_\eta} \left[ (u_i(\vec{Y}(t), t) - v_i(t)) - U_p^* \delta_{i3} \right]. \quad (2.43)$$

Here,  $U_p^* = U_p/u_\eta$  is the non-dimensional Stokes settling velocity (with all other variables considered dimensionless). For a given turbulence level ( $\varepsilon$  and  $\nu$ ) and fixed gravitational constant  $g$  (as in a real-world experiment), the dimensionless terminal settling velocity is related to the Stokes number according to

$$\frac{U_p}{u_\eta} = St_\eta \left( \frac{\nu}{\varepsilon^3} \right)^{1/4} g = St_\eta \frac{t_\eta}{u_\eta} g. \quad (2.44)$$

In simulations, however, these two parameters are often chosen independently of each other implying that the gravitational acceleration  $g$  is adjusted accordingly.

Finally, we need to specify the particle loading of the fluid. To this end, the particle volume fraction,

$$\Phi_v = \frac{(4/3)\pi r^3 n_p^r}{L^3}, \quad (2.45)$$

and the particle mass loading,

$$\Phi_m = \Phi_v \frac{\rho_p}{\rho}, \quad (2.46)$$

are defined. Note that the definition of the particle volume fraction, Eq. (2.45), is based here on the entire volume of the computational box.

The five dimensionless parameters sufficient to define the properties of particles settling in homogeneous turbulence are taken to be  $Re_\lambda$ ,  $St_\eta$ ,  $U_p^*$ ,  $\rho_p/\rho$  and  $\Phi_v$ . From these all other parameters, such as the particle

radius, the mass loading, or the ratio of particle density to fluid density, can be derived.

For a consistent non-dimensionalization of the governing equations the same reference quantities  $U_{ref}$  and  $L_{ref}$  have to be used for the fluid and particle equations. Therefore, we take for the parameters in Eqs. (2.5) and (2.13)

$$Re = Re_f, \quad (2.47)$$

$$St = \frac{\tau_p}{T_{ref}} = St_\eta \frac{t_\eta}{L_{ref}} U_{ref} \quad (2.48)$$

and

$$Fr = \frac{U_{ref}}{\sqrt{g L_{ref}}} = \sqrt{\frac{St}{U_p^*} \left(1 - \frac{\varrho}{\varrho_p}\right)}. \quad (2.49)$$

## 2.4 Forcing of stationary turbulence

### 2.4.1 Implementation

Turbulent flows are dissipative, i. e. they constantly lose energy by dissipation at the smallest scales. Thus, turbulence decays over time unless some sort of energy source is provided to compensate for the energy loss. Although decaying turbulence is of scientific interest in its own right, the study of statistically stationary turbulence is of special importance because time-averaging rather than ensemble-averaging, which is computationally costly, can be applied to obtain statistical flow properties. In the simulation of homogeneous, isotropic turbulence the energy loss is compensated for by artificially adding energy at the large scales. There are different forcing schemes available in the literature to accomplish this energy input, all of which have their advantages and drawbacks, see e. g. Siggia & Patterson (1978), Kerr (1985), Hunt *et al.* (1987). The forcing scheme used in this study was developed by Eswaran & Pope (1988). While reporting various test results of their forcing study, they only briefly outline the numerical implementation. For this reason additional comments on the implementation are given in the following.

The main idea of the forcing is to add energy to a selected number of low wavenumber velocity vectors by an additional source term in the Navier-Stokes equations,

$$\frac{d\hat{\mathbf{u}}_k}{dt} = \hat{\mathbf{a}}_k + \hat{\mathbf{a}}_k^F, \quad (2.50)$$

where  $\hat{a}_k$  represents the right-hand side of Eq. (2.24) and  $\hat{a}_k^F$  is the additional acceleration applied only to the velocity vectors within a low wavenumber band  $0 < |k| \leq K_F$ . The specification of  $\hat{a}_k^F$  is based on Ornstein–Uhlenbeck (OU) processes, which are solutions to the Langevin equation

$$du_L(t) = -\frac{dt}{T_L} u_L(t) + \sqrt{\frac{2\sigma^2}{T_L}} dW(t), \quad (2.51)$$

where  $T_L$  is the integral time scale and  $\sigma^2$  the variance of the OU process. The Wiener process  $dW(t)$  is the most fundamental diffusion process with zero mean and variance  $dt$  (see e.g. Pope (2000), appendix J).

The discrete form of the Langevin equation reads

$$u_L(t + \Delta t) = \left(1 - \frac{\Delta t}{T_L}\right) u_L(t) + \sqrt{\frac{2\sigma^2 \Delta t}{T_L}} \xi(t). \quad (2.52)$$

The first term on the right-hand side determines an exponential decay with time scale  $T_L$  (drift) and the second one is a random increment based on the standardized Gaussian variable  $\xi(t)$  (with  $\xi(t) = 0$  and  $\xi^2(t) = 1$ ). Eq. (2.52) is only valid for  $T_L \neq 0$ . However, Eswaran & Pope also considered the limit  $T_L \rightarrow 0$ . To this end, they define a parameter

$$\varepsilon_L := \sigma^2 T_L. \quad (2.53)$$

Inserting  $\varepsilon_L$  into Eq. (2.52), multiplying by  $T_L$ , and applying the limit  $T_L \rightarrow 0$  yields

$$u_L(t) = \sqrt{\frac{2\varepsilon_L}{\Delta t}} \xi(t). \quad (2.54)$$

Thus,  $u_L(t)$  becomes white noise.

In order to non-dimensionalize Eqs. (2.52) and (2.54) the reference quantities are used as defined for particles in homogeneous turbulence in the previous section (note that  $u_L(t)$  has dimensions  $[m/s^2]$ ). For  $T_L \neq 0$  the non-dimensional Langevin equation reads

$$u_L(t + \Delta t) = \left(1 - \frac{\Delta t}{T_L}\right) u_L(t) + \sqrt{\frac{2\Delta t}{T_L}} \xi(t) \quad (2.55)$$

with all variables considered dimensionless. Similarly, for  $T_L = 0$  we have

$$u_L(t) = \sqrt{\frac{2}{\Delta t}} \xi(t). \quad (2.56)$$

For each wavenumber vector with  $0 < |\mathbf{k}| \leq K_F$  four independent OU processes according to Eqs. (2.55) or (2.56) are used to assemble the complex two-component vector  $\hat{\mathbf{a}}_k^F$  (recall that Eq. (2.50) is solved in divergence-free Fourier space, hence  $\hat{\mathbf{u}}_k$  has two components).

For a given grid resolution the forcing input parameters to obtain a desired Taylor microscale Reynolds number  $Re_\lambda$  and resolution  $k_{max}\eta$  are the viscosity  $\nu$ , the upper bound of the wavenumber band  $K_F$ , the time scale  $T_L$ , and the parameter  $\varepsilon_L$ . Eswaran & Pope provide an estimation procedure to determine these parameters, which is outlined in Appendix C.

#### 2.4.2 Validation

In order to validate the implementation of the forcing scheme, two test simulations were performed with parameters given in the paper of Eswaran & Pope (1988): run f19 for  $T_L = 0$  and run f28 for  $T_L \neq 0$ .

Figures 2.1 and 2.2 show (volume-averaged) turbulent quantities over time. Since the forcing starts with a zero velocity field it takes a few eddy turnover times to “build up” the turbulence. Therefore, time-averaging was started after about 20 eddy turnover times ( $20 t_e$ ). All the quantities shown experience fluctuations over time, their time-average however remains stationary for  $t \gtrsim 20 t_e$ . Thus, the forcing well accomplishes its primary task to maintain stationary turbulence.

It is important to note that Eswaran & Pope apply a “smoothing” procedure to their 3-D energy spectrum, from which other turbulent quantities are then derived. To obtain a 3-D energy spectrum the wavenumber space is divided into a number of shells with increasing radii. The energy associated with all wavenumber vectors of magnitude  $k$  are combined to give the energy content  $E(k)$  of the shell with radius  $k$ . Applying this procedure to a finite number of discrete wavenumber vectors as done in numerical simulations leads to certain shells being “under-” or “overrepresented” compared to a continuous wavenumber space. This is taken into account by the smoothing procedure. The effect of smoothing on the corresponding spectra can be seen in Figs. 2.3 and 2.4 where the 3-D energy and dissipation spectra are plotted for runs f28 and f19, respectively. As seen from the spectra, the dissipation range is well resolved down to the smallest scales with  $k\eta = 1$ . The Kolmogorov ( $-5/3$ )-law is not observed since there is no developed inertial range in the spectra for the low microscale Reynolds numbers considered here.

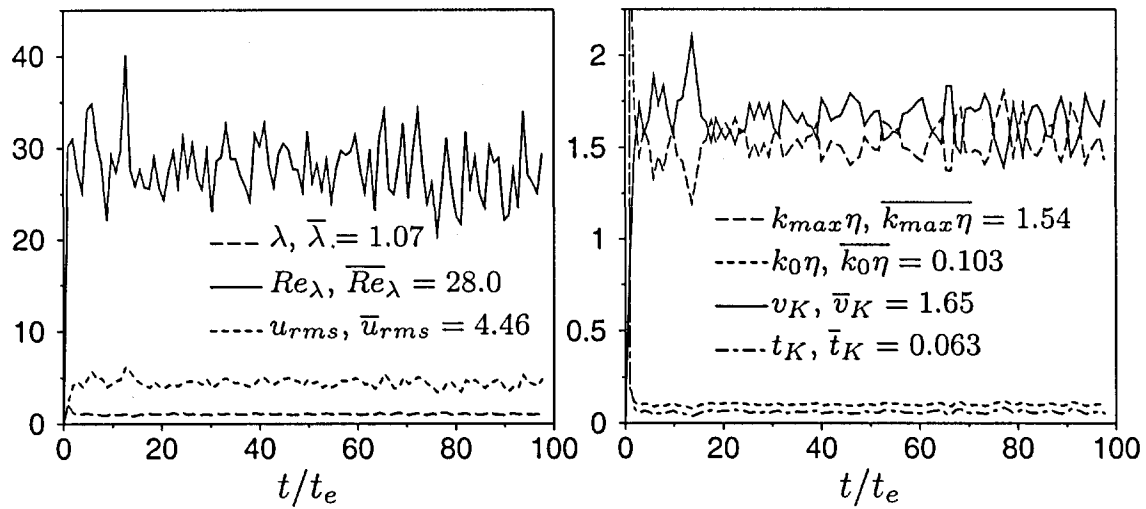


Figure 2.1: Validation run f28, Eswaran & Pope (1988). Left: Taylor microscale, microscale Reynolds number, RMS velocity. Right: resolution, Kolmogorov scales (all quantities from smoothed spectrum).

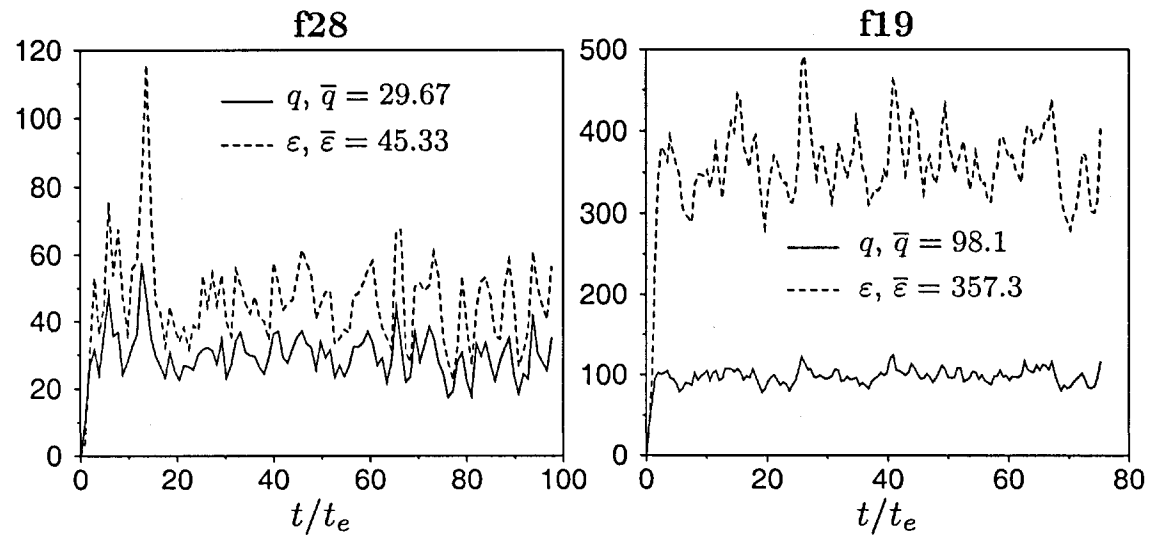


Figure 2.2: Turbulent kinetic energy  $q$  and dissipation rate  $\varepsilon$  computed from smoothed spectrum. Validation runs f28 and f19, Eswaran & Pope (1988).

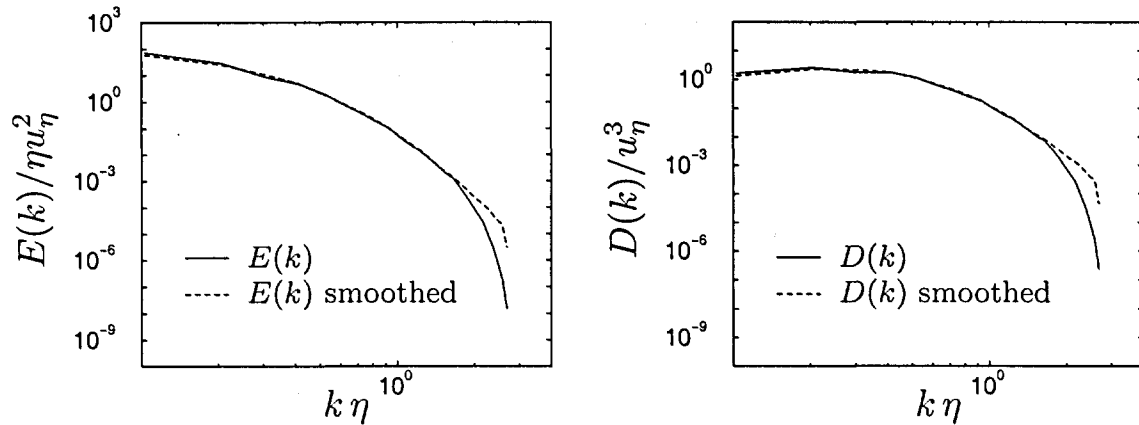


Figure 2.3: Validation run f28, Eswaran & Pope. 3-D energy spectra  $E(k)$  and dissipation spectra  $D(k)$ .

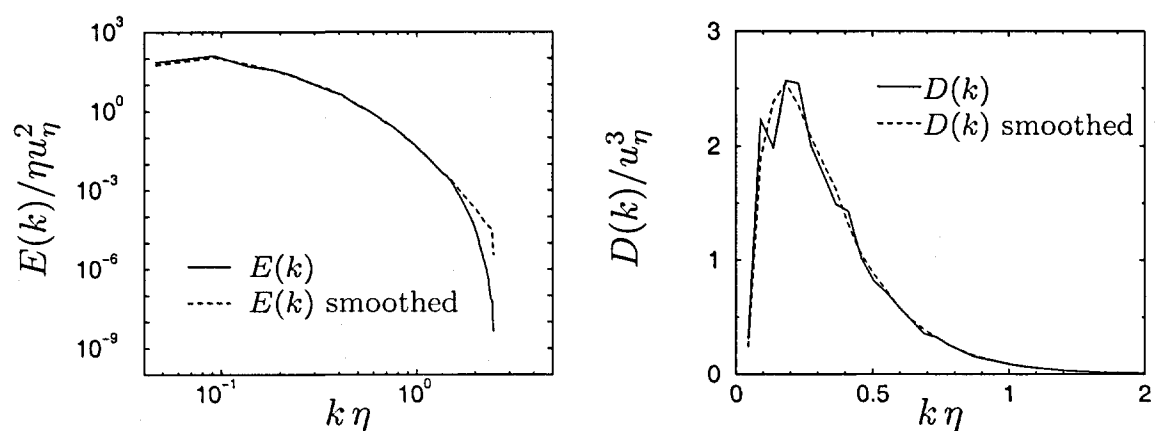


Figure 2.4: Validation run f19, Eswaran & Pope. 3-D energy and dissipation spectra. The linear-linear plot on the right clearly shows the effect of smoothing the dissipation spectrum.

Table 2.1 shows specific average turbulent quantities for a direct comparison with the results by Eswaran & Pope (HIT is the name of the simulation code developed for this dissertation and denotes the results of the present work). The quantities computed from both the “raw” and the smoothed spectrum are given. Fairly good agreement of the smoothed data with those by Eswaran & Pope is achieved. Here, it should be noted that the sampling period of Eswaran & Pope was typically between twelve and twenty eddy turnover times only. Given the rather strong fluctuations (see e. g. Fig. 2.2) it is possible that their statistical data was not fully converged.

	run	$N$	$k_0 \eta$	$k_{max} \eta$	$k_0 l_e$	$Re_\lambda$	$t_e$	$\epsilon$
ESPO	f28	32	0.103	1.55	1.81	28.2	0.409	43.1
HIT (raw)	f28	32	0.103	1.55	2.41	32.1	0.511	45.8
HIT (smoothed)	f28	32	0.103	1.55	1.77	28.0	0.406	45.3
ESPO	f19	64	0.045	1.36	1.18	42.2	0.138	382.9
HIT (raw)	f19	64	0.046	1.42	1.67	42.7	0.134	369.8
HIT (smoothed)	f19	64	0.046	1.42	1.08	39.5	0.198	373.1

Table 2.1: Comparison of non-dimensional time-averaged turbulent quantities with runs f28 and f19 of Eswaran & Pope.

Fig. 2.5 shows a comparison of the forcing scheme by Eswaran & Pope (ESPO) and the backscaling scheme (BS). The latter is similar to the forcing procedure used by Siggia & Patterson (1978). The principal idea is to backscale the magnitude of the velocity vectors within a low wavenumber band to some initial non-zero value at each time step. Thus the energy content in this wavenumber band remains constant and prevents the turbulence from decaying.

Using the ESPO scheme the turbulent quantities such as the kinetic energy and the dissipation rate fluctuate much more strongly compared with the BS scheme. However, the ESPO scheme has two important advantages. First, it can be started from a zero velocity field, whereas the BS scheme requires a fully turbulent initial velocity field that must be generated in advance. Second, the subsequent evolution of the turbulent quantities depends rather strongly on this initial turbulent state when using the BS scheme. This may conserve possible anisotropies in the initial field. Also, as clearly seen in Fig. 2.5, the mean values of the energy  $q$  and dissipation rate  $\epsilon$  are different using the ESPO and the BS

scheme, because the latter “freezes” the energy content at the large scales of the instantaneous velocity field at  $t/t_e \approx 100$ . Due to the random nature of the energy input the ESPO scheme prevents conservation of anisotropies and the long-term time evolution of turbulent quantites does not depend on the initial state.

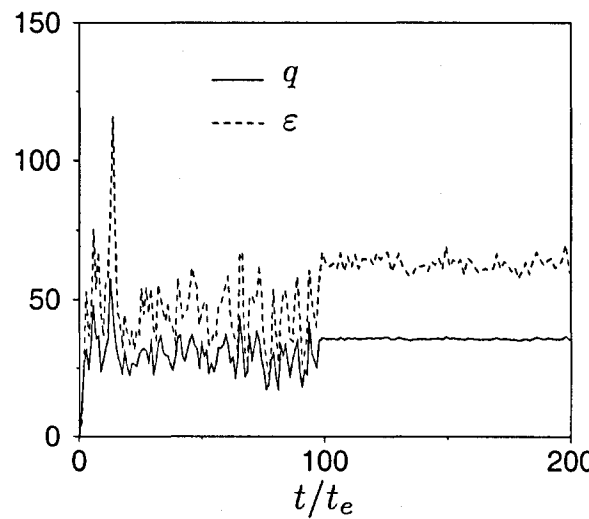


Figure 2.5: Comparison of forcing scheme by Eswaran & Pope (ESPO) and backscaling scheme (BS). At  $t/t_e \approx 100$  the forcing procedure was switched from ESPO to BS.

**Seite Leer /  
Blank leaf**

# Chapter 3

---

## Settling and break-up of suspension drops

The settling and break-up of suspension drops in a fluid under the influence of gravity is a simple example of disperse two-phase flows, in which the particles significantly influence the flow development of the surrounding fluid. The particle-fluid interaction is complex enough to study some fundamental properties of such dispersed phase flows. On the other hand, the numerical treatment is computationally affordable, since the flow remains laminar. This allows for a wide range of parameter variations, which are important for a thorough understanding of the underlying physics.

As detailed in the introduction, section 1.1, the primary focus of the investigations presented in the following is to reveal the physics of suspension drops settling at moderate Reynolds numbers  $1 \leq Re_d \leq 100$ . Furthermore, this flow problem serves as a test case for the Lagrangian point-particle model applied to low Reynolds number flows.

At the beginning of a simulation the suspension drop was set up by randomly distributing  $n_p^c$  computational particles within a spherical boundary of radius  $R$ . The drop was placed in the center of the periodic computational box with the particles and the fluid being initially at rest. Unless otherwise mentioned the ratio of the box side length  $L$  to the initial drop radius  $R$  was  $L/R = 15$  in all simulations for moderate Reynolds numbers.

Since the computational domain contains no solid boundaries there is no mechanism that would prevent the particles and the fluid from ever more accelerating in the direction of gravity (negative  $x_3$ -direction). To maintain the system in equilibrium a uniform pressure gradient was imposed in positive  $x_3$ -direction balancing the net weight of the particles per unit volume (Maxey & Patel (2001)). Settling velocities were computed with respect to the mean fluid velocity in  $x_3$ -direction.

For the time integration of the governing equations the combined Runge-Kutta Crank-Nicolson scheme was used unless otherwise mentioned (see Appendix A). In most of the simulations linear interpolation and the top hat function were employed for the interpolation of fluid velocities and particle feedback forces, respectively (see Appendix B). The influence of different interpolation methods will be discussed explicitly

in section 3.2.5.

In the figures presented in the following the particles' size may be larger than their actual size in the simulations and, if  $n_p^c > 2000$ , no more than 2000 particles are shown for clarity. Also, the particle positions will be displayed with respect to a fixed coordinate system (non-periodic  $x_3$ -coordinate) to indicate the distance traveled by the suspension drop. The initial position of the drop's center of mass coincides with the origin of this coordinate system.

The chapter is divided into two sections, the first dealing with suspension drops settling at low drop Reynolds numbers  $Re_d \ll 1$ , the second focusing on a range of moderate drop Reynolds numbers  $1 \leq Re_d \leq 100$ .

### 3.1 Low Reynolds numbers ( $Re_d \ll 1$ )

For drop Reynolds numbers much less than unity the suspension drop as a whole settles under creeping flow conditions. Nitsche & Batchelor (1997), hereafter referred to as N&B, examined this case both numerically and theoretically. Here their results are used for comparison and validation of our numerical method. N&B found that the drop retains a roughly spherical shape while settling. Only a few particles leak away into a tail emanating from the rear of the drop. Inside the drop the particles undergo a circulatory motion similar to Hill's vortex. This behavior was exactly reproduced in our simulations. Fig. 3.1 shows a suspension drop settling at  $Re_d = 0.1$  (Reynolds numbers  $Re_d < 0.1$  did not show any different results). The parameters were matched to one of the cases given by N&B in their table 1, i. e.  $\Phi_v = 0.02$ ,  $n_p^c = n_p^r = 320$ ,  $\epsilon = 0.0397$  (corresponding to  $St_d = 0.035$ ,  $Fr_d = 1.414$ ). The drop still has a coherent, roughly spherical structure and the tail of particles is clearly visible. This drop can be compared with that in figure 1(b) of N&B for  $T = 10$  (note their different definition of the dimensionless time). It shows good qualitative agreement. Sectional streamlines at  $x_2 = 0$  (vertical box center plane) are also provided in Fig. 3.1. The fluid is subject to a circulatory motion directed downward near the drop's vertical center line and upward in the outer parts of the drop.

In the simulations of N&B the number of particles is confined to a maximum of 320, probably due to computer limitations. A clearer picture of the underlying flow field structure is obtained when a larger number of (smaller) particles is used. The larger number of particles results in a finer discretization of the excess mass of the drop and a

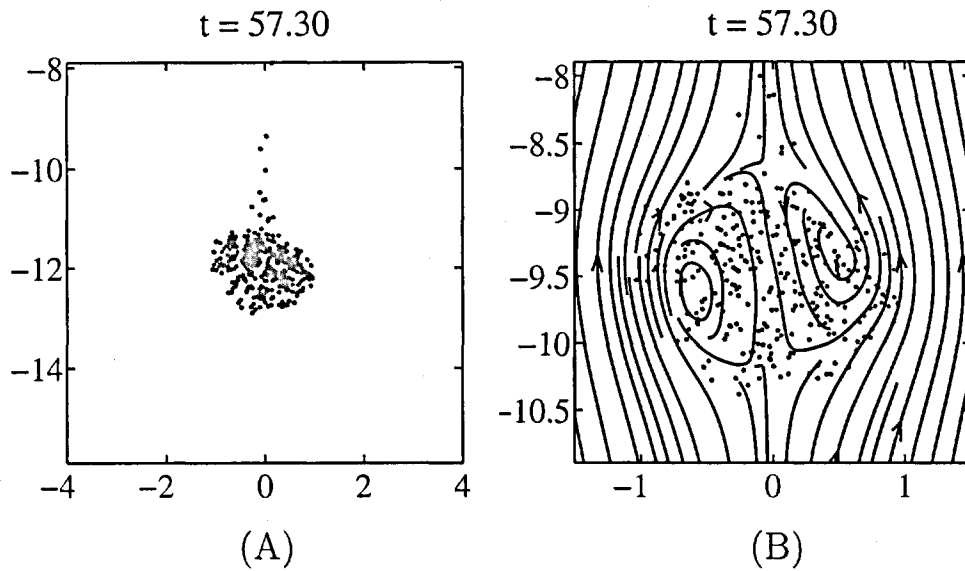


Figure 3.1: Suspension drop settling at  $Re_d = 0.1$ . (A) particles leak away into a tail emanating from the rear of the drop. (B) streamlines in  $(x_1, x_3)$ -plane at  $x_2 = 0$  computed in a coordinate system moving with the drop's center of mass (zoomed in).  $St_d = 0.035$ ,  $Fr_d = 1.414$ ,  $\Phi_v = 0.02$ ,  $n_p^c = n_p^r = 320$ ,  $L/R = 8$ ,  $N = 64$ .

smoother drop “surface” (interface between clear fluid and suspension). Fig. 3.2 shows an example of a suspension drop with 2095 particles settling at  $Re_d = 0.01$  ( $St_d = 0.001$ ,  $Fr_d = 0.447$ ). The streamline plot of the velocity field is shown in both a fixed coordinate system and a relative one attached to the drop's center of mass. Here, the theoretical streamline pattern given by N&B in their figure 2 is very well reproduced. As long as a particle stays inside the region of closed streamlines it remains within the cohesive structure of the drop. However, if a particle settles close to the vertical center line it may get outside of this region. When reaching the drop's lower boundary the particle may be pulled outside the region of closed streamlines as a result of fluid drag forces pulling it sideways and upward (following the streamlines) and gravity pulling it downward. Once outside the enclosing streamlines the particle is swept towards the rear stagnation point at the upper boundary and leaks away into the tail due to its reduced settling velocity outside the cohesive ensemble of particles (the settling velocity of a single particle is typically several orders of magnitude smaller than the settling velocity of the drop).

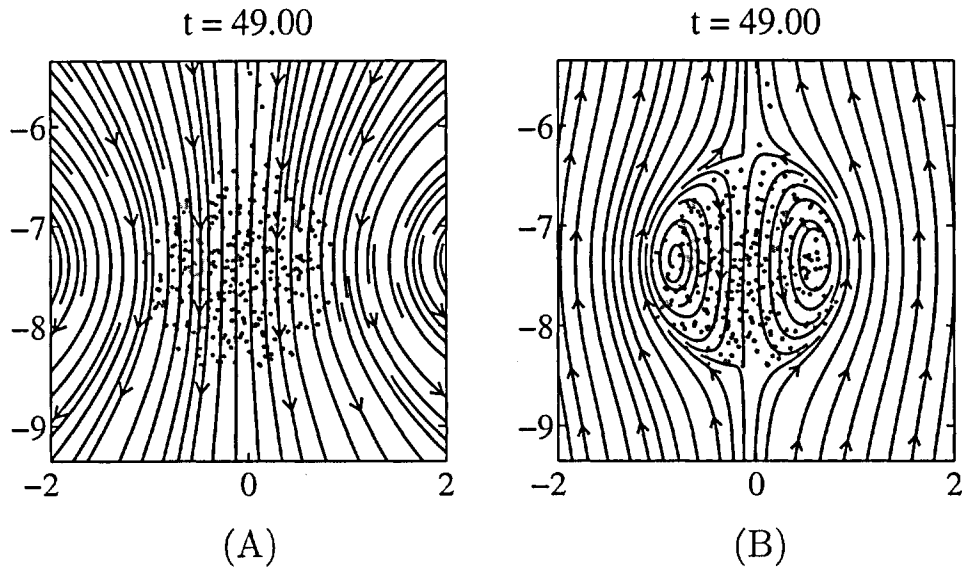


Figure 3.2: Streamlines in  $(x_1, x_3)$ -plane at  $x_2 = 0$ . Velocity computed in (A) a fixed coordinate system, and (B) a coordinate system moving with the particles' center of mass.  $Re_d = 0.01$ ,  $St_d = 0.001$ ,  $Fr_d = 0.447$ ,  $\Phi_v = 0.02$ ,  $n_p^r = n_p^c = 2095$ ,  $L/R = 8$ ,  $N = 64$ .

For a quantitative validation of our numerical approach the drop settling velocity was examined. It is important to recall that our numerical domain has periodic boundaries, i. e. a regular three-dimensional array of suspension drops is simulated rather than a single suspension drop in infinite fluid. As shown above the periodicity of the computational domain has apparently no effect on the principal features of the settling process and even the details, such as the internal circulatory fluid motion, are well reproduced. However, we found that the periodic boundaries do affect the drop's settling velocity. Each drop displaces fluid when settling downwards, which creates an upward flow in its vicinity affecting the neighboring drops. The overall effect is a decrease in settling velocity. A similar decrease in the settling velocity of irregular particle suspensions and regular arrays of solid particles has been reported in the literature and is usually referred to as the hindered settling effect, see e. g. Sangani & Acrivos (1982) and Zick & Homsy (1982).

The hindered settling of suspension drops is demonstrated in Fig. 3.3 (left), where the dimensionless drop settling velocity  $v_d/U_p$  is shown as a function of the drop volume fraction  $c = 4/3 \pi R^3/L^3$ . The parameters for the simulations were matched to the N&B case with  $\Phi_v = 0.02$ ,

$n_p^c = n_p^r = 160$ ,  $\epsilon = 0.05$ . Additionally, we specified  $Re_d = 0.1$  (yielding  $St_d = 0.056$ ,  $Fr_d = 1.414$ ). With increasing box size (decreasing  $c$ ) the number of grid points was augmented accordingly in order to keep the flow field resolution inside the drop constant, i. e. the same ratio of grid points per drop radius in each direction. The simulation parameters and results are summarized in Tab. 3.1.

The larger the drop volume fraction the smaller is the distance between adjacent drops in the periodic array, which enhances the effect of decreasing velocity. For example, increasing the drop volume fraction from  $c^{1/3} = 0.1$  to  $c^{1/3} = 0.2$  causes the settling velocity to decrease by approximately 15%. In Fig. 3.3 it is seen that the decrease in settling velocity is nearly linear for small drop volume fractions  $c^{1/3}$ . In the case of an array of solid spheres it can be shown analytically that, for small (sphere) volume fractions, the settling velocity depends roughly linearly on  $c^{1/3}$  (Hasimoto (1959), Sangani & Acrivos (1982)). Assuming that the same linear dependence applies to hindered settling of suspension drops, the data in Fig. 3.3 (left) is linearly extrapolated to  $c = 0$ , which corresponds to a suspension drop in infinite fluid. This yields a settling velocity  $v_d^0/U_p = 10.7$ , which is in good agreement with the result by N&B (see Tab. 3.2).

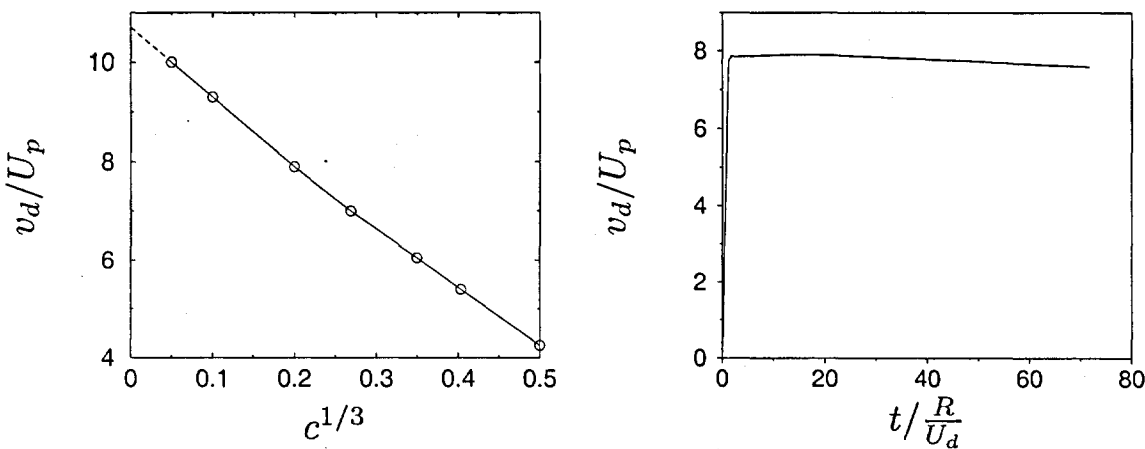


Figure 3.3: Hindered settling of suspension drops. Left: the drop settling velocity  $v_d$  is shown as a function of the drop volume concentration  $c^{1/3}$ . Circles indicate simulations performed. Dashed line extrapolates data to  $c = 0$ . Right: drop settling velocity as a function of time for  $Re_d = 0.1$  and  $L/R = 8$  (run #3,  $c^{1/3} = 0.2$ ).

The drop settling velocity as a function of time is shown in Fig. 3.3

run #	$c^{1/3}$	$c$	$L/R$	$N$	# cells/ $R$	$v_d/U_p$
1	0.05	$1.25e(-4)$	32.34	128	3.96	10.0
2	0.1	0.001	16.12	64	3.97	9.3
3	0.2	0.008	8.06	32	3.97	7.9
4	0.27	0.019	5.99	24	4.01	7.0
5	0.35	0.043	4.61	20	4.30	6.1
6	0.4	0.064	4.03	16	3.97	5.4
7	0.5	0.125	3.22	12	3.70	4.3

Table 3.1: Data of simulations shown in Fig. 3.3.

N&B: theory	N&B: simulation	extrapolation	Fig. 3.3
$v_d^0/U_p$	$10.6$	$10.5 \pm 0.1$	10.7

Table 3.2: Comparison of drop settling velocity with Nitsche &amp; Batchelor (1997).

(right) for the case of  $c^{1/3} = 0.2$ . The drop is rapidly accelerated from rest to reach a quasi-stationary settling velocity for a short period of time between  $t \approx 10$  and  $t \approx 25$  (this quasi-stationary velocity is plotted on the left in this figure). As soon as particles start leaking away into the tail the settling velocity slowly decreases.

Fig. 3.4 shows a comparison between hindered settling/rising of suspension drops, solid particles, and bubbles of the same size. In order to be independent of the individual drop (or particle/bubble) properties, the settling/rise velocities have been normalized by the corresponding terminal velocities in the limiting case of  $c = 0$ . Thus, in principle, the curve for suspension drops shown in Fig. 3.4 should be independent of specific particle and drop properties as long as  $Re_d \leq 0.1$ . Some spurious effects may be present due to the coarse drop discretization in terms of the number of particles ( $n_p^c = 160$ ). The principal observation is that the hindered settling of a regular array of suspension drops is less pronounced than that of solid particles and more pronounced than the hindered rising of bubbles. The analytical results for hindered settling of liquid drops and porous particles can be found in Sangani (1987) and Mo & Sangani (1994). Based on the formula for liquid drops (including

the limiting case of bubbles) presented in the former work, the hindered settling of suspension drops can be approximated for small drop volume fractions by

$$\frac{v_d}{v_d^0} = 1 - 1.76 c^{1/3} \frac{U_t}{v_d^0}, \quad (3.1)$$

where the terminal velocity of a solid particle of the same size as the suspension drop is  $U_t = (2/9) U_d = (2/9)(\bar{\rho} - \rho)R^2g/\mu$ . Eq. (3.1) is also plotted in Fig. 3.4 and found to accurately describe the asymptotic behavior of suspension drops for drop volume fractions  $c^{1/3} \lesssim 0.2$ .

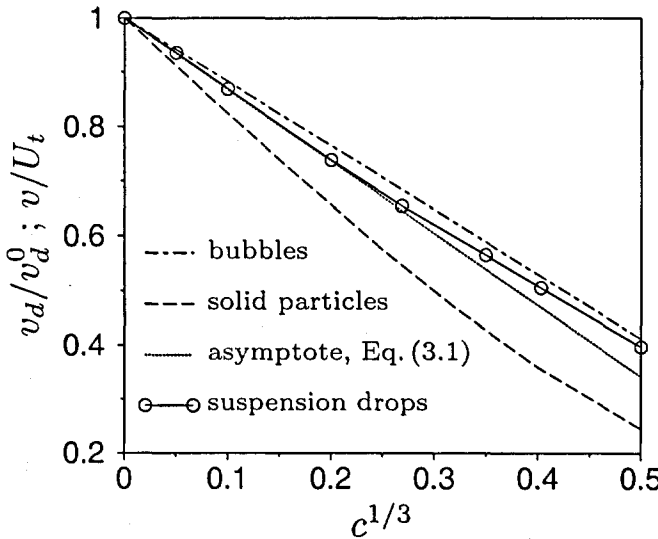


Figure 3.4: Hindered settling/rising of suspension drops, solid particles, and bubbles. The drop settling velocity  $v_d$  is normalized by the extrapolated settling velocity  $v_d^0$ . The particle and bubble velocities  $v$  are normalized by their corresponding terminal (Stokes) velocities  $U_t$  in infinite fluid. The asymptote is an approximation for small  $c$  according to Eq. (3.1).

## 3.2 Moderate Reynolds numbers ( $1 \leq Re_d \leq 100$ )

### 3.2.1 Reynolds number dependence

At drop Reynolds numbers  $Re_d \geq 1$  the suspension drop undergoes a complex shape evolution with eventual break-up into a number of secondary blobs. Fig. 3.6 shows a typical sequence of deformations and break-up of a drop settling at  $Re_d = 1$  ( $St_d = 0.0076$ ,  $Fr_d = 4.47$ ,  $\phi = 0.02$ ). The initially spherical drop flattens into an oblate shape

featuring a growing dimple at its rear (for  $t \lesssim 120$ , not shown in the figure). The dimple is formed because the fluid inside the drop below the particles at the rear (upper) boundary is accelerated downward by particle drag, whereas the fluid in front of the drop is still quiescent. Thus, the particles at the rear settle faster than those at the leading front, which creates the dimple shape. The dimple keeps growing inside the drop such that the latter deforms into a torus. The torus grows larger in diameter while traveling, before it eventually becomes unstable and disintegrates into two secondary blobs. The last sample of the sequence in Fig. 3.6 looks remarkably similar to two photographs of experiments at low Reynolds numbers given by Machu *et al.*, which are shown in Fig. 3.5. In the experiments the initial conditions were certainly different from a spherical suspension drop with all particles at rest. However, the key feature of the break-up process, the formation of a torus as found in our simulation, was observed in the experiments as well. A detailed discussion of the influence of initial conditions will be given later in section 3.2.2.

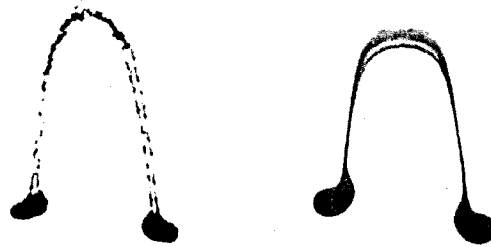


Figure 3.5: Disintegrated suspension drop (left) and liquid drop (right) in an experiment by Machu *et al.* (2001)

Fig. 3.7 shows a visualization of the flow field inside and outside the settling torus from Fig. 3.6. The streamlines, displayed on a vertical plane through the center of the computational box ( $x_2 = 0$ ), reveal a ring vortex growing in diameter over time. The ring vortex coincides with the particles forming the settling torus. At  $t = 358$  the ring vortex is closed in the sense that no streamlines pass from the front (lower) stagnation point through its center to the rear (upper) stagnation point. At  $t = 477$ , due to the growing ring hole, fluid starts penetrating the torus from the front stagnation point. At  $t = 597$  an open ring vortex is observed with streamlines passing through the center hole. This marks the beginning of torus disintegration. The transition from a closed to

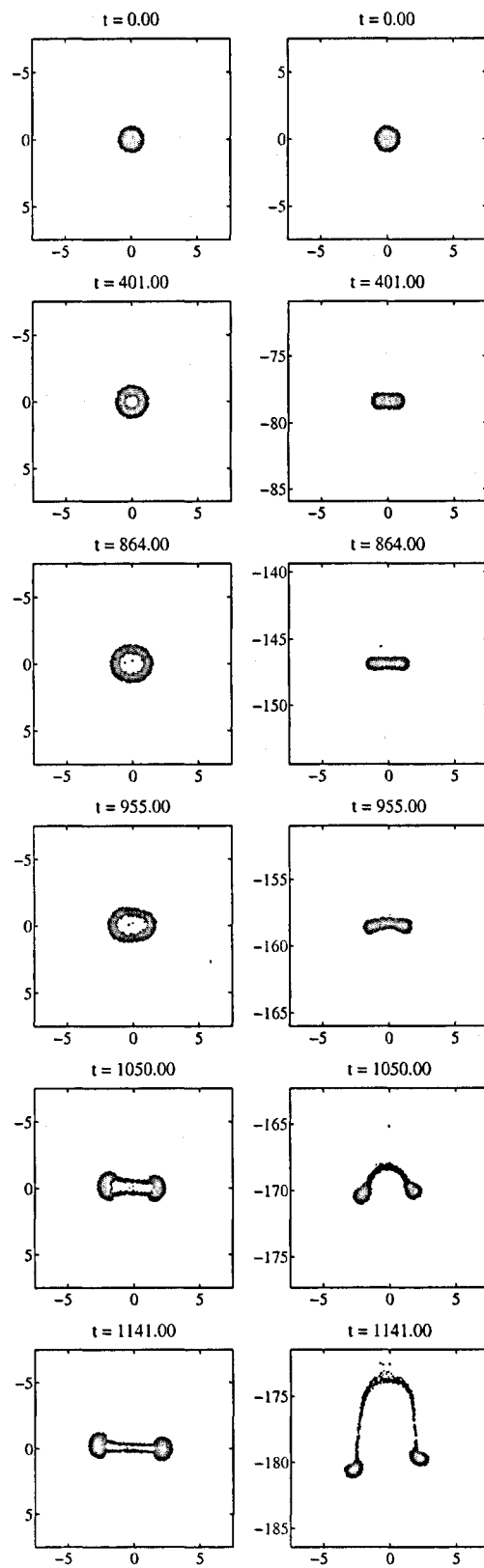


Figure 3.6: Typical sequence of deformations and break-up of a suspension drop settling at  $Re_d = 1$  ( $St_d = 0.0076$ ,  $Fr_d = 4.47$ ,  $\Phi_v = 0.02$ ,  $n_p^c = n_p^r = 100096$ ,  $N = 128$ ). Left: top view, right: side view.

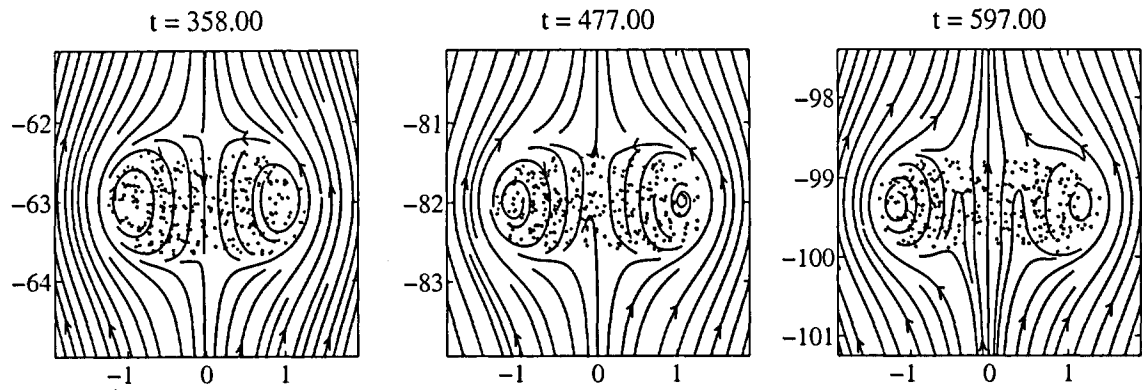


Figure 3.7: Transition from closed to open torus for  $Re_d = 1$ . Same simulation as shown in Fig. 3.6. The streamlines are computed in a coordinate system moving with the drop's center of mass and are displayed on a vertical plane at  $x_2 = 0$ . For clarity only 300 particles are shown.

an open torus was observed by Machu *et al.* in both their experiments and simulations. The difference is that they considered a low Reynolds number case,  $Re_d \ll 1$ , with an initially bell-shaped drop whereas here, the same phenomenon occurs for  $Re_d = 1$  and an initially spherical drop. As will be shown later in this section, the torus transition is not observed for higher Reynolds numbers. Fig. 3.8 shows the trajectories of three particles in a frame moving with the particles' center of mass for the same case of  $Re_d = 1$  discussed above. At the beginning the particles undergo a circulatory motion essentially the same as that indicated by the streamlines in Fig. 3.7. As long as the torus is stable the circulation continues and, as seen in the top view of Fig. 3.8, the particles are not displaced in azimuthal direction of the torus. This indicates that the flow field remains axisymmetric with respect to the  $x_3$ -axis. Only when the bulges form and the torus starts disintegrating (cf.  $t = 955$ , Fig. 3.2), particles are entrained towards the blobs being formed (trajectory t2).

In order to study the Reynolds number dependence of the disintegration process, the Reynolds number  $Re_d$  was successively increased while keeping (almost) all other parameters constant. We chose  $St_d = 0.01$ ,  $Fr_d = 10$ ,  $\Phi_v = 0.02$ ,  $n_p^c \approx 108000$ ,  $M = 7$  and the same initial particle distribution in all cases. From Eq. (2.34) it is clear that the density ratio has to be decreased accordingly if the Stokes number is to remain constant with increasing  $Re_d$ . The grid resolution was set to  $N = 128$ .

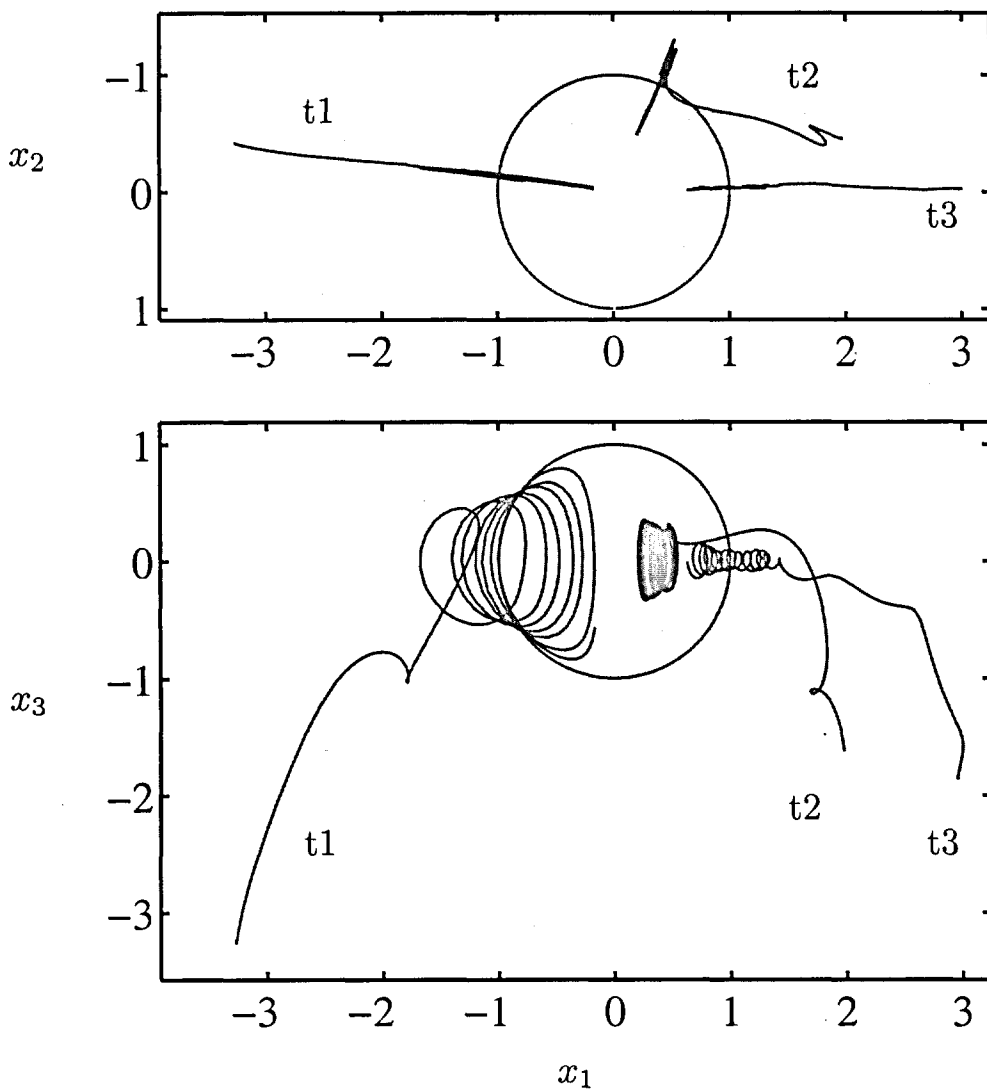


Figure 3.8: Trajectories of three particles ( $t_1, t_2, t_3$ ) inside the suspension drop shown in Fig. 3.6 ( $Re_d = 1$ ). The circle indicates the initial drop. The trajectories are computed in a coordinate system attached to the particles' center of mass.

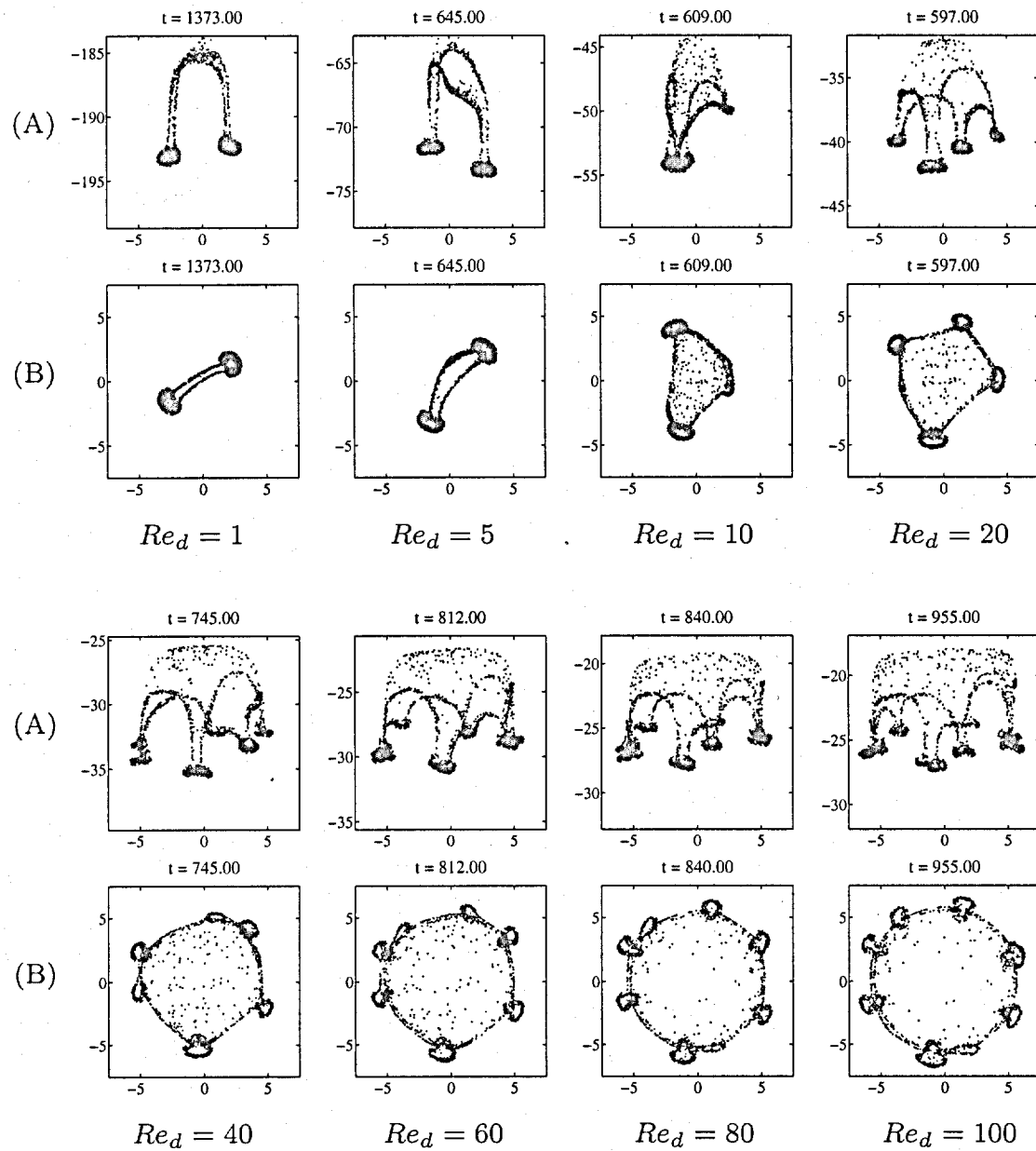


Figure 3.9: Disintegrated suspension drops at different drop Reynolds numbers. (A) top view, (B) side view.  $St_d = 0.01$ ,  $Fr_d = 10$ ,  $\phi = 0.02$ ,  $n_p^c \approx 108000$ .

Fig. 3.9 shows disintegrated suspension drops for  $Re_d = 1, 5, 10, 20, 40, 60, 80$ , and  $100$ . It is observed that the number of secondary blobs increases with increasing Reynolds number. For  $Re_d = 1$  two secondary blobs are obtained, for  $Re_d = 100$  the torus breaks up into seven major and one minor secondary blobs. The shape evolution of the initially spherical drop and the torus before break-up is similar to that shown in Fig. 3.6 in all cases. However, for  $Re_d > 5$  the torus is usually spanned by a “membrane” of dilute particles as shown in Fig. 3.10. A

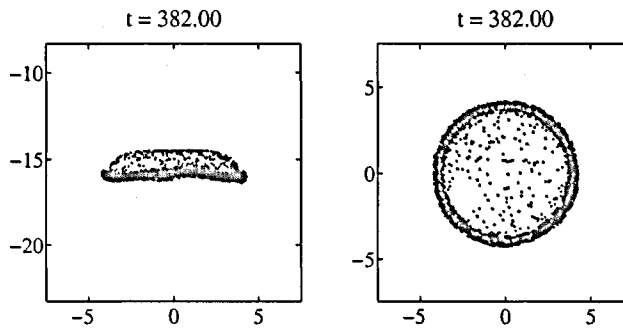


Figure 3.10: Side and top view of the torus spanned by a “membrane” of dilute particles at  $Re_d = 100$ .

comparison of the (nondimensional) drop settling velocities for different Reynolds numbers is provided in Fig. 3.11. It must be emphasized that the settling velocities are inherently affected by the hindered settling effect discussed in the previous section. Therefore, the velocities have been normalized by the maximum settling velocity for  $Re_d = 1$ . This allows for a relative comparison between different Reynolds numbers. It is seen that the higher the Reynolds number the smaller are the settling velocities. After reaching a peak value shortly after the particles are released the setting velocities decrease gradually as the torus is forming and expanding. This decrease is stronger and occurs at increasingly shorter times for larger Reynolds numbers reflecting a faster disintegration. For  $Re_d = 1$  the decrease of the settling velocity is considerably weaker than in the other cases. This is due to a relatively slow deformation of the drop into a torus, which then remains stable for a long period of time. Towards  $Re_d = 100$  the velocity curves become similar suggesting an asymptotic behavior for  $Re_d = 0(10^2)$ .

In order to determine the time required for the drop to deform into a torus, a radius,  $R_p^m$ , is defined as the mean distance of the particles to the center of mass in the  $(x_1, x_2)$ -plane. The time  $T_{d-t}$  required

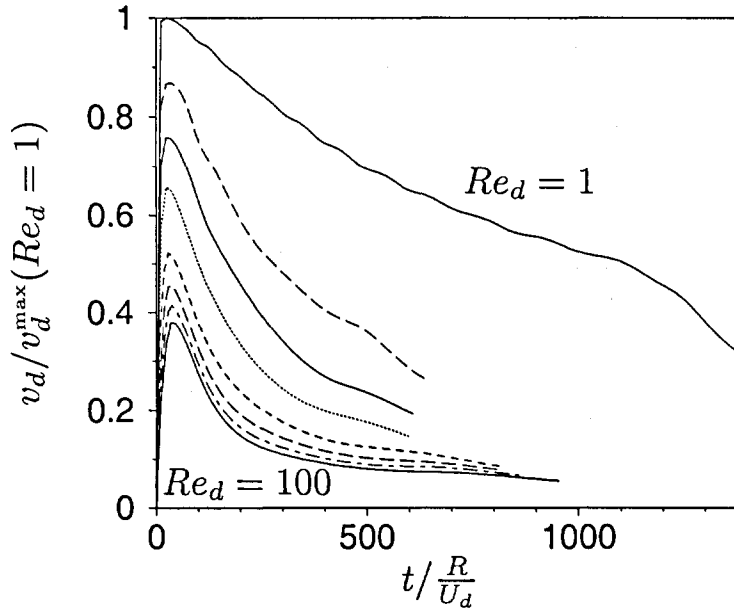


Figure 3.11: Comparison of drop settling velocities for different Reynolds numbers,  $Re_d = 1, 5, 10, 20, 40, 60, 80, 100$  ( $Re_d$  successively increasing from top down). Same simulations as in Fig. 3.9.

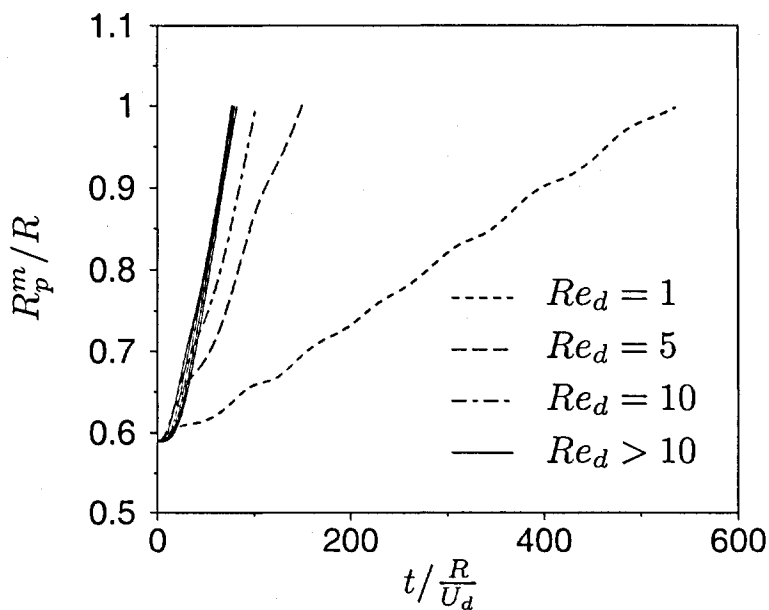


Figure 3.12: Time evolution of the mean radial particle distance from the center of mass,  $R_p^m$ , for different Reynolds numbers,  $Re_d = 1, 5, 10, 20, 40, 60, 80, 100$ . Same simulations as in Fig. 3.9.

$Re_d$	1	5	10	20	40	60	80	100
$\frac{T_{d-t}}{T_{d-t}(Re_d=1)}$	1	0.278	0.190	0.154	0.146	0.144	0.146	0.149

Table 3.3: Characteristic times  $T_{d-t}$  (normalized by  $T_{d-t}(Re_d = 1)$ ) for the deformation of the drop into a torus.

for  $R_p^m$  to reach the initial drop radius  $R$  is taken as a characteristic measure for the deformation of the drop into a torus. Fig. 3.12 shows the time evolution of  $R_p^m/R$  until  $R_p^m/R = 1$  for different Reynolds numbers. The corresponding characteristic times  $T_{d-t}$ , normalized by  $T_{d-t}(Re_d = 1)$ , are given in Tab. 3.3. The principal observation is that the deformation of the drop into a torus occurs the faster the higher the Reynolds number. Again, towards  $Re_d = 100$  an asymptotic behavior is found. In the case of  $Re_d = 1$  the time evolution of  $R_p^m$  reveals a slightly pulsating expansion and contraction of the torus. This behavior was also observed by Machu *et al.* for vanishing Reynolds number and a pear-like initial drop shape.

Fig. 3.13 shows the time evolution of the flow field for a suspension drop settling at  $Re_d = 100$ . The streamlines are computed in a coordinate system moving with the particles' center of mass. They are shown on a vertical center plane at  $x_2 = \pi$ . As opposed to the case of  $Re_d = 1$  the particle torus and the ring vortex do not coincide and the corresponding transition from a closed to an open torus is not observed. Instead the circulatory motion inside the initial drop starts extending towards the rear of the flattening drop shortly after the release ( $t = 95$ ). As the drop deforms into a torus spanned by a membrane of particles, the ring vortex moves completely outside the torus and the streamline structure looks similar to the wake of a circular flat plate ( $t = 191$ ). As long as the torus and the ring vortex coincide at least partially, the streamlines at the rear (upper boundary) of the torus point towards the torus. This keeps the torus and the membrane a compact structure. When the ring vortex detaches from the torus, however, the membrane of particles starts bulging towards the rear ( $t = 286$ ). This is due to the smaller settling velocity of single particles within the membrane compared to the settling velocity of the compact torus. In the further course of the settling process the ring vortex gradually dissipates ( $t = 382$ ). Since the particle torus and the ring vortex no longer coincide, there is

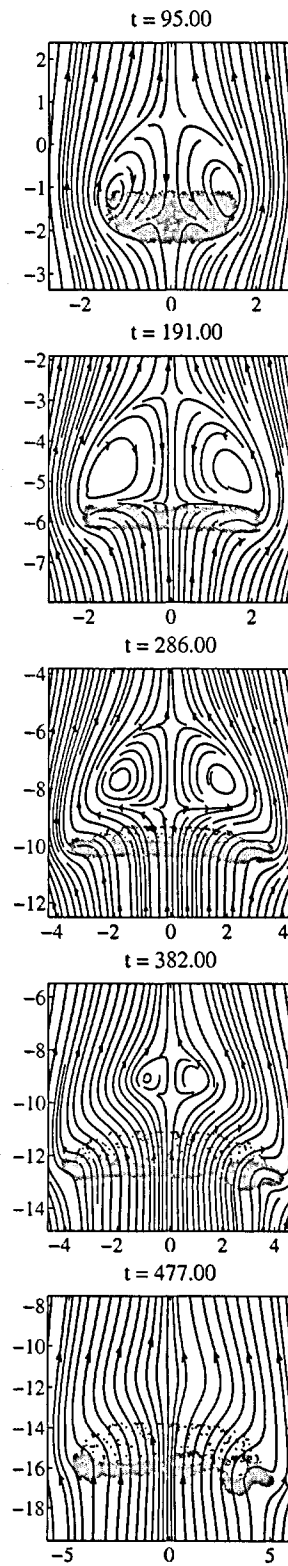


Figure 3.13: Evolution of the flow field for a suspension drop settling at  $Re_d = 100$ . The streamlines are computed in a coordinate system moving with the drop's center of mass and are displayed on a vertical plane at  $x_2 = \pi$ . From top to bottom the view frame zooms out of the expanding suspension torus.

no particle–fluid interaction that could sustain the vortex and the latter eventually disappears completely ( $t = 477$ ).

As pointed out by Machu *et al.* and others (e. g. Joseph & Renardy (1993)) the disintegration of the suspension torus is due to a Rayleigh–Taylor–type instability. In fact, in a first approximation the suspension can be considered a pseudoliquid of increased density  $\bar{\rho}$ . In this case small perturbations of the interface between the heavier pseudoliquid making up the torus and the lighter clear fluid will amplify and eventually lead to break–up. For a detailed discussion of the classic Rayleigh–Taylor instability the reader is referred to Chandrasekhar (1961). In the case of a “real” suspension, i. e. a particle–fluid mixture as in our simulations, there is no distinct interface between torus and clear fluid, but the instability mechanism works in a similar way as for two fluids of different density. A not perfectly uniform particle distribution results in a locally varying mixture density of the suspension, which causes some parts of the torus to settle faster than others. This creates perturbations of the torus shape and “surface” and is the starting point of the instability mechanism.

In the following sections we address the question: What determines the break–up behavior of a suspension drop at a given Reynolds number? To this end we study the influence of the initial particle positions, the effect of initially imposed drop shape perturbations, as well as the influence of the drop mass discretization in terms of the number of particles. With respect to the instability leading to torus break–up we try to distinguish as clearly as possible between perturbations of a “physical” nature, which are our primary interest, and those of a “numerical” nature. The former can also be present in a real–world experiment, whereas the latter are inherent to the numerical procedure. It is important to distinguish between “physical” and “numerical” sources of perturbations because both may affect the break–up behavior of a suspension drop in numerical simulations. Therefore, in order to demonstrate that our results are not tainted by numerical effects, the influence of the grid resolution, the periodic boundaries, and the interpolation used in the computation of the particle feedback force will be discussed briefly.

### 3.2.2 Influence of the initial particle distribution

The crucial role of the initial conditions has been pointed out by several authors (e. g. Machu *et al.* (2001), Kojima *et al.* (1984)), primarily with

respect to the initial drop shape. Machu *et al.* showed that even at very low Reynolds numbers,  $Re_d \ll 1$ , an initial shape different from a sphere, for example a bell-shaped drop, deforms into a torus with subsequent break-up. In our study it was found that the particle positions within the initial drop also affect the details of the break-up process and may even yield a different number of secondary blobs. Fig. 3.14 shows two examples of simulations with different initial particle positions. The initial distribution was uniformly random in all cases. For  $Re_d = 1$  the number of secondary blobs did not vary for different initial particle positions, but the location of the blobs was different. For  $Re_d = 100$  the details of the particular break-up pattern were different for different initial particle positions and even the number of secondary blobs varied between five and seven. These results demonstrate that the instability is very sensitive to the details of the initial conditions, and corroborate the idea of the particle distribution being the primary source of perturbations.

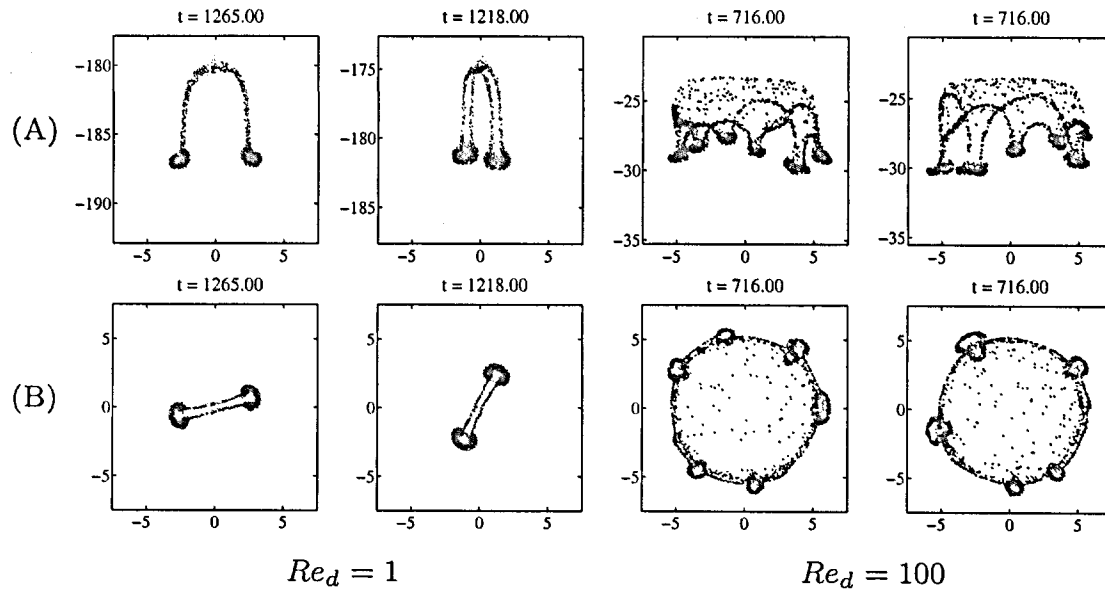


Figure 3.14: Disintegrated blobs for different initial particle positions. Left:  $Re_d = 1$ ,  $St_d = 0.01$ ,  $Fr_d = 4.5$ ,  $\phi = 0.02$ . Right:  $Re_d = 100$ ,  $St_d = 0.01$ ,  $Fr_d = 44.7$ ,  $\phi = 0.02$ .  $N = 64$  in both cases. (A) side view, (B) top view.

In order to shed more light on the role of the particle distribution, a set of simulations was performed with initially perturbed drop shapes. Perturbations due to the (initial) particle distribution are termed “natural” in the following, whereas the initial shape variations are called

“imposed artificial” perturbations. Starting from a spherical shape with a uniformly random particle distribution, the particles’ radial position with respect to the drop center line in the vertical direction was shifted according to

$$\Delta r = A_s \cos(l_s \theta). \quad (3.2)$$

Here  $\Delta r$  is the radial shift of the particle position in the  $(x_1, x_2)$ -plane with respect to the drop centerline,  $A_s$  is the perturbation amplitude,  $l_s$  is the number of periods along the circumference, and  $\theta$  is the azimuthal angle. Fig. 3.15 displays an initially perturbed suspension drop. Clearly, this is only one possibility to introduce controlled (artificial) perturbations, which allows us to trigger a certain break-up behavior of the suspension drop.

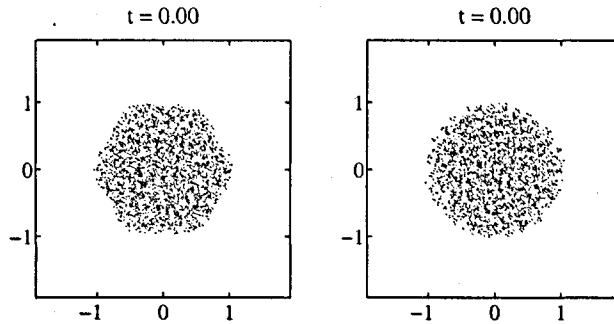


Figure 3.15: Initially perturbed suspension drop. Top view (left), side view (right).  $A_s = 0.05 R$ ,  $l_s = 6$ .

Fig. 3.16 shows disintegrated, artificially perturbed drops with  $l_s = 6$  ( $Re_d = 100$ ,  $St_d = 0.01$ ,  $Fr_d = 44.7$ ). The perturbation amplitude  $A_s$  was varied between  $0.1 R$  and  $0.001 R$ . The last drop shown in the lower two rows is an unperturbed reference case. The number of particles was  $n_p^c = 29433$  resulting in an initial mean particle spacing of  $d \approx 0.052 R$  (defined as  $d = (4\pi/3 n_p^c)^{1/3} R$ ). If the artificial perturbation level is large enough, the forced perturbations dominate the disintegration process and the drop breaks up into six equally spaced secondary blobs (first and second case with  $A_s = 0.1 R$  and  $A_s = 0.05 R$ ). If the artificial perturbation amplitude drops well below the order of the mean particle spacing ( $A_s = 0.001 R$ ), the natural perturbations clearly predominate and the disintegrated structure differs only little from the unperturbed reference case. Between these two cases, the natural and the artificial perturbation level are apparently of about the same order and none

clearly prevails ( $A_s = 0.01 R$ ). Here, as in other parts of this work also, we rely on visual judgment only, primarily for lack of measurable quantities that better characterize the entire break-up process.

As long as the artificial perturbations are large enough, i. e. of the order of the mean particle spacing, different break-up patterns can be triggered depending on the parameter  $l_s$ . For  $Re_d = 100$  any number between three and ten secondary blobs could be forced (same parameters as in Fig. 3.16,  $A_s = 0.05 R$ ). Three examples are shown in Fig. 3.17. These results further illustrate the crucial role of the particle distribution as a source of perturbations. The interplay of natural and artificial perturbations will be revisited within the spectral analysis of the settling torus in section 3.2.7.

### 3.2.3 Influence of the number of particles

The excess mass of the suspension drop with respect to the surrounding clear fluid is concentrated into the points where the particles are located. In this sense the drop can be regarded as discretized in terms of the number of particles making up the suspension. Now we focus on the question how this drop discretization affects the break-up behavior of the suspension drop by varying the number of particles. The same integral drop properties, such as the bulk density and the particle volume fraction, can be realized by either a large number of small particles or a smaller number of larger particles. Thus, a different drop discretization in terms of the number of real particles involves different particle properties, e. g. the Stokes number increases with the particle radius under otherwise same conditions. For the case of  $Re_d = 100$  a set of simulations was performed with an increasing number of real (and computational) particles. Since for  $Re_d = 100$ ,  $St_d \leq 0.01$  and  $\Phi_v = 0.02$  the resulting numbers of real particles are very large (of order  $10^8$ ) we chose a fixed  $M = 130$ . The Froude number was  $Fr_d = 44.7$  in all cases. Table 3.4 shows the different parameters.

Fig. 3.18 shows the results. It is observed that the number of secondary blobs increases with an increasing number of particles used in the simulation. There are two effects of a finer initial drop discretization: (i) the excess mass of the suspension is more uniformly distributed throughout the drop, and (ii) the (natural) perturbations introduced by the discrete particle distribution extend to a smaller length scale due to a decreased mean particle spacing. Consequently, the torus remains

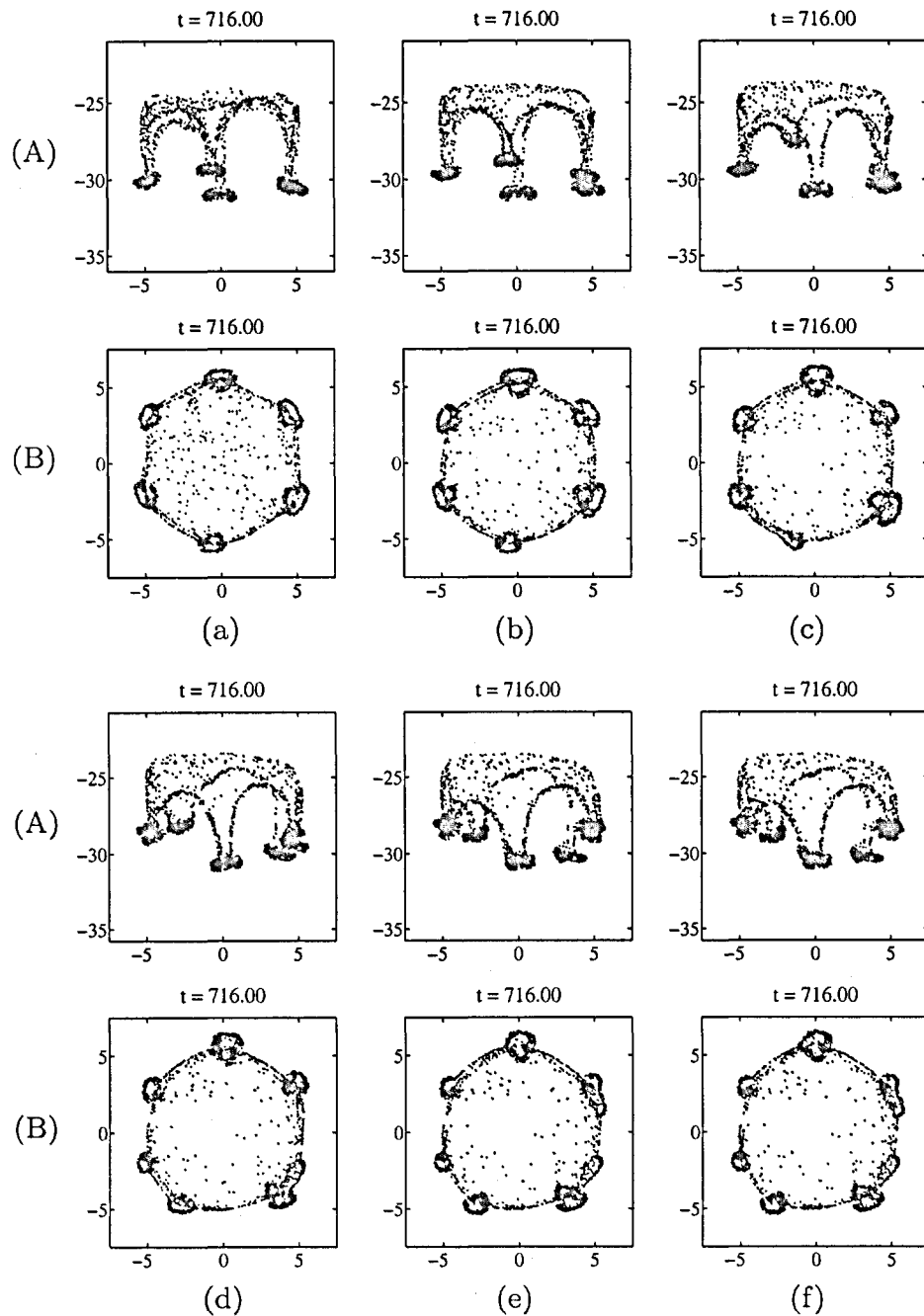


Figure 3.16: Disintegrated initially perturbed drops.  $Re_d = 100$ ,  $St_d = 0.01$ ,  $Fr_d = 44.7$ ,  $n_p^c = 29433$ ,  $M = 2251$ ,  $N = 64$ ,  $l_s = 6$ . (A) side view, (B) top view; (a)  $A_s = 0.1 R$ , (b)  $A_s = 0.05 R$ , (c)  $A_s = 0.025 R$ , (d)  $A_s = 0.01 R$ , (e)  $A_s = 0.001 R$ , and (f) unperturbed reference case. Initial mean particle spacing  $d \approx 0.052 R$ .

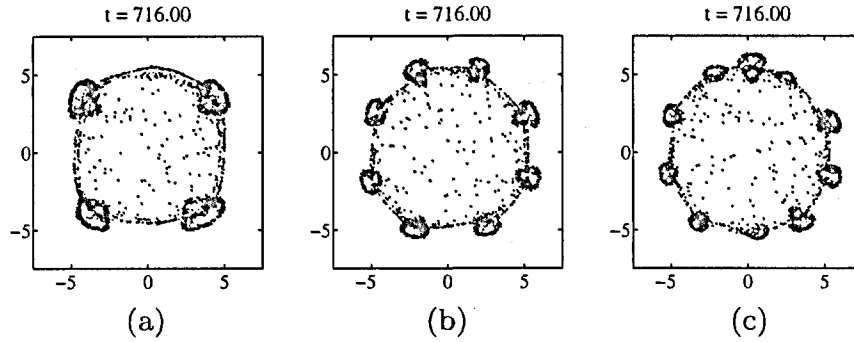


Figure 3.17: Forced number of secondary blobs of (artificially) perturbed suspension drops,  $Re_d = 100$ ,  $St_d = 0.01$ ,  $Fr_d = 44.7$ ,  $\phi = 0.02$ ; (a)  $l_s = 4$ , (b)  $l_s = 8$ , (c)  $l_s = 10$ ;  $A_s = 0.05 R$  in all cases. Natural (unperturbed) break-up into six secondary blobs as in Fig. 3.16(f).  $N = 64$ .

	$n_p^c$	$n_p^r$	$St_d$
(a)	509645	$\approx 66 \cdot 10^6$	0.01
(b)	$2 \cdot 10^6$	$260 \cdot 10^6$	0.00406
(c)	$4 \cdot 10^6$	$520 \cdot 10^6$	0.00253

Table 3.4: Number of computational and real particles and Stokes number for simulations with varying drop mass discretization.  $Re_d = 100$ ,  $Fr_d = 44.7$ ,  $\Phi_v = 0.02$ ,  $M = 130$ .

stable for a longer period of time, the visible break-up sets in at a later time (note the times given in Fig. 3.18 for the fully disintegrated drops). Comparison of the top views of cases (a) and (c) in Fig. 3.18 also reveals that the diameter of the disintegrated torus is larger in case (c), which provides additional room for a larger number of secondary blobs. It is concluded that for  $Re_d = 100$  an increased number of real (and computational) particles, i. e. a finer drop discretization, results in a larger number of secondary blobs due to a delayed torus break-up. A similar

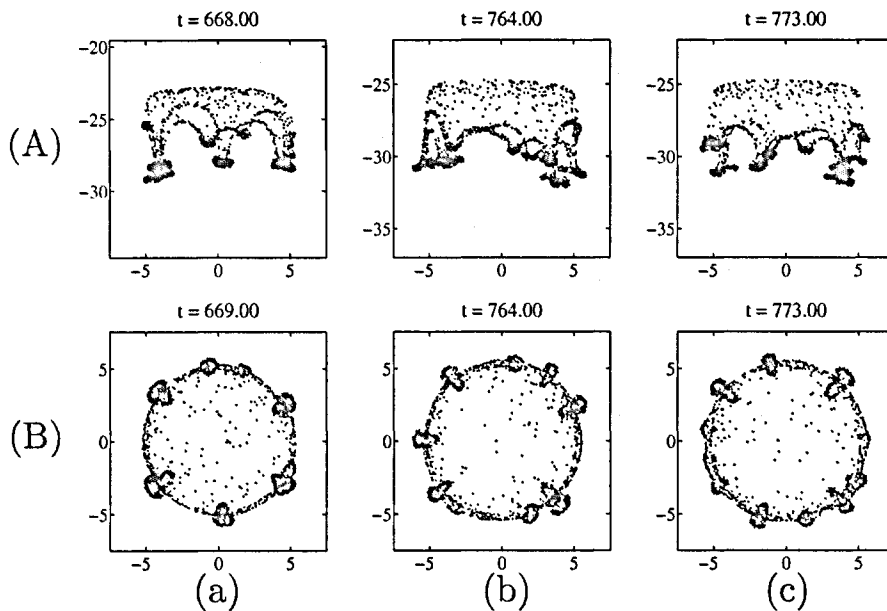


Figure 3.18: Influence of the number of computational particles. (A) side view, (B) top view of disintegrated drops; (a)  $n_p^c = 509645$ ; (b)  $n_p^c = 2 \cdot 10^6$ ; (c)  $n_p^c = 4 \cdot 10^6$ .  $Re_d = 100$ ,  $M = 130$ ,  $N = 128$  in all cases.

set of simulations with an increasing number of computational particles was performed for  $Re_d = 1$ . In this case the torus always breaks up into only two secondary blobs independently of the number of particles. This suggests that the range of possible disintegration patterns featuring a certain number of secondary blobs increases with increasing Reynolds number.

It is worth noting that the concept of computational particles offers a second possibility to examine the effect of a refined drop discretization. Instead of choosing a fixed ratio  $M$ , the number of computational particles can be augmented while keeping the number of real particles constant. The ratio  $M$  has to be adjusted accordingly. In this case the

particle properties do not change and it is obvious that this situation could not be reproduced in a real-world experiment. However, the effect of a finer drop mass discretization as “seen by the fluid” can as well be studied this way. A set of simulations was conducted with the number of computational particles successively increased from about  $5 \cdot 10^5$  to  $4 \cdot 10^6$  and a fixed number of real particles  $n_p^r \approx 6.625 \cdot 10^7$  ( $Re_d = 100$ ,  $St_d = 0.01$ ,  $N = 128$ ). The results revealed the same effect of a refined drop discretization as shown before. The torus disintegration is delayed resulting in an increased number of secondary blobs.

The findings discussed above necessitate a comment on the comparison between experiments and simulations. In a real-world experiment, in which a suspension drop is released into (roughly) quiescent fluid, the initial perturbations are not known. The particle distribution inside the suspension drop will certainly not be perfectly uniform and the drop will not have a perfectly well defined shape. Moreover, it is likely that other perturbations introduced by the apparatus to release the suspension drops (whatever its functional details) will be present. Thus, it is virtually impossible to match experimental and numerical conditions. Numerical simulations can predict a range of secondary blobs to be expected and possible break-up patterns. For example, in the case of  $Re_d = 100$  it is likely to obtain approximately six secondary blobs. This number, however, may vary significantly in a real-world experiment due to unknown perturbations and different initial conditions.

The strong sensitivity of the instability to the details of the initial conditions is a notable characteristic of the drop disintegration process. As already mentioned the growing perturbations in our simulations may not only be of a “physical” nature, such as a not perfectly homogeneous particle distribution, but also due to numerical effects. In the subsequent sections numerical influences are shown to be negligible thus confirming the results presented above.

### 3.2.4 Influence of the periodic boundaries

As has been shown for the low Reynolds number case,  $Re_d = 0.1$ , the periodic boundaries have a considerable effect on the drop settling velocity (hindered settling). Thus, it might be expected that they affect the break-up process in some general way such that, for example, the number of secondary blobs is influenced by the periodic boundaries. On

the other hand, the substructural effects of the particle–fluid interaction, the internal circulating motion, was well reproduced in the low Reynolds number case despite the periodic boundaries. This would suggest only a minor influence of the periodicity on the disintegration process. Fig. 3.19 shows disintegrated drops from two simulations with different inter-drop spacings under otherwise same conditions ( $Re_d = 100$ ,  $St_d = 0.01$ ,  $Fr_d = 44.7$ ,  $n_p^c \approx 10^5$ , same initial particle distribution). In the first case  $128^3$  grid points were used with  $L/R = 15$ , in the second case  $256^3$  grid points with  $L/R = 30$ . The higher grid resolution in the second case ensures a fixed drop resolution in terms of grid points per drop radius. The disintegrated torus looks very similar in both cases. Not only is the same number of secondary blobs obtained, but also the details are very similar. It is concluded that the periodic boundaries have a negligible effect on the break-up pattern of the suspension drop. Thus, the Reynolds number dependence and the role of the particle distribution discussed above should as well apply to the general case of a single suspension drop in infinite fluid.

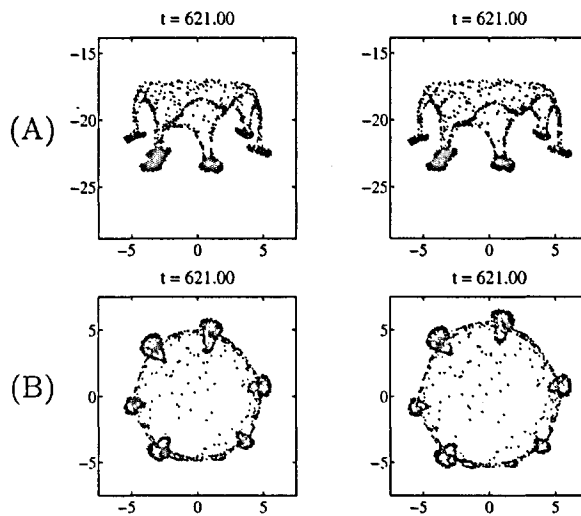


Figure 3.19: Influence of periodic boundaries. Two simulations at  $Re_d = 100$  ( $St_d = 0.01$ ,  $Fr_d = 44.7$ ,  $\phi = 0.02$ ) with the same initial particle distributions but different inter-drop spacing. Left:  $L/R = 15$ ,  $N = 128$ . Right:  $L/R = 30$ ,  $N = 256$ . The ratio of grid points per drop radius was equal in both simulations. (A) side view, (B) top view.

### 3.2.5 Influence of interpolation

Interpolation is used to compute the fluid velocity at the instantaneous particle positions and to distribute the particles' feedback force from the particle positions to the grid points of the Eulerian mesh. There are several studies available in the literature that examine the influence of interpolation in detail, primarily in turbulent particle-laden flows (e.g. Yeung & Pope (1988), Balachandar & Maxey (1989), Sundaram & Collins (1999), Kitagawa *et al.* (2001)). Here, we confine ourselves to demonstrating that the use of different interpolation methods does not significantly alter our results of suspension drop disintegration at moderate Reynolds numbers. For the fluid interpolation three different methods were employed: (i) trilinear interpolation, (ii) 4<sup>th</sup>-order Lagrange polynomials, and (iii) spectral summation, the details of which are given in Appendix B. These interpolation techniques were used alternatively in a set of simulations with otherwise same parameters ( $Re_d = 100$ ,  $St_d = 0.01$ ,  $Fr_d = 44.7$ ,  $n_p^c = 7337$ ,  $M = 9030$ ). The grid resolution was set to  $N = 64$ . In all cases linear interpolation was used to distribute the particle feedback force to the surrounding grid points. In the case of spectral summation a 3<sup>rd</sup>-order accurate Runge–Kutta scheme was employed for both the linear and nonlinear terms (instead of a combined Runge–Kutta Crank–Nicolson scheme). Thus, the overall accuracy of the time integration was augmented from second to third order.

The results are shown in Fig. 3.20. The hardly visible differences between cases (b) and (c) (Lagrange and spectral interpolation, respectively) are negligible. In the linear case (a) the number of secondary blobs is the same as in (b) and (c), however, their location is somewhat different. The principal features of the settling process, such as torus formation and break-up, are well captured in all three cases. Given the increased computational cost of Lagrange polynomial interpolation and spectral summation, it is reasonable to resort to linear interpolation. It should be noted that the influence of interpolation is significantly reduced if higher grid resolutions are used, e.g.  $N = 128$  as in the simulations shown in Fig. 3.6.

We also used first-order top hat interpolation to distribute the particle feedback force between the grid points. Here, the full feedback force of a particle is attributed to the closest grid point in its vicinity. The results did not show any major differences to those presented in Fig. 3.20.

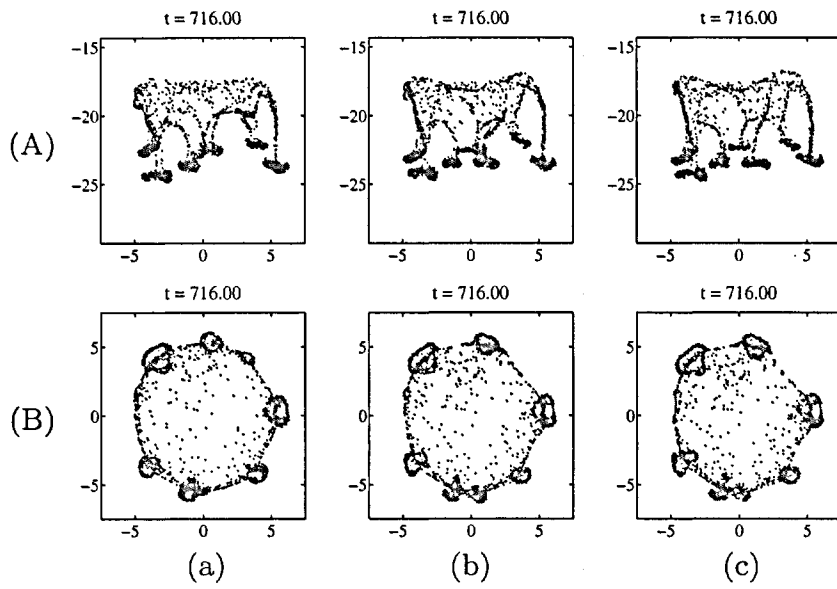


Figure 3.20: Influence of interpolation. Case (a): trilinear fluid interpolation, (b) 4th-order Lagrange-polynomial fluid interpolation, (c) spectral summation. In all cases trilinear interpolation of the particle feedback force was used.  $Re_d = 100$ ,  $St_d = 0.01$ ,  $Fr_d = 44.7$ ,  $n_p = 7337$ ,  $M = 9030$ ,  $N = 64$ .

### 3.2.6 Influence of the grid resolution

In numerical simulations reliable results are generally required to be independent of the grid resolution (grid convergence). To find a grid resolution fine enough to capture all relevant details of the disintegration process, a set of simulations with different numbers of grid points was performed. Fig. 3.21 shows examples for  $Re_d = 100$ . It was found that a resolution of  $64^3$  grid points is sufficient to capture all characteristic features of the settling and disintegration process, i. e. torus formation and break-up into a certain number of blobs depending on the Reynolds number. However, it is worth noting that grid convergence in a strict sense is not given. The instability is very sensitive to only small perturbations of the suspension torus. A different grid resolution involves different relative positions between particles and grid points resulting in a slightly different particle feedback force. This small difference is sufficient to produce different details of the disintegrating torus. For example, the location of the secondary blobs along the torus' circumference may be different in one simulation with  $N = 64$  and another one with  $N = 128$  and otherwise same parameters. Also, the disintegration process tends to evolve a little more slowly when using  $64^3$  grid points

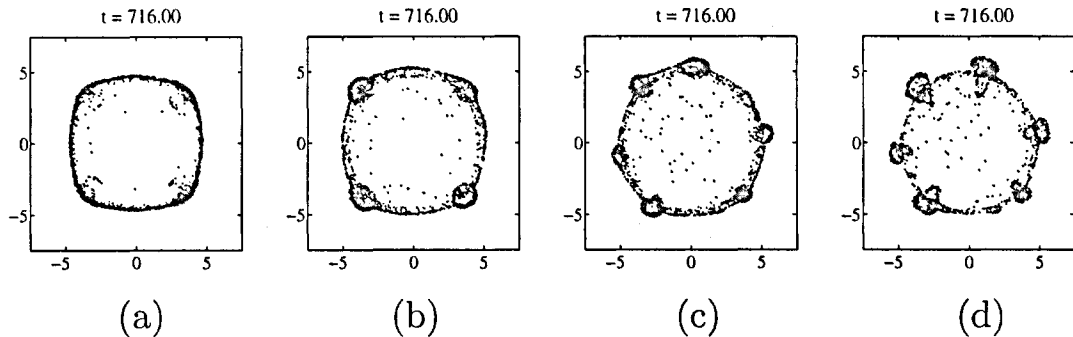


Figure 3.21: Disintegrated blobs computed with different grid resolutions. From left to right:  $N = 16$ ,  $N = 32$ ,  $N = 64$ ,  $N = 128$ .  $Re_d = 100$ .

compared to  $128^3$ .

### 3.2.7 Spectral analysis of settling drop and torus

The initial particle distribution has been identified as the primary source of perturbations, which are crucial to the instability developing during the drop settling process. To gain a deeper understanding of the particle dispersion processes involved, the particle field inside the settling drop and torus was analyzed from a spectral point of view. To this end the particle field was divided into  $N_s$  radially symmetric segments in the  $(x_1, x_2)$ -plane according to the sketch in Fig. 3.22. The segments are similar to the slices of an orange. This segmentation served as a tool to study the time evolution of the particle distribution.

The idea is to define a measurable quantity  $q(\theta_s, t)$  as a function of the segmentation angle  $\theta_s$  and time  $t$  and to study the time evolution of the Fourier coefficients associated with this quantity. Each segment contains a number of particles  $n_p^s(\theta_s, t)$  that may change during the disintegration process. As will be demonstrated in the following, it is instructive to use this number as the time-dependent quantity,  $q(\theta_s, t) := n_p^s(\theta_s, t)$ . The number of particles per segment indicates whether particles accumulate in certain azimuthal regions. Another choice would be to use the mean particle settling velocity per segment,  $q(\theta_s, t) := v_3^s(\theta_s, t)$ , which may indicate whether particles settle faster in certain regions.

A reasonable number of segments  $N_s$  must meet two criteria: (i) the size of a segment should be much smaller than the smallest scale of particle clustering to be captured along the torus' circumference; (ii) a segment should contain enough particles such that  $n_p^s$  does not change

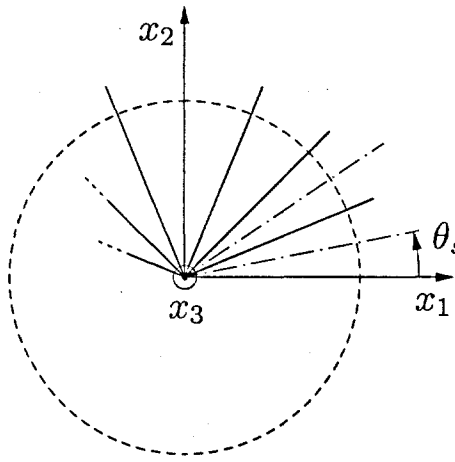


Figure 3.22: Axisymmetric segmentation of particle field in  $x$ - $y$ -plane. The dashed circle indicates the initial suspension drop. The angle  $\theta_s$ ,  $s = 1, \dots, N_s$  denotes the azimuthal location of the segments' center.

significantly if the segment is slightly shifted in azimuthal direction. This is to ensure that  $n_p^s$  is a measure of the local particle number density. Fig. 3.23 shows the mean number of particles per segment  $\bar{n}_p^s(N_s)$  and the corresponding standard deviation  $\sigma(N_s)$  for a simulation with  $n_p^c = 509645$  ( $Re_d = 100$ ,  $St_d = 0.01$ ,  $Fr_d = 44.7$ ,  $\phi = 0.02$ ). In this case the suspension drop breaks up into six secondary blobs. Thus, criterion (i) requires the number of segments  $N_s$  to be much larger than the order of 10. Criterion (ii) requires the ratio  $\sigma/\bar{n}_p^s$  to be much smaller than unity (Fig. 3.23). For the subsequent analysis  $N_s = 128$  was chosen.

The quantity  $q(\theta_s, t)$  is decomposed into its Fourier coefficients according to

$$\hat{q}(k, t) = \frac{1}{N_s} \sum_{\theta_s} q(\theta_s, t) e^{-ik\theta_s}, \quad (3.3)$$

where  $\hat{q}(k, t)$  is the Fourier coefficient associated with the azimuthal wavenumber  $k = -N_s/2, \dots, N_s/2 - 1$ . Since  $q(\theta_s, t)$  is a real quantity, the coefficients  $\hat{q}(k, t)$  and  $\hat{q}(-k, t)$  are complex conjugates. Therefore, the time evolution of the magnitude  $|\hat{q}(k, t)|^2$  needs to be studied for positive  $k$  only.

Fig. 3.24(a) shows the time evolution of the Fourier coefficients associated with the number of particles per segment ( $q(\theta_s, t) = n_p^s(\theta_s, t)$ ). From  $t \approx 100$  on all Fourier coefficients start growing. For  $100 \lesssim t \lesssim 400$  the increase is approximately linear in the logarithmic-linear plot indi-

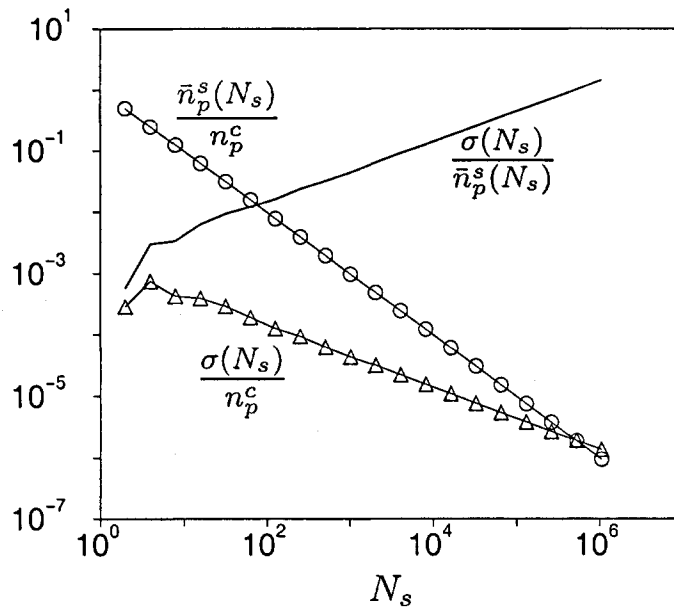


Figure 3.23: Mean number of particles per segment  $\bar{n}_p^s$  and standard deviation  $\sigma$  as a function of the number of segments  $N_s$  for initial suspension drop ( $\bar{n}_p^s$  and  $\sigma$  are normalized by the total number of particles  $n_p^c$ ).  $Re_d = 100$ ,  $N = 64$ ,  $n_p^c = 509645$ .

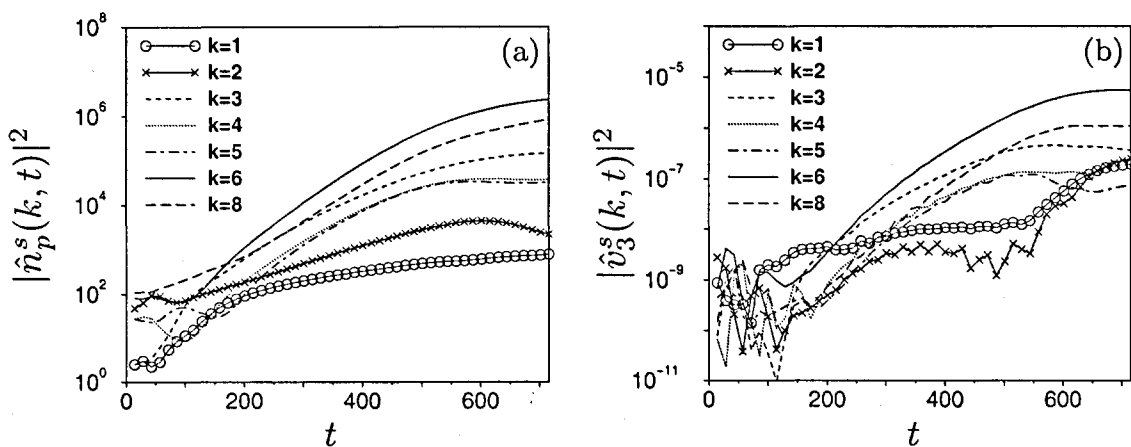


Figure 3.24: Time evolution of the Fourier coefficients associated with the number of particles per segment  $n_p^s(\theta_s, t)$  (a), and with the mean particle settling velocity  $v_3^s(\theta_s, t)$  (b). Same simulation as in Fig. 3.25.

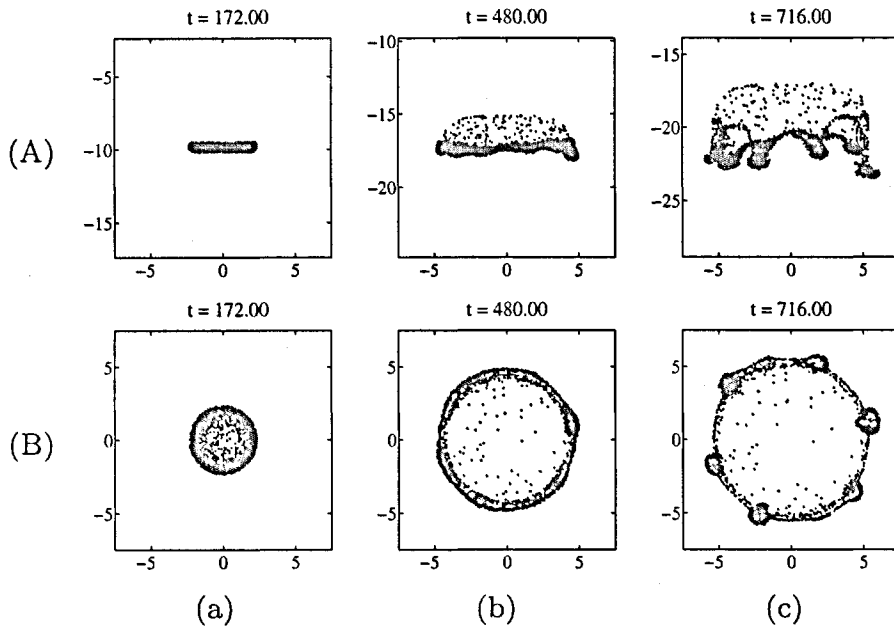


Figure 3.25: Suspension drop at (a)  $t = 172$ , (b)  $t = 480$ , and (c)  $t = 716$ .  $Re_d = 100$ ,  $St_d = 0.01$ ,  $Fr_d = 44.7$ ,  $n_p^c = 509645$ ,  $M = 130$ ,  $N = 64$ . (A) side view, (B) top view.

cating an exponentially growing instability. The Fourier coefficient associated with wavenumber  $k = 6$  clearly predominates. This reflects a torus break-up into six (major) secondary blobs, as shown in Fig. 3.25 (c). The second-strongest mode is associated with  $k = 8$  corresponding to the two additional (minor) secondary blobs in Fig. 3.25 (c). It is worth noting that only at  $t \approx 480$  the formation of bulges becomes visible when observing the settling torus (Fig. 3.25 (b)). The wavenumber selection, i. e. the onset of exponential growth with a certain mode predominating, occurs at a much earlier stage ( $t \approx 150$ ), when it is clearly impossible to predict the number of secondary blobs by visual judgment only (Fig. 3.25 (a)).

Fig. 3.24(b) shows the time evolution of the Fourier coefficients associated with the mean particle settling velocity per segment ( $q(\theta_s, t) = v_3^s(\theta, t)$ ). The overall picture observed is the same as that in Fig. 3.24(a). The predominant mode is associated with wavenumber  $k = 6$ , the second-strongest with  $k = 8$ , however only for  $t \gtrsim 500$ . Also, the point in time when the wavenumber selection occurs cannot be identified as clearly as in Fig. 3.24(a).

Imposing artificial perturbations on the initial drop, as discussed in

section 3.2.2, affects the time evolution of the Fourier coefficients. This is shown in Fig. 3.26. Here, the initial drop shape was perturbed according to Eq. (3.2) with  $A_s = 0.01 R$  and  $l_s = 4$ . The shape perturbation causes the fourth mode,  $k = 4$ , to grow rapidly shortly after the drop is released and then prevail during the entire settling process. The sixth mode  $k = 6$ , which is due to the natural perturbations caused by the particle distribution, starts growing in the same way as in the unperturbed case (Fig. 3.24). As the instability develops, the sixth mode “catches up” with the fourth mode such that at  $t = 716$  the corresponding Fourier coefficients reach the same level. This results in a disintegrated drop with six secondary blobs as shown in Fig. 3.27. If the artificial perturbation level is increased ( $A_s > 0.01 R$ ) the predominance of the fourth mode is more pronounced yielding only four secondary blobs. If  $A_s \ll 0.01 R$  the fourth Fourier coefficient in Fig. 3.26 drops below the sixth mode and the disintegrated drop looks almost like the unperturbed one in Fig. 3.25.

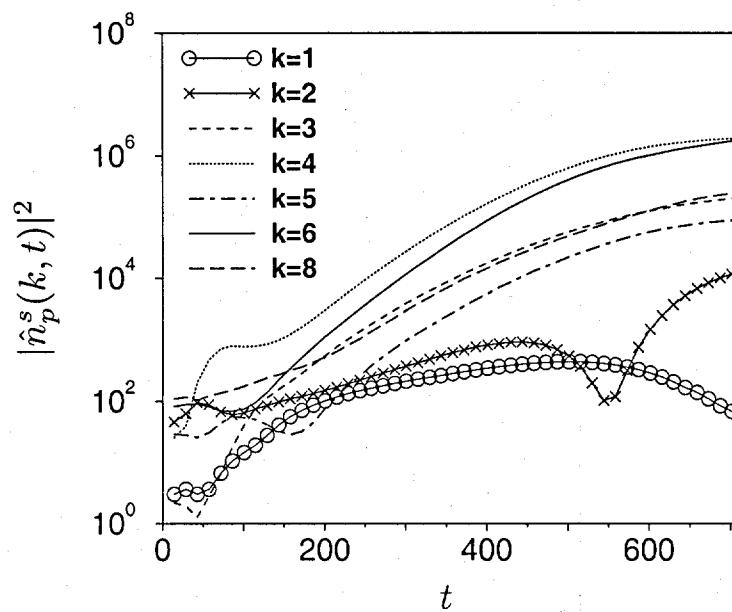


Figure 3.26: Time evolution of the Fourier coefficients associated with the number of particles per segment for an initially perturbed suspension drop. Same parameters as in Fig. 3.25 and  $A_s = 0.01 R$ ,  $l_s = 4$ .

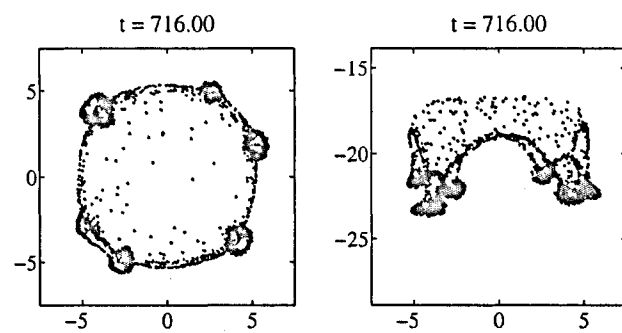


Figure 3.27: Initially perturbed suspension drop. Top view (left), side view (right). Same parameters as in Fig. 3.25 and  $A_s = 0.01 R$ ,  $l_s = 4$ .

**Seite Leer /  
Blank leaf**

# Chapter 4

---

## Particle settling in homogeneous turbulence

This chapter is concerned with the settling of small particles in homogeneous turbulence. As detailed in section 1.2 of the introduction, a considerable amount of research work has already been devoted to the effects of particle dispersion and turbulence modulation by micro-particles in turbulent flow environments. Nevertheless, there are still discrepancies and contradicting findings in the literature, in particular with respect to the mean settling velocity of particles in homogeneous turbulence. This is the subject of the following sections.

If a particle suspension is dilute enough with relatively low particle volume fraction, the effect of the particles on the fluid, i. e. a momentum transfer from the dispersed to the liquid phase, is negligible. In this case particle dispersion can be studied in one-way coupled simulations. Here, the particles are driven by surface forces exerted by the carrier fluid and volume forces such as gravity. The flow field, however, remains unchanged compared to a particle-free simulation under the same conditions, i. e. the particles do not exert any feedback force on the liquid phase. If the particle mass loading, i. e. the particle volume fraction and/or the density ratio (see Eq. (2.46)), is increased the effects of the particles on the fluid become important and may alter the fluid flow characteristics. In this case a two-way coupling approach is necessary to account for the particles' feedback forces (cf. section 2.2.2). The demarcation between one-way and two-way coupling is usually drawn with respect to the particle volume fraction  $\Phi_v$ . For  $10^{-6} \lesssim \Phi_v \lesssim 10^{-3}$  two-way coupling effects have to be accounted for (see e. g. Elghobashi (1994)). For suspensions with  $\Phi_v \gtrsim 10^{-3}$  particle-particle collisions may no longer be negligible in a turbulent flow and should be included in the numerical model. This is usually referred to as four-way coupling.

The following study is confined to the dilute regime with one-way and two-way coupling. In a first step the mean settling velocity in homogeneous, isotropic turbulence is studied for one-way coupling only. A comparison with the results by Wang & Maxey (1993) serves for validation purposes. In the second step two-way coupling effects are included in order to investigate the underlying physics linked to the mechanism responsible for an enhanced mean particle settling velocity. Finally, a

direct comparison with the experimental results by Aliseda *et al.* (2002) will be made by matching the simulation parameters as closely as possible to those in the experiments.

At the beginning of a simulation the particle distribution within the computational box was uniformly random and their initial velocity was set to the Stokes settling velocity. Gravity was applied in negative  $x_3$ -direction. The turbulent motion of the fluid was generated and kept statistically stationary by the forcing procedure described in section 2.4. To obtain desired turbulence properties such as a specific microscale Reynolds number  $Re_\lambda$  the forcing parameters have to be chosen appropriately. Unless otherwise indicated the parameters  $\varepsilon_L = 16.997$ ,  $T_L = 0.038$  and  $K_F = 2\sqrt{2}$  were kept fixed throughout all simulations and only the viscosity  $\nu$  was adjusted to obtain different turbulence intensities. This procedure is further explained in Appendix C.

In each time step the mean fluid velocity in each direction was set to zero. In  $x_3$ -direction this is equivalent to superposing a positive uniform pressure gradient that balances the net weight of all particles. As in the case of suspension drops this is necessary to keep the particles and the fluid from ever more accelerating in negative  $x_3$ -direction due to gravity.

For the time integration of the governing equations, Eqs. (2.5) and (2.13), the combined Runge–Kutta Crank–Nicolson (RK3CN) scheme was used. For details the reader is referred to Appendix A. Unless otherwise mentioned linear interpolation and the tent function were employed for the interpolation of fluid velocities and particle feedback forces, respectively (see Appendix B).

## 4.1 One-way coupling

In the case of one-way coupling the study of Wang & Maxey (1993) (hereafter referred to as W&M) is used for comparison and validation. It is well known that small heavy particles in a turbulent flow tend to accumulate in regions of low vorticity and high strain rate (Maxey (1987b), Maxey (1987a), Wang & Maxey (1993), Squires & Eaton (1991b), Yang & Lei (1998)). Due to Stokes drag forces and inertia the particles travel towards the peripheries of “individual” eddies. If, in addition, gravitational forces are present, the particle motion is subject to the mechanism of preferential sweeping. This means that the particles, accelerated in the direction of gravity, are swept preferably towards the regions of downward fluid motion when encountering an eddy. The net effect of this

preferential sweeping is an increase in the mean particle settling velocity compared to the free-fall velocity of a single particle in still fluid. This enhancement of particle settling velocity can be studied in one-way coupled simulations, i. e. for dilute suspensions with particle volume fractions  $\Phi_v \lesssim 10^{-6}$ .

The grid resolutions and corresponding forcing parameters were taken from the table 1 in Wang & Maxey (1993) to allow for a direct comparison of the results. The density ratio was  $\varrho_p/\varrho = 1000$  in all simulations.

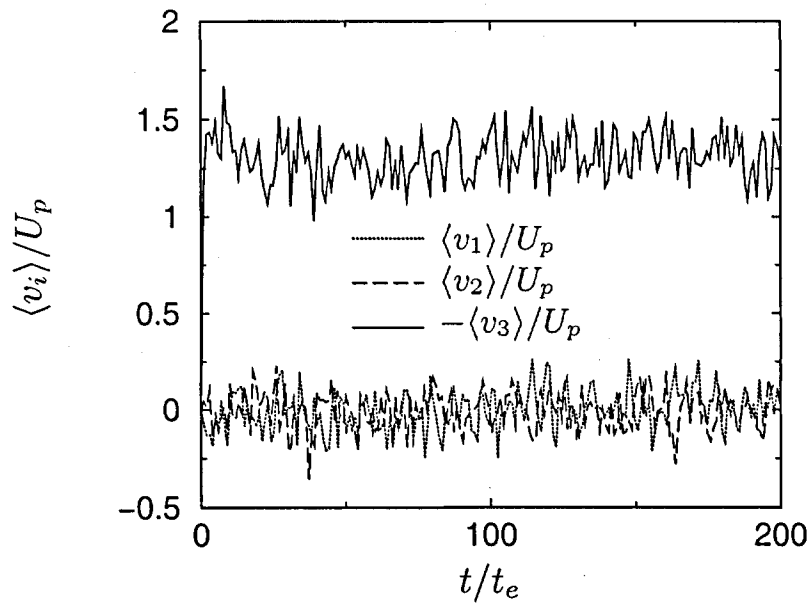


Figure 4.1: Mean particle velocities  $\langle v_i \rangle$  normalized by the Stokes settling velocity  $U_p$  as a function of time.  $Re_\lambda = 31$ ,  $St_\eta = 1$ ,  $U_p/u_\eta = 1$ ,  $N = 48$ .

Fig. 4.1 shows the time evolution of the mean particle velocities in the simulation with  $N = 48$ ,  $Re_\lambda = 31$ ,  $St_\eta = 1$ , and  $U_p/u_\eta = 1$ . Due to their initial velocity the particles experience an immediate increase in settling velocity. After a transient period of about 70 eddy turnover times the time average of the settling velocity converges to a statistically stationary value of about 1.3 times the Stokes settling velocity.

The settling velocity increase is defined here with respect to the Stokes settling velocity of a single particle as

$$\Delta V_3 := -\overline{\langle v_3 \rangle} - U_p \quad (4.1)$$

where the angle brackets  $\langle \cdot \rangle$  indicate an ensemble average over all particles at a certain point in time, and the over-bar  $\overline{\langle \cdot \rangle}$  denotes an additional

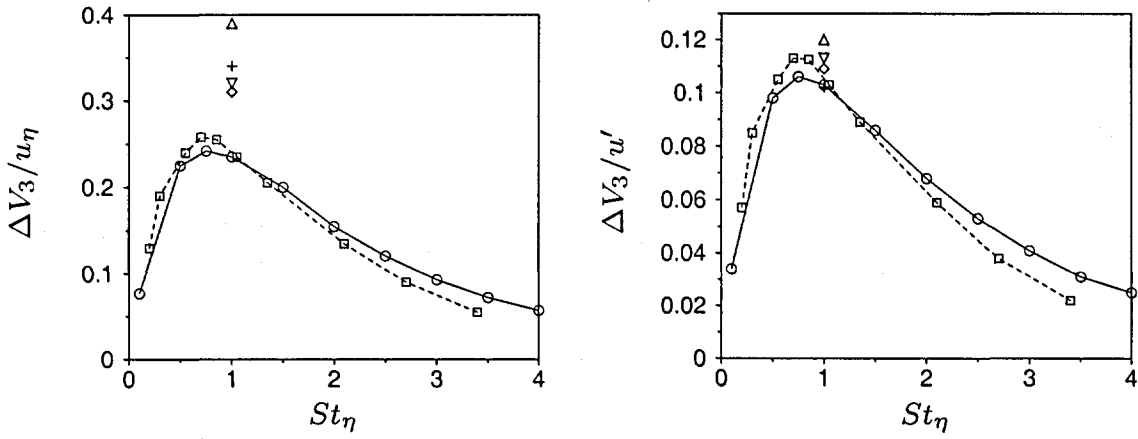


Figure 4.2: Increase in the mean particle settling velocity as a function of the Stokes number. The velocity enhancement is normalized by the Kolmogorov velocity scale (left) or the RMS velocity scale (right).  $Re_\lambda = 21$  ( $N = 32$ ):  $\square$  W&M,  $\bigcirc$  HIT (solid and dashed lines).  $Re_\lambda = 31$  ( $N = 48$ ):  $\triangledown$  W&M,  $\diamond$  HIT.  $Re_\lambda = 43$  ( $N = 64$ ):  $\triangle$  W&M,  $+$  HIT.

time average. Fig. 4.2 shows the relative increase in the mean settling velocity of particles for different particle Stokes numbers. The velocity enhancement is most pronounced for Stokes numbers around unity, i.e. when the particle response time is of the order of the Kolmogorov time scale. In the case of very small Stokes numbers the particle inertia becomes negligible and the particles respond almost immediately to changes in the velocity of their fluid neighborhood. Hence, there is no significant particle accumulation and the preferential sweeping has a negligible effect. As a result, the mean settling velocity is about the same as that of a single particle in quiescent fluid. If the Stokes number is increased beyond unity preferential sweeping is also less pronounced – in this case due to an increased particle inertia. These findings are in very good accordance with the results by W&M. In the case of  $Re_\lambda = 21$  ( $N = 32$ ) the velocity enhancement found in our simulations is slightly higher for Stokes numbers larger than unity and slightly smaller for Stokes numbers below unity compared to W&M. We also found a weak dependence on the microscale Reynolds number (only done for  $St_\eta = 1$ ,  $Re_\lambda = 31$ ,  $Re_\lambda = 43$ ), however less pronounced than that reported by W&M. It should be noted that in the case of  $Re_\lambda = 31$  ( $N = 48$ ) the latter used a different forcing scheme for comparison yielding the same qualitative features but quantitatively different by up to about 30 per-

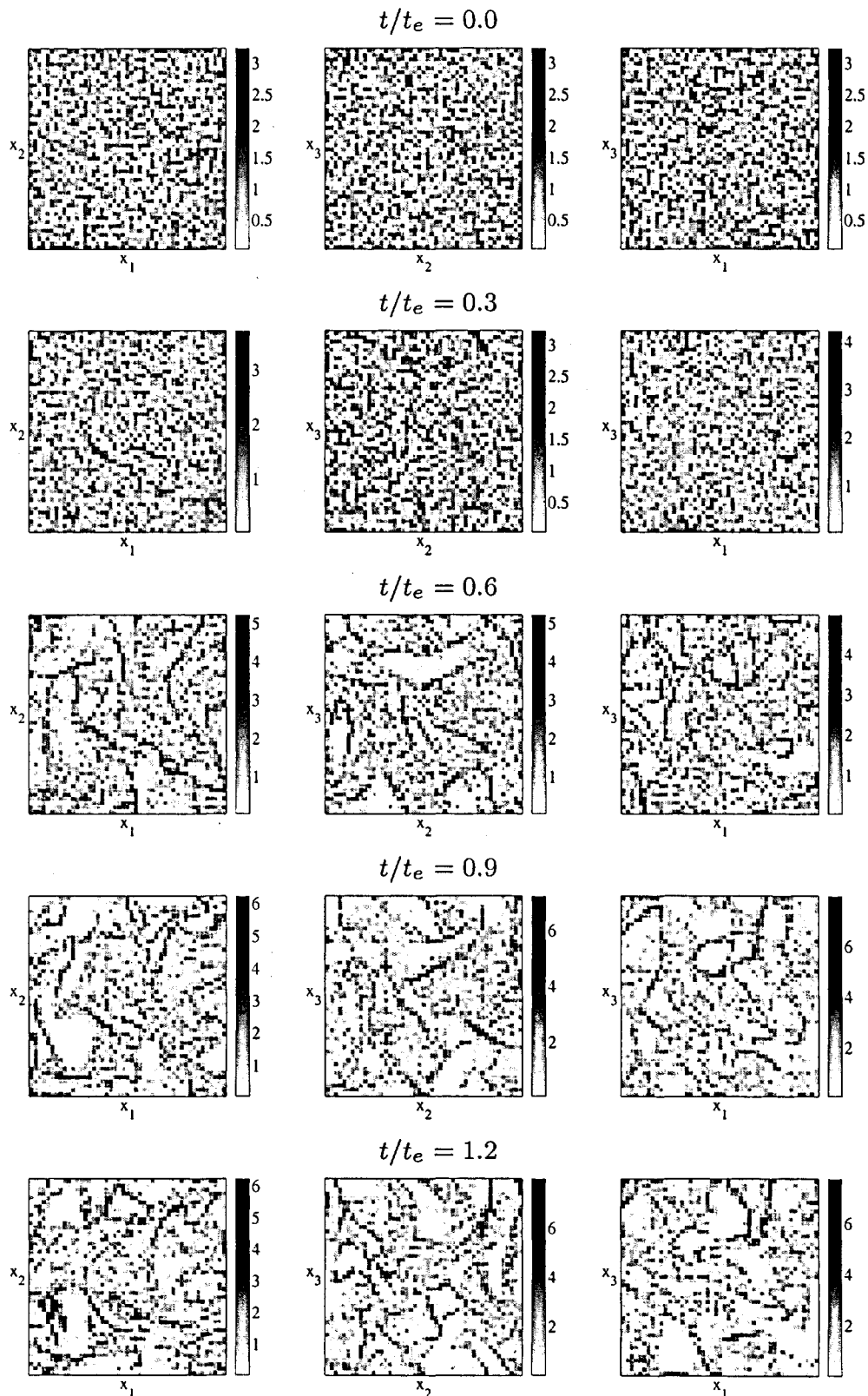


Figure 4.3: Normalized particle volume fraction  $\Phi_v^l/\Phi_v$  in slices of thickness  $3\Delta x_i$  cut through the center of the computational box (at  $x_i = \pi$ ). Left column:  $(x_1, x_2)$ -plane; middle column:  $(x_2, x_3)$ -plane; right column:  $(x_1, x_3)$ -plane.

cent. Thus, differences in the results may be related to a slightly different implementation of the forcing procedure and/or the solution algorithm. Also, W&M applied time averages over only a few eddy turnover times whereas in our simulation the sampling period was of the order of 100 eddy turnover times.

For the simulation with  $Re_\lambda = 31$  ( $N = 48$ ) Fig. 4.3 visualizes the initial evolution of the local particle volume fraction in slices cut through the center of the computational box. The slices' thickness is three grid cells ( $3 \Delta x_i$ ) and they are located at  $x_i = \pi$ . The local particle volume fraction is denoted by  $\Phi_v^l$  and computed by dividing the computational domain into  $N_b$  small boxes. The volume of such a sub-box is equal to the grid cell volume and the box center coincides with a grid point ( $N_b = N$ ). After the particles are released at  $t/t_e = 0.0$  it takes only about one eddy turnover time for the particles to "demix" resulting in large inhomogeneities in the local particle volume fraction. At  $t/t_e = 0.6$  regions of zero particle volume fraction are already discernible and become even more distinct as the simulation continues. The qualitative picture found at  $t/t_e = 1.2$  does not change in the further course of the simulation. The maximum local particle volume fraction  $\Phi_v^l(x_i)$  is about seven times the spatially averaged volume fraction  $\Phi_v$ . It should be noted that the preferential accumulation of the particles starting from a uniformly random distribution occurs much faster than the mean particle settling enhancement converges to a statistically stationary value. Typical simulation times for convergence are about 50 to 100 eddy turnover times whereas the particle accumulation, as discussed above, occurs on a time scale of the order of only one eddy turnover time.

To further quantify the preferential concentration of the particles, we introduce a probability function  $P_c(n_p^b)$ , which specifies the probability of finding a certain number of particles  $n_p^b$  (i.e. a certain volume fraction or concentration) within a sub-box. Following W&M we distinguish between four discrete events of finding zero, one, two, or more than two particles in a sub-box. Given the relatively small number of particles compared to the number of sub-boxes this is a reasonable choice. For example, in the simulation with  $Re_\lambda = 31$  ( $N = 48$ ) the number of particles was  $n_p^r = n_p^c = 147456$ , which is an average of 1.3 particles per grid cell or sub-box. As the particles accumulate the highest particle volume fractions involve about seven particles, the lowest zero particles per sub-box.

At the beginning of a simulation the particle distribution is uniformly

random. In this case the probability functions can be computed exactly from the binomial distribution

$$P_{binom}(n_p^b) = \binom{n_p^r}{n_p^b} \left(\frac{1}{N_b}\right)^{n_p^b} \left(1 - \frac{1}{N_b}\right)^{n_p^r - n_p^b}, \quad (4.2)$$

resulting in

$$\begin{aligned} P_{binom}(n_p^b = 0) &= 0.2636 \\ P_{binom}(n_p^b = 1) &= 0.3515 \\ P_{binom}(n_p^b = 2) &= 0.2343 \\ P_{binom}(n_p^b \geq 3) &= 0.1506. \end{aligned}$$

These analytical values are reproduced in the simulation for the initial distribution at  $t = 0$ . The time evolution of the probability functions  $P_c(n_p^b, t)$  is plotted in Fig. 4.4. Shortly after the particles are released all functions start deviating from their initial value. The strongest increase is observed for  $P_c(n_p^b = 0, t)$  reflecting large particle-free regions emerging from the initially uniform distribution. At the same time regions of high particle volume fraction are growing as indicated by an increase of  $P_c(n_p^b \geq 3, t)$ . Correspondingly, the other two probability functions decrease over time. For  $t/t_e \gtrsim 2$  the functions remain essentially stationary. This behavior of the probability functions supports the qualitative observation made in Fig. 4.3 that particles accumulate in certain regions (of high strain rate) creating large inhomogeneities in the particle distribution. Note that Fig. 4.4 is in very good qualitative agreement with figure 6 of W&M. The quantitative differences are primarily due to a different number of particles in the simulations (W&M:  $n_p^r = 131072$ , HIT:  $n_p^r = 147456$ ).

As a global measure for the particle accumulation the integrated square deviation between the computed and the analytical binomial distribution was introduced by W&M:

$$D_c(t) = \sum_{n_p^b=0}^{n_p^r} (P_c(n_p^b, t) - P_{binom})^2. \quad (4.3)$$

As displayed in Fig. 4.5 the global measure  $D_c(t)$  remains approximately constant at a value of about 0.13 for  $t/t_e \gtrsim 3$ . This agrees well with the result by W&M graphed in their figure 17.

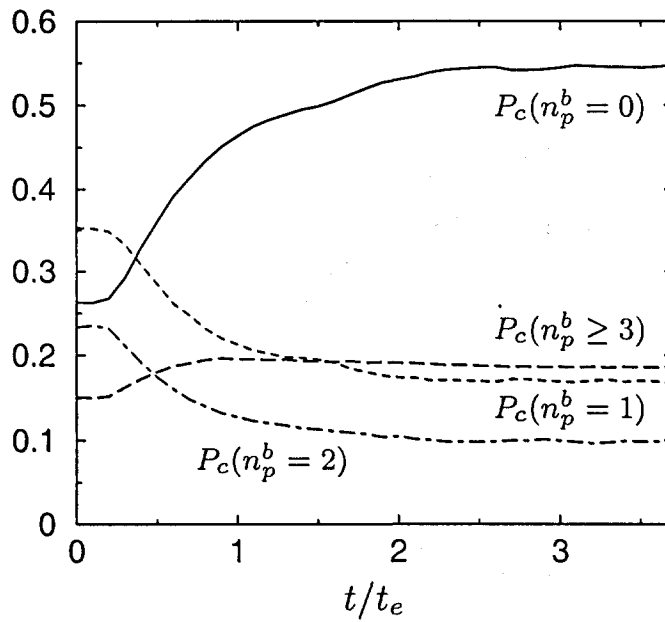


Figure 4.4: Time evolution of the probability functions describing the likelihood of finding a certain number of particles in a grid cell.  $Re_\lambda = 31$ ,  $N = 48$ ,  $St_\eta = 1$ ,  $U_p/u_\eta = 1$ , one-way coupling.

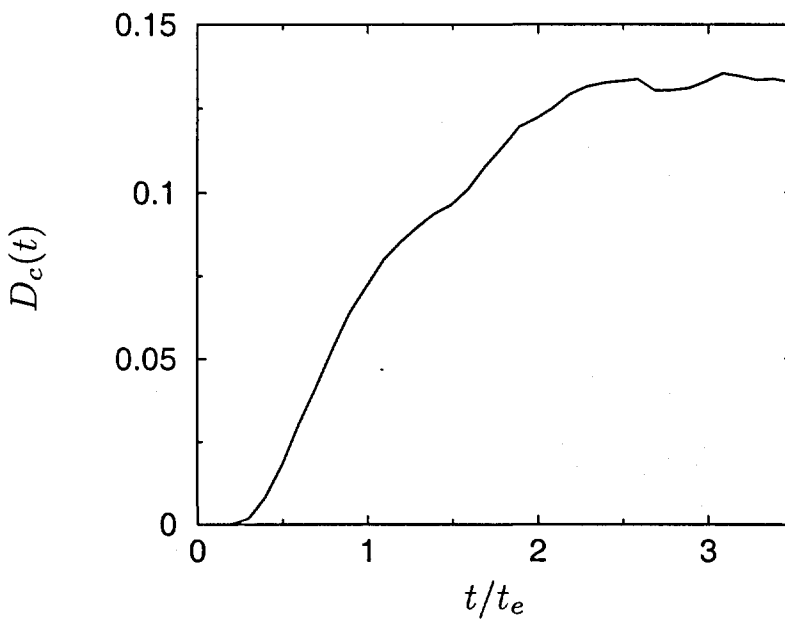


Figure 4.5: Time evolution of the global “dispersion function”  $D_c(t)$  describing the difference between the actual particle distribution in the simulation and the analytical binomial distribution.  $Re_\lambda = 31$ ,  $N = 48$ ,  $St_\eta = 1$ ,  $U_p/u_\eta = 1$ , one-way coupling.

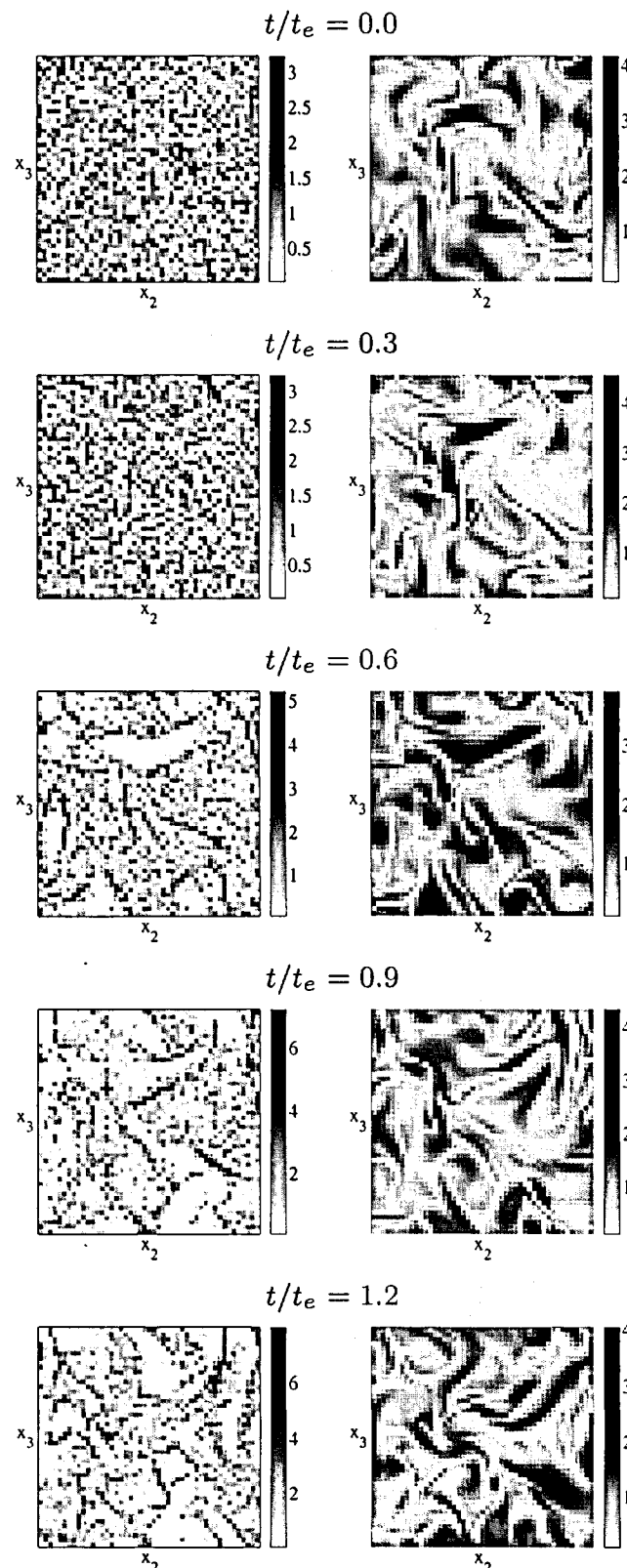


Figure 4.6: Correlation between normalized particle volume fraction  $\Phi_v^l / \Phi_v$  (left column, slices of thickness  $3 \Delta x_1$  cut through box center) and scalar vorticity  $\Omega$  (right column). The initial particle distribution is uniformly random.

Fig. 4.6 shows a comparison of the local particle volume fraction and the scalar vorticity defined as

$$\Omega := \frac{\sqrt{\omega_i \omega_i}}{\langle \sqrt{\omega_i \omega_i} \rangle}, \quad (4.4)$$

where  $\omega_i$  is the (vector) vorticity and the square brackets denote a spatial average. It is observed that areas of vanishing particle volume fraction correlate with regions of high vorticity. For example, this can clearly be seen for  $t/t_e = 0.6$  where the large white areas indicating particle-free regions in the left image correspond with the black regions of high vorticity in the right image. This result is also in line with W&M and other studies in the literature.

## 4.2 Two-way coupling

In order to study the effect of two-way coupling on the mean particle settling velocity a set of simulations with varying particle volume fraction and otherwise fixed parameters was performed. The Stokes number  $St_\eta$  and the dimensionless terminal velocity  $U_p/u_\eta$  were set to unity, for which a strong interaction level between dispersed phase and carrier fluid are to be expected. The density ratio was  $\rho_p/\rho = 5000$  in all simulations. The range of particle volume fractions relevant for our investigation is  $10^{-7} \lesssim \Phi_v \lesssim 10^{-4}$ . The suspension at the lower bound of  $\Phi_v \approx 10^{-7}$  is usually considered to be dilute enough to simulate the particle-fluid interaction in a one-way coupled approach (see e.g. Elghobashi (1994)). From  $\Phi_v \approx 10^{-6}$  on, two-way coupling effects may become important. As shown in the one-way coupled simulations presented above, the local volume fraction may increase during the simulation by about an order of magnitude compared to the mean volume fraction due to particle accumulation. Thus, the upper bound of  $\Phi_v \approx 10^{-4}$  is chosen such that the expected maximum local volume fraction does not exceed  $\Phi_v \approx 10^{-3}$ . This value is usually considered the limit where particle-particle collisions (four-way coupling) become important, which are not included in our numerical model. The grid resolution was chosen as small as possible to save on computational time. For the range of volume fractions investigated and a sufficiently large number of particles (of order  $10^5$ ) an initial microscale Reynolds number of  $Re_\lambda \approx 40$  is necessary for a consistent set of parameters. Accordingly, the grid resolution was set to  $N = 64$ . The number of computational particles was  $n_p^c = 100096$  in all

simulations. To account for the increasing number of real particles with growing volume fraction, the ratio  $M$  of real to computational particles was adjusted accordingly.

A simulation for a specific particle volume fraction consists of three parts. First, the forcing parameters are chosen to yield a desired microscale Reynolds number  $Re_\lambda$ . The simulation is run without particles to yield the quasi-stationary turbulence characteristics, such as the eddy turnover time and the Kolmogorov scales, required to form the desired particle parameters, i. e. the Stokes number and the dimensionless terminal velocity. Second, the particles are released into the fluid starting from a uniformly random distribution and the simulation is run with one-way coupling only. This yields particle statistics for comparison with the two-way coupled case. Third, two-way coupling is included in the simulation starting from an instantaneous velocity and particle field of the foregoing one-way coupled run. This has the advantage that particle and (changing) fluid statistics converge more quickly than in a simulation started from a zero velocity field and random particle positions. It should be noted that fluid turbulence quantities can change once the two-way coupling is active. Thus, the turbulence statistics characterized by  $Re_\lambda$ ,  $\eta$ ,  $t_e$  etc. are only known a posteriori. (In particular, this can involve a tedious trial-and-error process to match certain experimental conditions.)

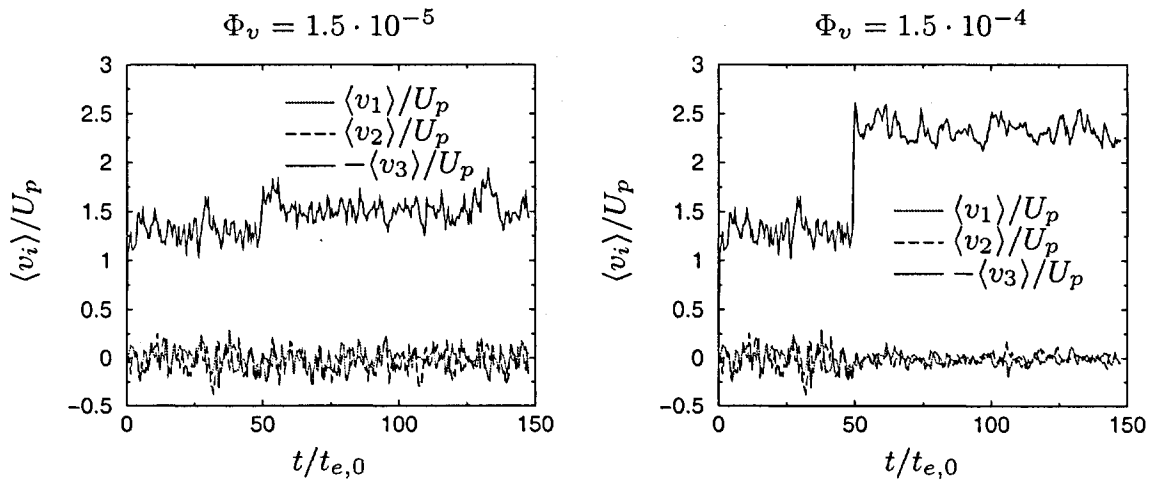


Figure 4.7: Time evolution of mean particle velocities normalized by the terminal settling velocity  $U_p$ . At  $t/t_{e,0} \approx 50$  the phase coupling was switched from one-way to two-way coupling ( $t_{e,0}$  denotes the eddy turnover time in the one-way coupling regime).

Fig. 4.7 shows the time evolution of the mean particle velocities for two different particle volume fractions,  $\Phi_v = 1.5 \cdot 10^{-5}$  and  $\Phi_v = 1.5 \cdot 10^{-4}$  (initial  $Re_\lambda \approx 42$ , see also Tab. 4.1, runs #2 and #7). At  $t/t_{e,0} \approx 50$  the phase coupling was switched from one-way to two-way coupling. (Here,  $t_{e,0}$  denotes the eddy turnover time in the one-way coupling regime. This time scale was chosen for non-dimensionalization since the turbulence characteristics may change in the two-way coupling regime.) For one-way coupling we observe an already increased mean particle settling velocity compared to the Stokes settling velocity. This is due to the mechanism of preferential sweeping as explained in the previous section. Once the particles are allowed to exert a feedback force onto the fluid, a further, almost immediate enhancement of the mean settling velocity is found (at  $t/t_e \approx 50$ ). This enhancement is more pronounced in the case of the larger particle volume fraction, where the settling velocity is increased by a factor of about 2.3 compared to the Stokes velocity. In both cases the mean velocities in directions  $x_1$  and  $x_2$  fluctuate around zero, which is in accordance with the isotropic conditions and a vanishing mean fluid velocity in planes perpendicular to the direction of gravity.

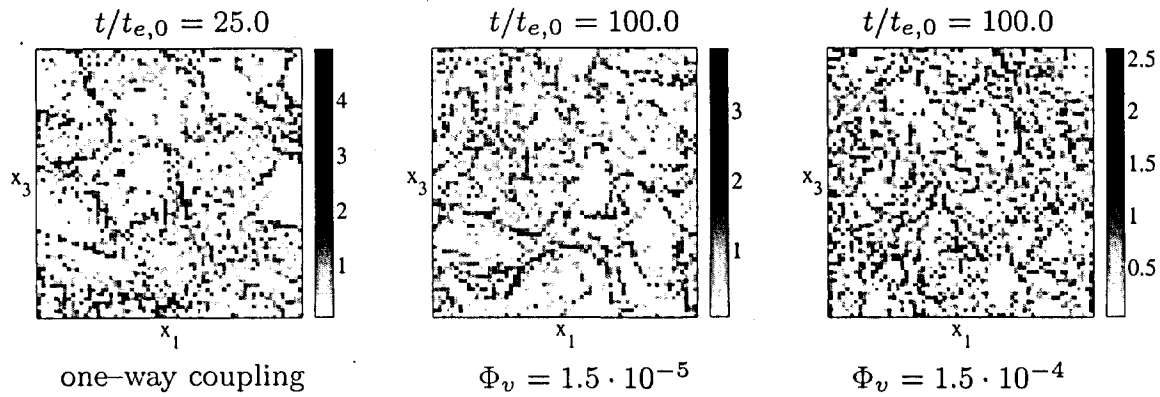


Figure 4.8: Normalized particle volume fraction  $\Phi_v^l/\Phi_v$  in slices of thickness  $3 \Delta x_2$  cut through the center of the computational box (at  $x_2 = \pi$ ). Left: one-way coupling; middle and right: two-way coupling. Same simulations as shown in Fig. 4.7.

The local particle volume fractions  $\Phi_v^l/\Phi_v$  of the same simulations as in Fig. 4.7 are visualized in Fig. 4.8. The particle volume fraction is shown in a slice cut through the computational box at  $x_2 = \pi$  at two different times,  $t/t_e = 25$  in the one-way coupling regime and  $t/t_e = 100$  in the two-way coupling regime. In the case of  $\Phi_v = 1.5 \cdot 10^{-5}$

there are no discernable differences in the overall qualitative structure of the inhomogeneous particle distribution. In both cases the particles accumulate in certain regions where the local particle volume fraction can be up to about four times higher than the average volume fraction. The size of the typical particle-free areas is very similar in both cases. Thus, the visible structure of inhomogeneities in the particle distribution does not allow any inference whether one-way or two-way coupling is present. In the case of  $\Phi_v = 1.5 \cdot 10^{-4}$  the typical size of the particle-free regions appears somewhat smaller than in the previous case. This is due to a reduced microscale Reynolds number as a consequence of the particle fluid interaction, which involves a smaller eddy length scale. Thus, the overall volume of the regions of high particle concentration (low vorticity) increases and the maximum particle volume fraction reduces to about 2.5 times the average. The turbulence modulation by the particles will be further discussed below.

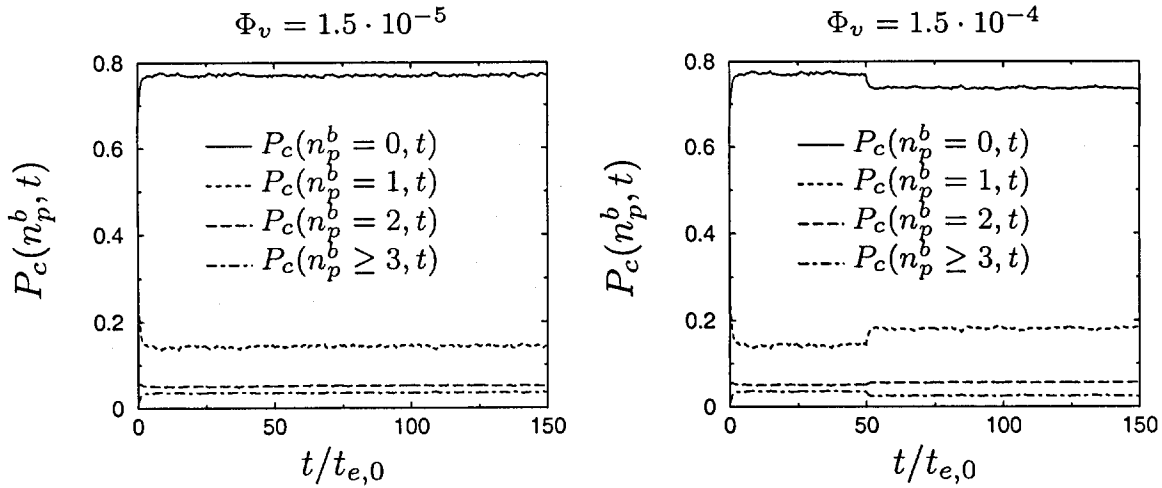


Figure 4.9: Time evolution of the probability functions  $P_c(n_p^b, t)$ . At  $t/t_{e,0} \approx 50$  the phase coupling was switched from one-way to two-way coupling. Initial  $Re_\lambda = 42$ ,  $N = 64$ .

The time evolution of the probability functions  $P_c(n_p^b, t)$ , introduced in the previous section, corroborates the qualitative observations of the particle dispersion (Fig. 4.9). Again, in the case of  $\Phi_v = 1.5 \cdot 10^{-5}$  there are no discernable differences between the one-way and the two-way coupling regime. In the case of  $\Phi_v = 1.5 \cdot 10^{-4}$  the onset of the two-way coupling regime is characterized by a small shift of all four probability functions displayed. According to the changing turbulence properties

involving smaller eddy length scales, the probability of finding particle-free regions decreases slightly while that of finding one particle per cell increases. The occurrence of higher particle volume fractions changes only little.

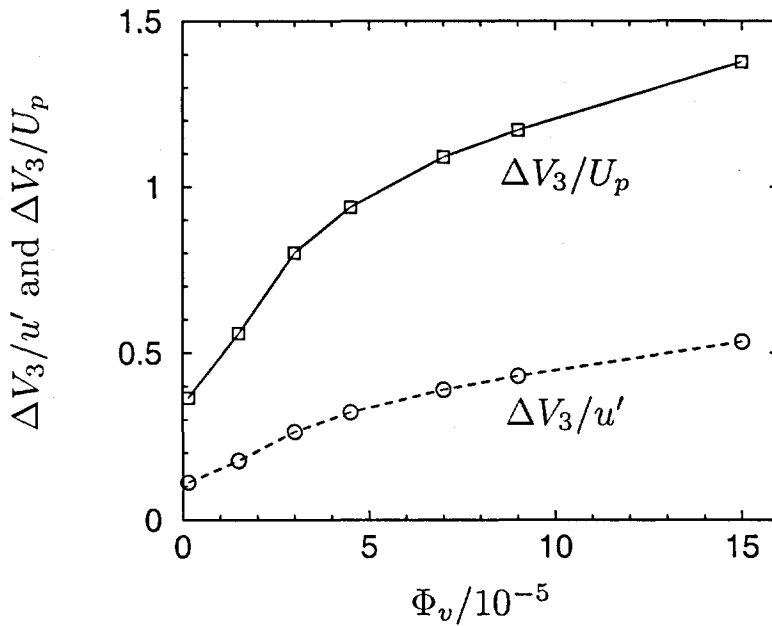


Figure 4.10: Particle settling velocity enhancement as a function of the particle volume fraction (two-way coupling). Simulations were started from a fully turbulent flow field with one-way coupled particles. Initial parameters:  $Re_\lambda = 42$ ,  $St_\eta = 1.0$ ,  $U_p/u_\eta = 1.0$ .  $N = 64$  in all cases.

Fig. 4.10 shows the enhancement of the particle settling velocity as a function of the particle volume fraction in the case of two-way coupling. The range of particle volume fractions covered is  $1.5 \cdot 10^{-6} \leq \Phi_v \leq 1.5 \cdot 10^{-4}$ . As before the settling velocity difference  $\Delta V_3$  is normalized by either the Stokes settling velocity or the fluid RMS velocity. If the particle volume fraction is very small, i. e.  $\Phi_v \leq 1.5 \cdot 10^{-6}$ , the increase in the particle settling velocity is negligible compared to the one-way coupled regime. Thus,  $\Phi_v \approx 10^{-6}$  can be considered the limit where two-way coupling effects come into play and start affecting the fluid-particle interaction. This confirms common observations found in the literature, see e. g. Elghobashi (1994).

As long as the overall turbulence properties are not significantly influenced by the feedback forces of the particles, the enhancement of the particle settling velocity increases with an approximately constant

slope as a function of the particle volume fraction. This is observed for  $1.5 \cdot 10^{-6} \leq \Phi_v \lesssim 3 \cdot 10^{-5}$  in Fig. 4.10. In this range the particle and turbulence properties remain roughly constant for fixed forcing parameters. If the particle volume fraction is further increased the slope of the curve decreases and the settling velocity enhancement is less pronounced. The strongest velocity enhancement is found for the largest particle volume fraction in the range covered,  $\Phi_v = 1.5 \cdot 10^{-4}$ . Here, the increase is almost one and a half times the Stokes settling velocity.

For all simulations the particle velocity enhancement and some turbulence properties are summarized in Tab. 4.1. The overall observation is that the introduction of small particles into the turbulent carrier fluid has a dissipative effect on the turbulence for particle volume fractions  $\Phi_v \gtrsim 3 \cdot 10^{-5}$ . This involves a change of essentially all relevant turbulent quantities, such as the turbulent kinetic energy and dissipation rate, the Kolmogorov scales, the eddy length and time scale, and other integral scales. As a result the microscale Reynolds number drops below its value in the one-way coupled case reflecting a decrease in the overall turbulence “level”. It is worth emphasizing that turbulence modulation is shown here to occur for particle volume fractions as low as  $\Phi_v \approx 5 \cdot 10^{-5}$ . This is in contradiction to Aliseda *et al.* (2002), who claim that “the range of volumetric fractions used in all the experiments reported here is such that the turbulence is not significantly affected by the presence of the particles, ...” (they used volume fractions of up to  $\Phi_v \approx 7 \cdot 10^{-5}$ ).

For a better illustration of the turbulence modulation with increasing particle volume fraction some characteristic turbulent quantities are displayed separately in Figs. 4.11 through 4.17. The microscale Reynolds number decreases due to a decrease of both the RMS velocity  $u'$  and the Taylor microscale  $\lambda$  (Fig. 4.11). It is interesting to note that the Kolmogorov scales hardly change with increasing particle volume fraction, whereas the eddy turnover time and length scale decrease considerably (by up to 58%, Tab. 4.1). The former observation indicates that the particles interact primarily with turbulent structures larger than the smallest ones. Indeed, the visualization in Fig. 4.8 suggests a typical length scale of the particle inhomogeneities larger than the Kolmogorov length. As shown by Wang & Maxey (1993), Yang & Lei (1998) and others this length scale is of the order of  $10\eta$ , which is consistent with Fig. 4.8. In fact, Yang & Lei demonstrated that the preferential accumulation can accurately be predicted in a large-eddy simulation (LES) with the Kolmogorov scales not resolved by the computational grid. The decrease of

run # $\Phi_v/10^{-5}$	one-way				two-way				max. $\Delta$ [%]
	0	< 0.1	1	1.5	3	4	5	6	
$Re_\lambda$	42.70	42.56	41.96	39.90	37.04	33.61	30.75	24.50	42.6
$\lambda$	0.595	0.596	0.606	0.608	0.591	0.554	0.522	0.435	26.9
$u'$	8.42	8.32	8.02	7.69	7.37	7.11	6.90	6.56	22.1
$q$	105.5	103.5	96.2	88.0	80.6	75.2	70.9	64.4	39.0
$\varepsilon$	354.0	342.0	307.5	282.5	275.7	290.1	308.1	397.8	22.1
$\eta$	0.0465	0.0465	0.0478	0.0492	0.0497	0.0488	0.0481	0.0448	6.9
$u_\eta$	2.549	2.528	2.452	2.410	2.402	2.426	2.463	2.616	2.6
$t_\eta$	0.0184	0.0186	0.0196	0.0206	0.0210	0.0204	0.0197	0.0172	14.1
$l_e$	1.678	1.686	1.678	1.603	1.441	1.230	1.060	0.709	57.7
$t_e$	0.201	0.204	0.210	0.210	0.198	0.175	0.155	0.108	46.3
$l_I$	1.168	1.172	1.182	1.195	1.198	1.203	1.196	1.144	3.0
$t_I$	0.140	0.142	0.148	0.157	0.165	0.171	0.175	0.175	25.0
$q_1$	102.5	102.4	92.4	88.0	77.2	67.5	61.8	48.8	52.4
$q_2$	105.5	103.4	93.9	84.9	76.4	69.0	61.8	48.4	54.1
$q_3$	108.2	104.6	102.3	96.2	88.2	89.0	88.9	95.8	18.5
$q$	105.4	103.5	96.2	88.0	80.6	75.2	70.9	64.4	38.8
$St_\eta$	1.0	0.99	0.94	0.88	0.88	0.92	0.92	1.08	12.0
$U_p/u_\eta$	1.0	1.0	1.04	1.05	1.06	1.05	1.03	0.97	6.0
$\Delta V_3/U_p$	0.355	0.366	0.558	0.801	0.938	1.091	1.171	1.378	288.2
$\Delta V_3/u'$	0.107	0.112	0.177	0.264	0.323	0.390	0.431	0.534	399.6

Table 4.1: Turbulent flow and particle quantities of simulations shown in Fig. 4.10. Two-way coupled simulations (runs #1–7) were started from a fully turbulent flow field with one-way coupled particles (run #0).  $\tau_p = m_p/(6\pi\mu r) = 0.0184$ ,  $|U_p| = 2.5407$ .

the eddy time and length scales, on the other hand, is primarily due to the damped velocity fluctuations  $u'$  (cf. the definitions (D.10) and (D.11) in Appendix D).

The presence of gravity introduces an anisotropy that alters the initially isotropic fluid velocity field by particle drag forces. This becomes obvious when comparing the turbulent kinetic energies associated with the three spatial directions,  $q_i$ ,  $i = 1, 2, 3$  (Fig. 4.13, left). While the energies in the directions perpendicular to gravity are reduced with increasing  $\Phi_v$ , the energy in the direction of particle settling remains roughly constant for  $\Phi_v \gtrsim 3 \cdot 10^{-5}$ . The dissipative effect of the particles is most evident in the mean turbulent kinetic energy  $q$ , which is significantly reduced with growing particle volume fraction (Fig. 4.13, left). The dissipation rate  $\varepsilon$ , however, decreases for volume fractions  $\Phi_v \lesssim 5 \cdot 10^{-5}$  and then increases again for higher volume fractions (Fig. 4.13, right). For  $\Phi_v = 1.5 \cdot 10^{-4}$  it is even larger than in the one-way coupled case. This is only possible, because the particles interact primarily with the small-scale fluid structures (although not with smallest ones as discussed above). That means the particles' effect is not uniform but selective with respect to the range of represented wavenumbers. This can be confirmed by analyzing the energy and dissipation spectra, which are plotted in Figs. 4.16 and 4.17 for particle volume fractions  $\Phi_v = 1.5 \cdot 10^{-5}$  and  $\Phi_v = 1.5 \cdot 10^{-4}$ , respectively. In the first case the influence of the particles on the spectral distribution of turbulent kinetic energy and dissipation is negligible. Correspondingly, the turbulence properties are essentially not affected by the presence of the particles (Tab. 4.1, run #2). In the second case with the particle volume fraction larger by one order of magnitude we observe a significant spectral redistribution of kinetic energy with respect to the shape of the spectra. The energy and dissipation associated with the small scales (high wavenumbers) increase, while those associated with the large scales decrease. This phenomenon is sometimes referred to as “pivoting” and has been reported in the literature by different authors (e. g. Squires & Eaton (1990), Elghobashi & Truesdell (1993)).

Fig. 4.18 shows the enhancement of the particle settling velocity over the particle volume fraction if the microscale Reynolds number is fixed at  $Re_\lambda \approx 42$ . For comparison the dashed lines indicate the same relation in the case where the microscale Reynolds number reduces with increasing particle volume fraction due to turbulence modulation by the particles (as already discussed, cf. Fig. 4.10). In the former case the forcing pa-

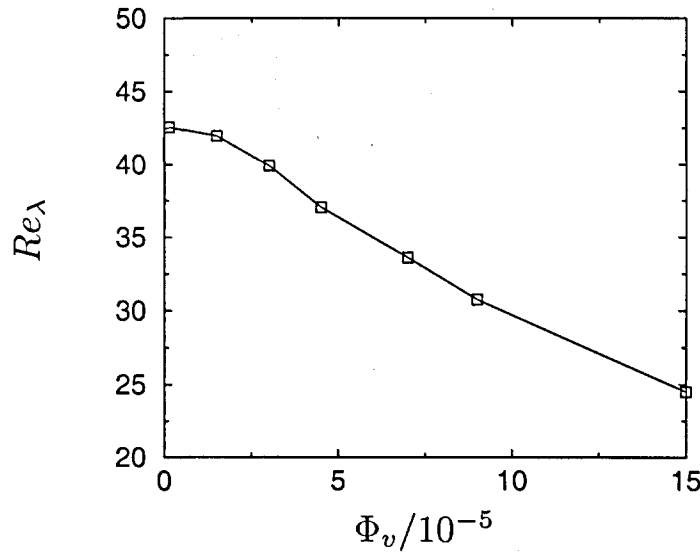


Figure 4.11: Microscale Reynolds number  $Re_\lambda$  as a function of the particle volume fraction (same set of simulations as in Fig. 4.10).

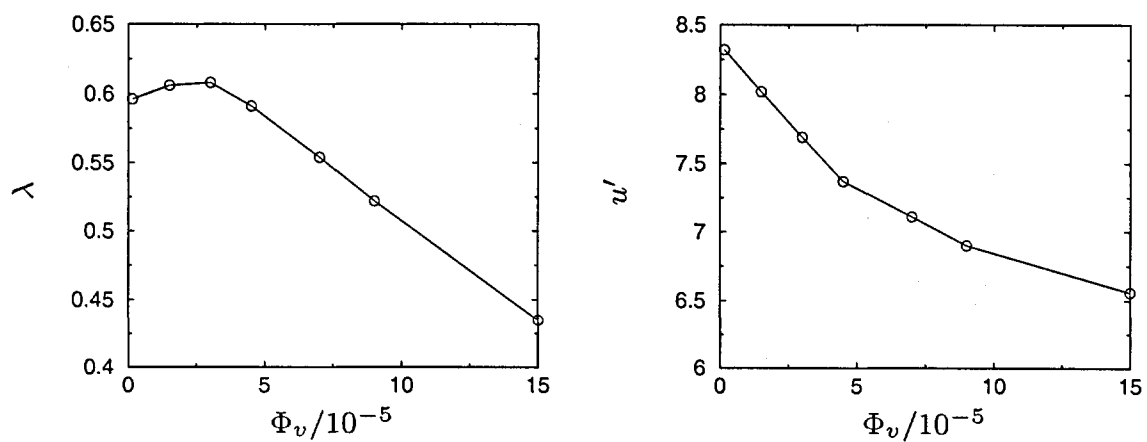


Figure 4.12: Taylor microscale  $\lambda$  (left) and RMS velocity  $u'$  (right) as a function of the particle volume fraction (same set of simulations as in Fig. 4.10).

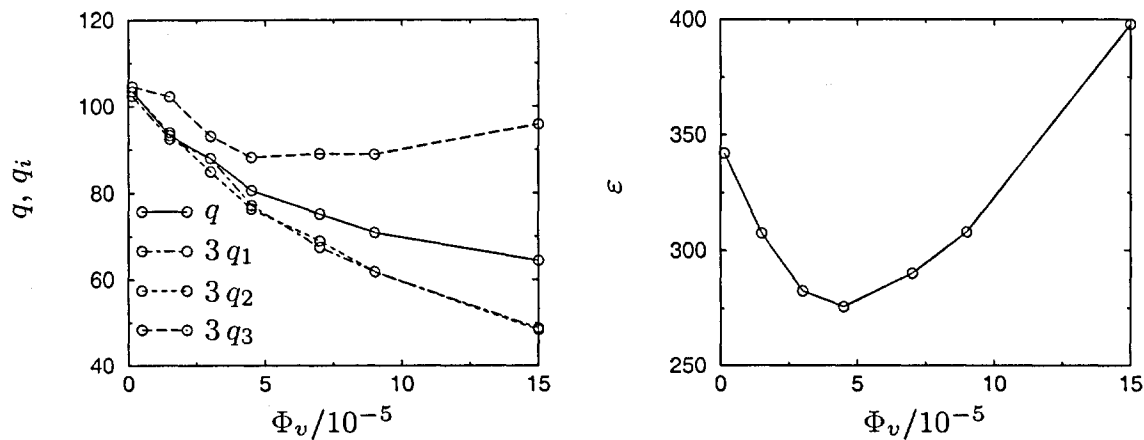


Figure 4.13: Left: mean turbulent kinetic energy  $q$  and kinetic energies  $q_i$  averaged in directions  $i = 1, 2, 3$  as a function of the particle volume fraction. Right: dissipation rate  $\epsilon$  (same set of simulations as in Fig. 4.10).

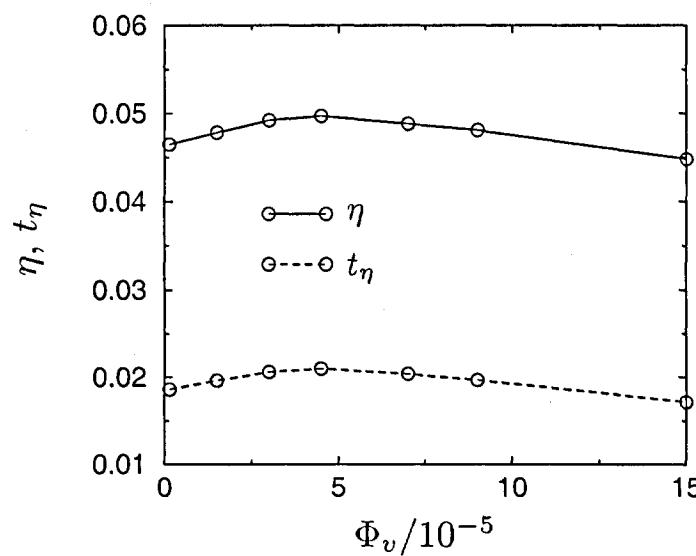


Figure 4.14: Kolmogorov length scale  $\eta$  and time scale  $t_\eta$  as a function of the particle volume fraction (same set of simulations as in Fig. 4.10).

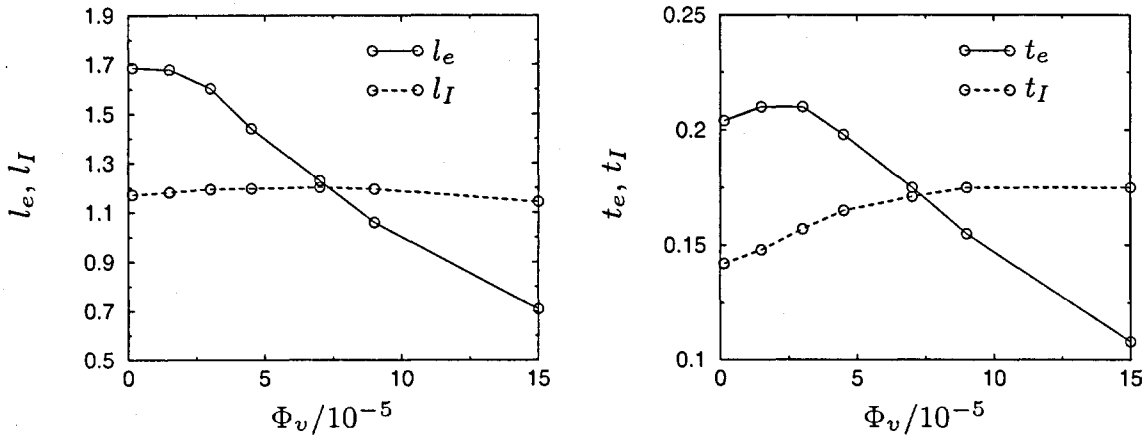


Figure 4.15: Integral length scales (left) and integral times (right) as a function of the particle volume fraction (same set of simulations as in Fig. 4.10).

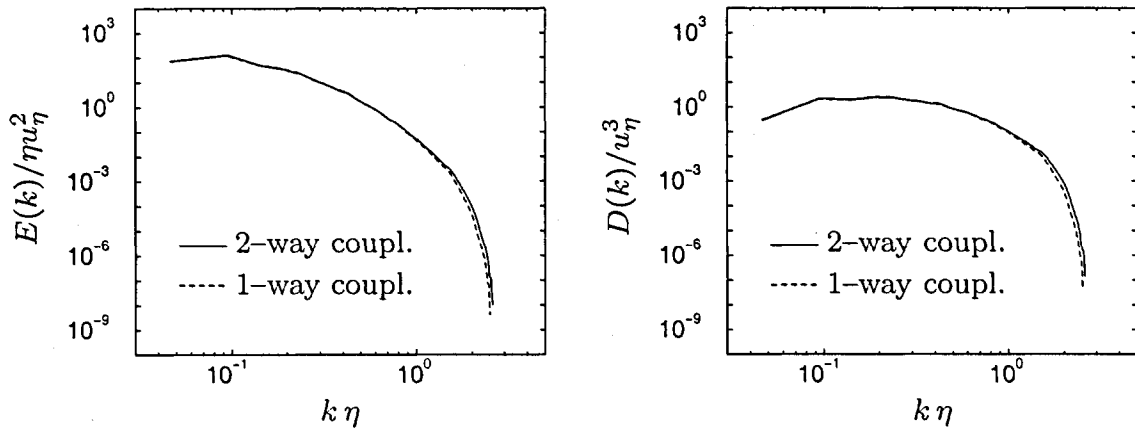


Figure 4.16: Three-dimensional energy spectra (left) and dissipation spectra (right) for  $\Phi_v = 1.5 \cdot 10^{-5}$  in the case of one-way and two-way coupling.

$\Phi_v$	$4.5 \cdot 10^{-5}$	$6.8 \cdot 10^{-5}$	$9.0 \cdot 10^{-5}$
$\nu$	0.215	0.198	0.154
$N$	72	72	96
$Re_\lambda$	42.5	41.5	41.9
$k_{max}\eta$	1.30	1.29	1.36
$\Delta V_3/U_p$	0.975	1.258	1.514
$\Delta V_3/u'$	0.346	0.459	0.566

Table 4.2: Data of simulations with fixed  $Re_\lambda \approx 42$  in Fig. 4.18. The data corresponding to the dashed lines are given in Tab. 4.1.

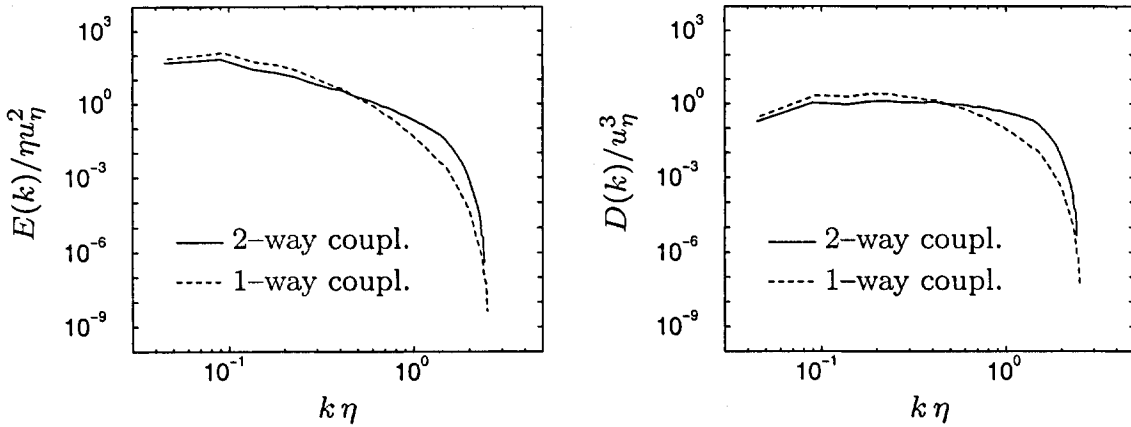


Figure 4.17: Three-dimensional energy spectra (left) and dissipation spectra (right) for  $\Phi_v = 1.5 \cdot 10^{-4}$  in the case of one-way and two-way coupling.

rameters were adjusted such that the resulting turbulence level remains at  $Re_\lambda \approx 42$ , whereas in the latter case the simulations were performed with fixed initial parameters (Tab. 4.2 contains the grid resolutions and viscosities for the additional simulations in Fig. 4.18). The particle settling velocity enhancement is found to increase with a roughly constant slope if the (resulting) microscale Reynolds number is kept constant. This result is in good agreement with the findings by Aliseda *et al.* (2002) (see their figure 16).

In order to understand the physical mechanism responsible for the particle settling velocity enhancement, the collective effect of the particles in regions of increased particle volume fraction needs to be analyzed. To this end the mean particle settling velocity conditioned to the regions of increased settling velocity will be compared for one-way and two-way coupling and different particle volume fractions. The same is done for the mean fluid velocity in these regions.

In the following the mean particle settling velocity averaged over the whole computational domain and over time is denoted by

$$V_3 := \overline{\langle v_3 \rangle}, \quad (4.5)$$

where the angle brackets indicate an average over all particles and the over-bar denotes a time average. Similarly, the mean particle settling velocity averaged over regions of a specific local particle volume fraction

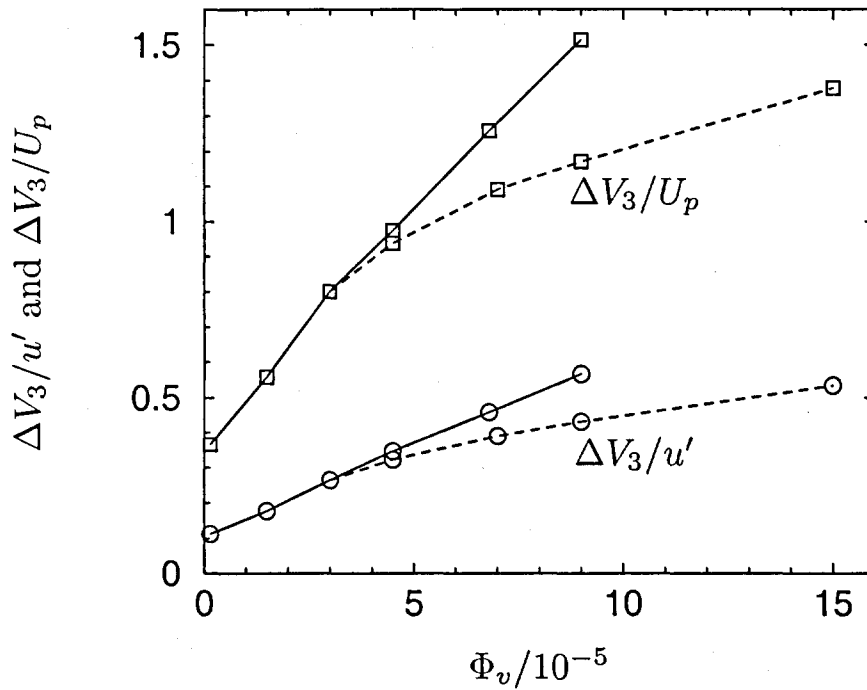


Figure 4.18: Particle settling velocity enhancement as a function of the particle volume fraction. Solid lines: Reynolds number remains fixed at  $Re_\lambda \approx 42$  (forcing parameters adjusted accordingly). Dashed lines: Reynolds number decreases due to turbulence modulation by the particles, same as shown in Fig. 4.10 (fixed initial parameters).  $St_\eta \approx 1.0$ ,  $U_p/u_\eta \approx 1.0$  in all cases.

is denoted by

$$V_3(\Phi_v^l) := \overline{\langle v_3(\Phi_v^l) \rangle}. \quad (4.6)$$

Fig. 4.19 shows the normalized difference of the conditioned mean particle settling velocity  $V_3(\Phi_v^l)$  to the overall mean settling velocity  $V_3$  for the simulations summarized in Tab. 4.1. Furthermore, the corresponding mean fluid velocity in  $x_3$ -direction in these regions of specific  $\Phi_v^l$  is shown in the bottom graph of Fig. 4.19 (note that  $\langle u_3 \rangle$ , i. e.  $u_3$  averaged over the entire domain, is zero per definitionem). As mentioned before, the number of sub-boxes in which the local quantities were computed is equal to the number of grid cells ( $N_b = N$ ). The normalized local particle concentration is only shown for a range up to  $\Phi_v^l/\Phi_v \approx 13$ . Although areas of even larger local particle concentration are found, their number of occurrences is rather small resulting in poor statistics. For this reason these very high local particle concentrations are excluded from Fig. 4.19.

We observe a monotonic increase in the conditioned settling veloc-

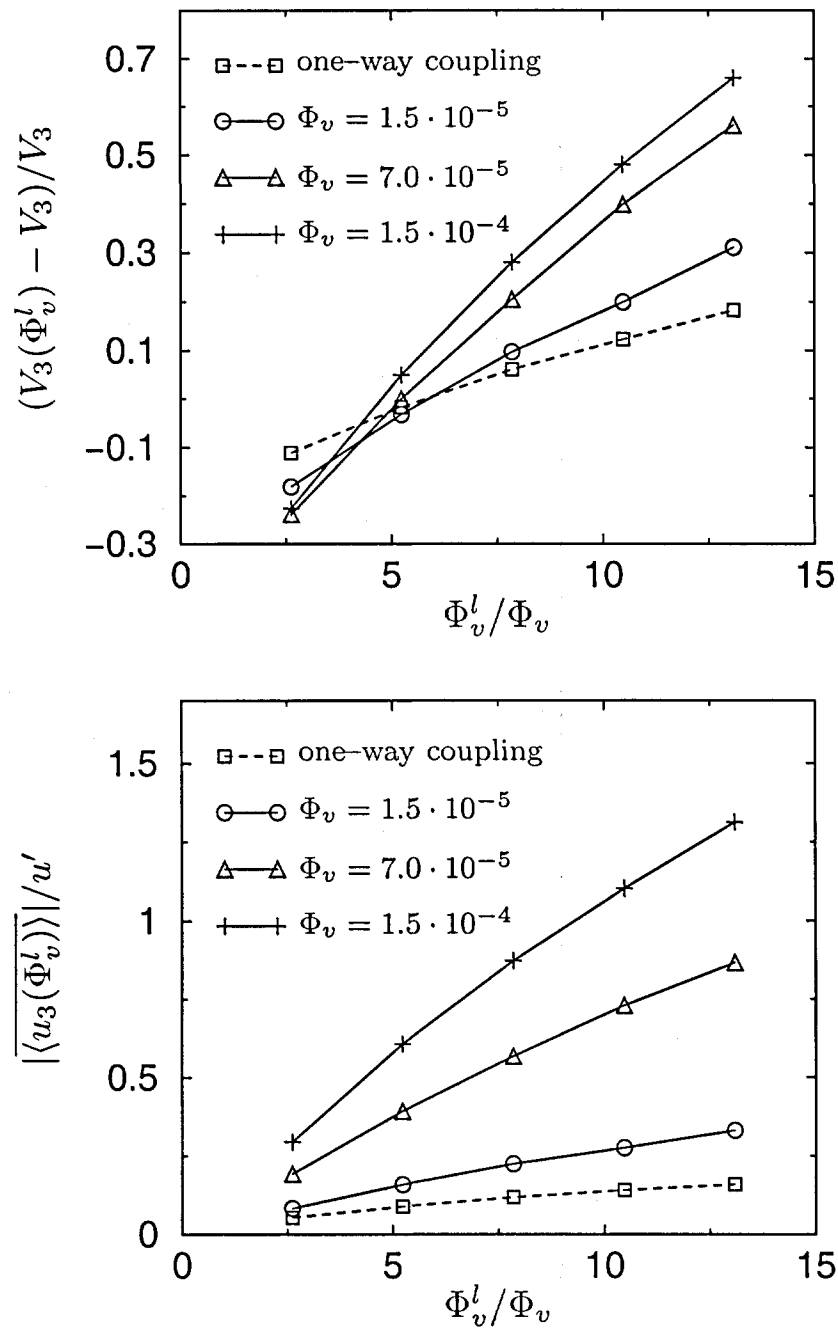


Figure 4.19: Top: Mean particle settling velocity averaged over regions of certain local particle volume fraction  $\Phi_v^l$  for different overall particle loadings  $\Phi_v$ . Bottom: Magnitude of the mean fluid velocity  $\langle u_3 \rangle$  in these regions. The dashed lines show the one-way coupled case for comparison.  $St_\eta \approx 1.0$ ,  $U_p/u_\eta \approx 1.0$  in all cases.  $Re_\lambda$  according to Tab. 4.1.

ity with increasing local particle volume fraction for both one-way and two-way coupling. However, this effect is much stronger in the case of two-way coupling and is enhanced with increasing overall particle volume fraction  $\Phi_v$ . Thus, in the case of two-way coupling we observe a collective effect of the particles in regions of high particle concentration resulting in an enhanced mean settling velocity in these regions. The accumulated particles – pulled downwards by gravity – exert a larger drag force on the surrounding fluid, which is more strongly accelerated in  $x_3$ -direction than in the one-way coupled case. This is seen in the bottom graph. Here, the magnitude of the mean fluid velocity  $|\langle u_3(\Phi_v^l) \rangle|$  averaged over regions of specific particle volume fraction  $\Phi_v^l$  is found to exhibit a similar monotonic increase due to the particle–fluid interaction (the fluid velocity  $u_3$  in all regions where particles are found is negative on average). Note that the curves for the particle velocity enhancement in the upper graph cross each other at  $\Phi_v^l/\Phi_v \approx 4$ . This is due to the normalization by the overall mean settling velocity  $V_3$ , which increases with increasing particle volume fraction  $\Phi_v$ . It indicates that the effect of the accumulated particles becomes more important with both growing local and overall particle concentration.

If the microscale Reynolds number  $Re_\lambda$  is kept constant as in Fig. 4.18 the qualitative behavior of the conditioned particle and fluid velocities remains the same as that in Fig. 4.19. However, the slopes of the curves for particle volume fractions  $\Phi_v \gtrsim 3.0 \cdot 10^{-5}$  are a little steeper than in Fig. 4.19.

The mechanism responsible for the particle velocity enhancement in two-way coupled simulations can now be explained as the interplay of three contributing effects. The first one is the well-known inertial bias by which the particles accumulate in regions of high-strain rate and low vorticity. If gravity is present the second effect, usually known as preferential sweeping, causes the particles to travel primarily towards regions of downward fluid motion on their way through the turbulent carrier fluid. This can also be observed in merely one-way coupled simulations. Finally, the third effect – only present in the case of two-way coupling – is a local modification of the fluid velocity structure by the particles in regions of increased particle volume fraction. The collective effect of the accumulated particles is a downward drag force on the carrier fluid. As a result the latter is additionally accelerated in direction of gravity compared to the one-way coupled case, which in turn causes the particle settling velocity to be enhanced in these regions of increased downward fluid

motion. In principle, this explanation is similar to the phenomenological model hypothesized by Aliseda *et al.* (2002). However, their model is based on the assumption of individual particle clusters acting as large pseudo-particles and settling at their own velocity  $V_{cl}$ , which adds to the mean settling velocity of an isolated particle in turbulence. According to Fig. 4.8 such individual clusters are not observed in our simulations, but the particles accumulate in rather coherent, web-like regions of low vorticity.

### 4.3 Comparison with experimental data

In the previous section it was shown that the mean particle settling velocity in homogeneous turbulence can be considerably increased due to a collective effect of the particles in regions of high particle concentration. In the following a quantitative comparison of these findings with experimental results in the literature will be performed. As mentioned in the introduction, the available data are very limited. We found only one study suitable for such direct comparisons: Aliseda *et al.* (2002) (hereafter referred to as AL) did experiments of heavy particles settling in homogeneous decaying turbulence. Their experimental facility was a wind tunnel, in which roughly spherical water droplets were seeded into grid-generated turbulence. They provide particle and turbulence statistics at two downstream locations of the wind tunnel ( $x \approx 100$  cm and  $x \approx 200$  cm) for different particle volume fractions and Stokes numbers. We chose the first,  $x \approx 100$  cm, for a comparison by matching the microscale Reynolds number in our simulations to  $Re_\lambda \approx 75$ . Table 4.3 shows the turbulence characteristics measured by AL at this location.

$u'$ (cm/s)	$\varepsilon$ ( $\text{m}^2/\text{s}^3$ )	$l_I$ (mm)	$\lambda$ (mm)	$\eta$ (mm)	$\tau_\eta$ (ms)	$u_\eta$ (cm/s)	$Re_\lambda$
21.1	1.00	43.0	5.37	0.241	3.87	6.23	75.54

Table 4.3: Turbulence characteristics of the experiment by Aliseda *et al.* (2002) at the wind tunnel downstream location  $x \approx 100$  cm;  $\nu = 1.5 \cdot 10^{-5} \text{ m}^2/\text{s}$ . (Data taken from their table 1.)

In a first set of simulations the mean particle settling velocity was investigated in a one-way coupled approach. Several Stokes numbers and corresponding dimensionless terminal settling velocities were studied

$St_\eta$	0.18	1.0	1.38	3.2
$U_p/u_\eta$	0.110	0.611	0.843	1.954

Table 4.4: Stokes numbers and corresponding dimensionless Stokes settling velocities for  $x \approx 100$  cm investigated by Aliseda et al. (2002).

according to Tab. 4.4. Fig. 4.20 and Tab. 4.5 show the increase in the mean particle settling velocity as a function of the Stokes number for both our simulations and the experiment (with the approximate values for  $\Phi_v = 1.5 \cdot 10^{-5}$  taken from the figure 14 of AL). It is obvious that one-way coupling between the liquid and dispersed phase is not sufficient to capture the underlying physics of the enhanced particle settling. The simulation results under-predict the experimental findings by almost an order of magnitude.

For the two-way coupled case two simulations with  $\Phi_v = 1.5 \cdot 10^{-5}$  and  $\Phi_v = 7.0 \cdot 10^{-5}$  were performed, which are also shown in Fig. 4.20 ( $Re_\lambda = 75$ ,  $St_\eta = 1$ ,  $U_p/u_\eta = 0.6$ ). In the first case we observe an increase in the particle settling velocity of roughly 30% compared to the one-way coupled case. However, the predicted velocity enhancement of  $\Delta V_3/u' \approx 0.1$  is still considerably smaller than the experimental result of  $\Delta V_3/u' \approx 0.26$ . If the particle volume fraction is augmented to  $\Phi_v = 7.0 \cdot 10^{-5}$  the settling velocity enhancement further increases as expected, but the discrepancy between experimental and numerical results is still observed (AL:  $\Delta V_3/u' \approx 0.46$  (not shown in Fig. 4.20), HIT:  $\Delta V_3/u' \approx 0.14$ ).

		$St_\eta$	0.18	1.0	1.38	3.2
AL		$\Delta V_3/u'$	0.125	0.26	0.27	0.21
HIT	1-way	$\Delta V_3/u'$	0.0086	0.081	0.080	0.073
		$\Delta V_3/U_p$	0.34	0.56	0.37	0.16
	2-way	$\Delta V_3/u'$		0.104		
		$\Delta V_3/U_p$		0.732		

Table 4.5: Comparison of settling velocity enhancement with Aliseda et al. (2002). Experimental values taken from their figure 14 for  $Re_\lambda = 75$ ,  $\Phi_v = 1.5 \cdot 10^{-5}$ . Simulations done with a grid resolution of  $N = 128$ .

The discrepancy between simulations and experiment calls for a discussion of possible reasons. In the following we point out some differences

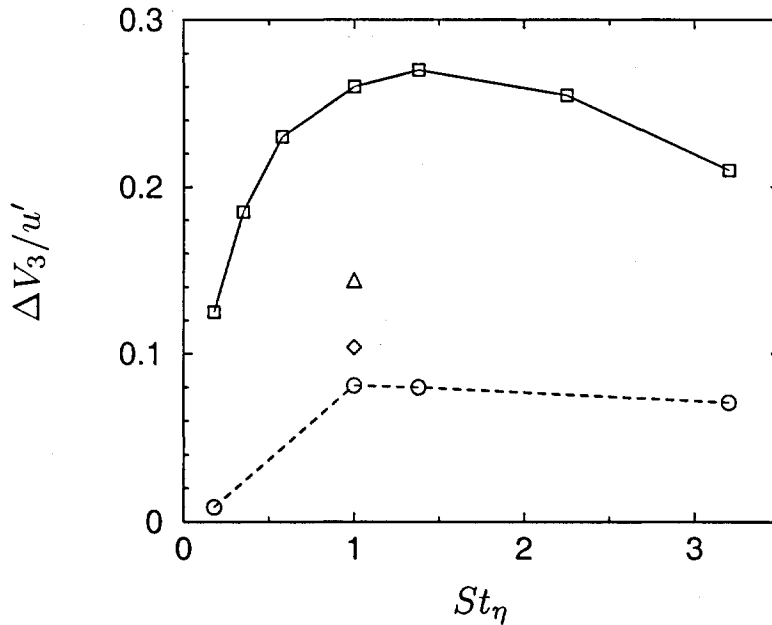


Figure 4.20: Increase in the mean particle settling velocity as a function of the Stokes number. Comparison of simulations with the experiment of AL for  $Re_\lambda = 75$ ; one-way coupled simulations (dashed lines); experiment AL,  $\Phi_v = 1.5 \cdot 10^{-5}$  (solid lines); two-way coupled simulations:  $\diamond \Phi_v = 1.5 \cdot 10^{-5}$ ,  $\triangle \Phi_v = 7.0 \cdot 10^{-5}$ .

between numerical and experimental conditions. In the experiment by AL the turbulent air stream in the wind tunnel was seeded with particles generated by an array of atomizers. The particle size was not uniform but spread over a range of diameters (figure 3 of AL displays the probability density function of the droplet diameters). Thus, particles with different Stokes numbers ranging from  $St_\eta \approx 0.01$  to  $St_\eta \approx 5.1$  were present in the flow. In the simulations, on the other hand, all particles had the same Stokes number. This may be the most important difference between experiment and simulation. However, confining the particles to a single size with  $St_\eta = 1$ , for which the strongest particle-fluid interaction can be expected, should increase the effect of settling velocity enhancement rather than decrease it. This makes the particle size distribution unlikely to be the reason for the observed discrepancies.

Even though the microscale Reynolds number in the simulation was matched to that in the experiment, other turbulence properties were found to be different. For example, from Tab. 4.3 the ratio of integral

length to Kolmogorov length can be formed, which is different from that in the simulation (AL:  $l_I/\eta \approx 180$ , HIT:  $l_I/\eta \approx 80$ ). The same applies to the ratio of Taylor microscale to Kolmogorov scale. However, given the results in the previous section for different Reynolds numbers, i. e. different turbulence “levels”, it is unlikely that these discrepancies make up for a difference in the particle settling velocity enhancement of more than 100% as found in the comparison between simulation and experiment (cf. Tab. 4.5).

In the simulations linear interpolation was used to compute both the fluid velocity at the particle positions and the particle feedback forces at the grid points. As already discussed in chapter 3 about settling suspension drops the influence of interpolation has been a subject of controversy in the literature. Several authors use high-order interpolation to compute the fluid velocities while considering low-order interpolation sufficient for the feedback forces (e. g. Ferrante & Elghobashi (2003)). Others report no significant differences in the results whether high-order or low-order interpolation is used to compute the fluid velocities (e. g. Squires & Eaton (1991b)). To assess the influence of fluid interpolation two simulations using spectral summation and fourth-order Lagrangian polynomials were performed and compared with corresponding simulations presented in the previous sections for one-way and two-way coupling, respectively. (Due to computational limitations we resort here to two representative simulations using smaller grid resolutions than required for a direct comparison with the simulations in Tab. 4.5, which were done on a  $128^3$ -grid.) As shown in Tab. 4.6 higher-order interpolation does make a difference in the results. In the case of two-way coupling the particle velocity enhancement is roughly 5% smaller if fourth-order polynomials are used instead of linear interpolation. In the previous section about the effects of two-way coupling on the particle settling this difference is acceptable, since we were primarily interested in demonstrating the principal mechanism of additional settling velocity increase compared to the one-way coupled case. In general, such a difference may be important when comparing with experimental results. However, even when assuming a worst case scenario with a difference of about 20% in the results using different interpolation techniques (as for one-way coupling and spectral summation, Tab. 4.6), this difference would not make up for the discrepancy in settling velocity found between the experiment of AL and our simulation. Thus, interpolation can also be excluded as a possible cause.

		LIN	SPE
(1-way)	$\Delta V_3/u_\eta$	0.155	0.125
		LIN	CUB
(2-way)	$\Delta V_3/u'$	0.177	0.168

Table 4.6: Particle velocity enhancement computed with different fluid interpolation methods (LIN: linear, CUB: 4th-order Lagrangian polynomials, SPE: spectral summation). One-way coupling:  $N = 32$ ,  $Re_\lambda = 21$ ,  $St_\eta = 1$ ,  $U_p/u_\eta = 1$ . Two-way coupling: run # 2 from Tab. 4.1.

As for the experimental conditions there is one remark to be made about the measurement of the mean particle settling velocity. It would be conceivable that the settling particles in the experiment induce a mean downward fluid velocity within the test region of the wind tunnel cross section. This mean downward fluid motion would be balanced by an upward motion near the tunnel walls outside the test region. Clearly, if measured with respect to the fixed laboratory system the particle settling velocity would be overestimated compared to the simulation if such mean downward fluid motion would be present in the wind tunnel experiment. It is emphasized that this reasoning is only speculative. Unfortunately, there is no explicit information given in the paper by AL as for a possible mean fluid flow induced by the drag of the particles.

The considerations above suggest that additional research is required to clarify the discrepancies between experiment and simulations. Even though some qualitative numerical findings are in very good agreement with the experimental results by Aliseda *et al.* (2002) (e.g. the roughly constant slope of the particle velocity enhancement with increasing local volume fraction  $\Phi_v^l$ , Fig. 4.19), the correct prediction of the mean particle settling velocity in a homogeneously turbulent carrier fluid remains an open question.<sup>1</sup> Future efforts should be driven by a close collaboration between experimentalist and numericist to ease the matching of numerical parameters to laboratory conditions.

<sup>1</sup>Shortly before this dissertation was completed new experimental findings of particles settling in homogeneous turbulence were published by Yang & Shy (2005). The mean particle settling velocities measured in their experiments are significantly smaller than those by Aliseda *et al.*. The numerical results of the present work lie somewhere in the range between these experimental findings.

Seite Leer /  
Blank leaf

# Chapter 5

---

## Summary and conclusions

Two configurations of disperse two-phase flows were numerically investigated with the aim of revealing some of the physics related to particle settling in suspensions. The first configuration was a suspension drop settling in an initially quiescent fluid under gravity, the second was a random particle suspension in homogeneous turbulence. In the simulations a pseudospectral method was employed to solve the governing fluid equations while the particles were modeled as point-masses that were individually tracked along their trajectories (Eulerian-Lagrangian approach).

The settling and break-up of suspension drops was studied with the focus on the physical processes affecting the instability and subsequent drop disintegration for moderate drop Reynolds numbers.

The case of low drop Reynolds numbers,  $Re_d \leq 0.1$ , was used for validation purposes. Here, the suspension drop retains a roughly spherical shape while settling under gravity. A few particles leak away into a tail emanating from the rear of the drop. The theoretical streamline pattern provided by Nitsche & Batchelor (1997) was very well reproduced in our simulations. Due to periodic boundaries in the pseudospectral method a hindered settling effect was observed: the drop settling velocity of a regular, three-dimensional array of suspension drops implied by our simulations may be considerably decreased compared with a single drop in infinite fluid. The settling velocity in the limiting case of vanishing drop volume concentration was found to be in good agreement with the result by Nitsche & Batchelor.

In the case of moderate drop Reynolds numbers,  $1 \leq Re_d \leq 100$ , the suspension drop deforms into a torus that eventually becomes unstable and breaks up into a number of secondary blobs. The particular way the torus breaks up is primarily determined by the drop Reynolds number and the distribution of the particles inside the drop and torus. With a fixed initial particle distribution an increasing Reynolds number leads to a larger number of secondary blobs. The deformation of the drop into a torus occurs at increasingly shorter times with increasing Reynolds number. The instability developing during the settling process was found to be very sensitive to the initial conditions, i. e. the initial distribution of

particles, the initial drop shape, and the number of particles making up the suspension drop. In particular, the following observations were made: The random particle distribution was identified as the primary source of (natural) perturbations, which are crucial to the instability leading to torus break-up. Different initial particle positions affect the details of the disintegration process. They may even result in a different number of secondary blobs. If the number of real and/or computational particles is increased with otherwise fixed parameters, the particle distribution becomes more homogeneous. The natural perturbation level is decreased, which causes the settling torus to remain stable for a longer period of time and to break up into a larger number of secondary blobs. The crucial role of perturbations was further illustrated by initially perturbing the shape of the suspension drop. If the level of these artificial perturbations is large enough, a particular number of secondary blobs can be forced. To gain a deeper insight into the substructural effects leading to torus break-up, the particle field was analyzed from a spectral point of view. The time evolution of the Fourier coefficients in azimuthal direction of the torus associated with the local particle number density and the mean particle settling velocity was studied. The instability is characterized by exponentially growing modes associated with the wavenumbers in azimuthal direction. The fastest growing modes determine the number of secondary blobs obtained during break-up. The wavenumber selection, i. e. the onset of exponential growth with a certain mode predominating, was found to occur at an early stage during the torus formation long before the visible break-up sets in.

The settling of an initially **random particle suspension in homogeneous turbulence** was examined with the focus on the mean particle settling velocity. In the case of one-way coupling the study by Wang & Maxey (1993) was used for validation purposes. Compared to the terminal (Stokes) settling velocity of a single particle the mean settling rate of the particle suspension was found to be increased. This increase was most significant for particle Stokes numbers around unity and only little pronounced for either very small or very large Stokes numbers. The visualization of the particles in the turbulent carrier fluid revealed regions of strong particle accumulation. The particles were shown to concentrate preferably in areas of low vorticity. Due to their inertia they are swept towards the peripheries of individual eddies in the turbulent flow. These findings were all in very good agreement with the results by Wang & Maxey.

In the case of two-way coupling the mean particle settling velocity was analyzed for different particle volume fractions  $\Phi_v$ . The principal observation was an additional enhancement of the mean settling velocity compared to the one-way coupled case for volume fractions  $\Phi_v \gtrsim 10^{-5}$ . In regions of high concentration the particles exert a collective effect on the carrier fluid, by which the fluid is accelerated due to particle drag. The enhanced downward fluid motion, in turn, leads to a larger particle settling velocity in these regions, thus increasing the overall mean settling velocity. In the range of particle volume fractions studied,  $1.5 \cdot 10^{-6} \leq \Phi_v \leq 1.5 \cdot 10^{-4}$ , the settling velocity enhancement monotonically grows with growing volume fraction. If the microscale Reynolds number  $Re_\lambda$  is kept constant the increase has a constant slope to first approximation. These findings qualitatively agree with those by Aliseda *et al.* (2002). If the forcing parameters are kept constant throughout the simulations for different particle volume fractions, the settling velocity enhancement grows less strongly, in particular for volume fractions  $\Phi_v \gtrsim 3.0 \cdot 10^{-5}$ . This is paralleled by a reduction of the turbulence intensity due to the particle–fluid interaction. The overall effect of the particles on the turbulence is dissipative, i.e. the mean turbulent kinetic energy is reduced. The effect, however, is selective with respect to the energy spectrum: at high wavenumbers the energy (and dissipation rate) is increased whereas at low wavenumbers it is decreased. This is in accordance with results in the literature.

A careful quantitative comparison with experimental findings by Aliseda *et al.* (2002) was performed by matching the turbulence and particle parameters to those in the experiment ( $Re_\lambda = 75$ ,  $St_\eta = 1$ ,  $U_p/u_\eta = 0.6$ ,  $\varrho_p/\varrho = 1000$ ,  $\Phi_v = 1.5(7.0) \cdot 10^{-5}$ ). The particle settling velocity enhancement found for both particle volume fractions was considerably smaller than those reported by Aliseda *et al.*. Some possible reasons for this discrepancy were discussed. However, the determination of the correct mean particle settling velocity in a homogeneously turbulent carrier fluid and the underlying physics remain an open question and call for future investigations. A close collaboration between numericist and experimentalist would be desirable to facilitate an exact matching of numerical parameters and experimental conditions. In this respect an obvious lack of available data was found in the literature.

**Seite Leer /  
Blank leaf**

# Appendix A

---

## Time stepping procedure

In order to integrate Eqs. (2.2) and (2.24) in time, a second-order mixed Runge–Kutta Crank–Nicolson scheme (**RK3CN**) or a standard third-order Runge–Kutta scheme (**RK3**) was applied. Both time stepping procedures are outlined in the following using the dimensionless fluid momentum equation in Fourier space (see section 2.2.1),

$$\frac{d\hat{\mathbf{u}}_{\mathbf{k}}}{dt} = \underbrace{-\frac{1}{k^2} \left( \mathbf{k} \times \left( \mathbf{k} \times [\hat{\mathbf{s}}_{\mathbf{k}} + \hat{\mathbf{f}}_{\mathbf{k}}] \right) \right)}_{G(\hat{\mathbf{u}}_{\mathbf{k}})} - \underbrace{\frac{k^2}{Re} \hat{\mathbf{u}}_{\mathbf{k}}}_{L(\hat{\mathbf{u}}_{\mathbf{k}})} . \quad (\text{A.1})$$

### A.1 RK3CN scheme

The nonlinear and two-way coupling terms  $G(\hat{\mathbf{u}}_{\mathbf{k}})$  are discretized in a third-order Runge–Kutta scheme whereas the linear terms  $L(\hat{\mathbf{u}}_{\mathbf{k}})$  are implicitly integrated according to a second-order Crank–Nicolson scheme. At time  $t_n$  the discretized equation assumes the following general form:

$$\frac{\hat{\mathbf{u}}_{\mathbf{k}n}^{(m+1)} - \hat{\mathbf{u}}_{\mathbf{k}n}^{(m)}}{\Delta t_n} = a^{(m)} G(\hat{\mathbf{u}}_{\mathbf{k}n}^{(m)}) + b^{(m)} G(\hat{\mathbf{u}}_{\mathbf{k}n}^{(m-1)}) + (a^{(m)} + b^{(m)}) \frac{L(\hat{\mathbf{u}}_{\mathbf{k}n}^{(m+1)}) + L(\hat{\mathbf{u}}_{\mathbf{k}n}^{(m)})}{2} \quad (\text{A.2})$$

The superscript  $m$  indicates the substep ( $m = 1$  denotes the solution  $\hat{\mathbf{u}}_{\mathbf{k}n}$  at the current time step  $t_n$  and  $m = 4$  denotes the solution  $\hat{\mathbf{u}}_{\mathbf{k}(n+1)}$  at the new time step  $t_{n+1}$ ). The coefficients  $a^{(m)}$  and  $b^{(m)}$  are given in Tab. A.1.

Substituting for  $L(\hat{\mathbf{u}}_{\mathbf{k}n})$  in Eq. (A.2) and using the definition  $G_{\mathbf{k}n} := G(\hat{\mathbf{u}}_{\mathbf{k}n})$  yields the following equation for substep  $m$ :

$$\begin{aligned} \hat{\mathbf{u}}_{\mathbf{k}n}^{(m+1)} = & \frac{1}{1 + \frac{a^{(m)} + b^{(m)}}{2} \frac{\Delta t_n k^2}{Re}} \left[ \left( 1 - \frac{a^{(m)} + b^{(m)}}{2} \frac{\Delta t_n k^2}{Re} \right) \hat{\mathbf{u}}_{\mathbf{k}n}^{(m)} \right. \\ & \left. + \Delta t_n \left( a^{(m)} G_{\mathbf{k}n}^{(m)} + b^{(m)} G_{\mathbf{k}n}^{(m-1)} \right) \right] . \end{aligned} \quad (\text{A.3})$$

$m$	$a^{(m)}$	$b^{(m)}$
1	8/15	0
2	5/12	-17/60
3	3/4	-5/12

Table A.1: Coefficients for Runge–Kutta time integration.

By adequately combining terms on the right-hand side of Eq. (A.3), it is possible to work with only two storage levels for  $\hat{\mathbf{u}}_{kn}^{(m+1)}$ ,  $\hat{\mathbf{u}}_{kn}^{(m)}$ ,  $G_{kn}^{(m)}$ , and  $G_{kn}^{(m-1)}$ . For this reason RK3CN is called a low–storage scheme.

## A.2 RK3 scheme

As an alternative to the second–order RK3CN procedure a standard third–order Runge–Kutta scheme (RK3) can be applied to Eq. (A.1). The advantage of RK3 is an increased order of accuracy. However, the purely explicit discretization involves a generally smaller time step  $\Delta t_n$  leading to an increased computational time.

At time  $t_n$  the discretized momentum equation, Eq. (A.1), assumes the form

$$\frac{\hat{\mathbf{u}}_{kn}^{(m+1)} - \hat{\mathbf{u}}_{kn}^{(m)}}{\Delta t_n} = a^{(m)} \left( G(\hat{\mathbf{u}}_{kn}^{(m)}) + L(\hat{\mathbf{u}}_{kn}^{(m)}) \right) + b^{(m)} \left( G(\hat{\mathbf{u}}_{kn}^{(m-1)}) + L(\hat{\mathbf{u}}_{kn}^{(m-1)}) \right) \quad (A.4)$$

with the coefficients given in Tab. A.1. Substituting for  $L(\hat{\mathbf{u}}_{kn})$  in Eq. (A.4) yields for substep  $m$

$$\hat{\mathbf{u}}_{kn}^{(m+1)} = \hat{\mathbf{u}}_{kn}^{(m)} + \Delta t_n \left( a^{(m)} \left( G_{kn}^{(m)} - \frac{k^2}{Re} \hat{\mathbf{u}}_{kn}^{(m)} \right) + b^{(m)} \left( G_{kn}^{(m-1)} - \frac{k^2}{Re} \hat{\mathbf{u}}_{kn}^{(m-1)} \right) \right). \quad (A.5)$$

Here, three storage levels are needed corresponding to substeps  $m + 1$ ,  $m$ , and  $m - 1$ . Since both the nonlinear and linear terms are discretized explicitly, a low–storage scheme with only two storage levels is not feasible.

### A.3 Stability criterion for time step

Explicit time stepping procedures require a careful choice of the time step  $\Delta t$ . If the time step is taken too large, the numerical integration may become unstable. Since there is no rigorous stability theory available for Runge–Kutta schemes applied to the Navier–Stokes equations, a linearized model equation is used to gain an approximate stability criterion similar to a CFL number in a one-dimensional first-order upwind scheme (see Hirsch, 1988). A trial-and-error process is necessary to “tune” this stability criterion to the maximum time step possible without the numerical scheme becoming unstable.

For the linear model problem

$$\frac{dU}{dt} = \Omega U \quad (A.6)$$

with  $\Omega$  a complex constant, the stability properties of Runge–Kutta schemes are known. For third order, the stability region in the complex  $(\Omega\Delta t)$ -plane has the typical kidney shape including the imaginary axis from  $-i\sqrt{3}$  to  $i\sqrt{3}$  and the real axis from  $-2.78$  to  $0$  (Hirsch (1988), p. 447). A linear model equation that matches Eq. (A.6) is

$$\frac{\partial u}{\partial t} + \bar{u}_j \frac{\partial u}{\partial x_j} = -\frac{1}{Re} \frac{\partial^2 u}{\partial x_j \partial x_j}, \quad (A.7)$$

where  $\bar{u}_i = \max(||u_i||)$  is the maximum of the absolute value of the velocity component in direction  $i$  at the current time step. Assuming periodicity the Fourier transformation of each term in Eq. (A.7) yields

$$\frac{\partial \hat{u}_k}{\partial t} = - \underbrace{\left( i k_j \bar{u}_j + \frac{k^2}{Re} \right)}_{:=\Omega} \hat{u}_k. \quad (A.8)$$

with  $k := |\mathbf{k}|$ . To obtain an upper bound of the magnitude of  $\Omega$  we set

$$\Omega = - \left( i \cdot k_{max} (\bar{u}_1 + \bar{u}_2 + \bar{u}_3) + \frac{1}{Re} k_{max}^2 \right) \quad (A.9)$$

with  $k_{max} := \max(|\mathbf{k}|)$  the maximum magnitude of the wavenumber vectors.

In the case of **RK3CN** with the linear terms discretized implicitly, only the convective term (first term on the right-hand side of Eq. (A.9))

needs to be taken into account. Stability requires that  $\Omega\Delta t$  be inside the stability region in the complex  $\Omega\Delta t$  plane, i. e.

$$|\Omega| \Delta t = k_{max}(\bar{u}_1 + \bar{u}_2 + \bar{u}_3) \Delta t \leq \sqrt{3} , \quad (A.10)$$

or equivalently

$$\Delta t = \text{CFL} \cdot \frac{\sqrt{3}}{k_{max}(\bar{u}_1 + \bar{u}_2 + \bar{u}_3)} \quad (A.11)$$

with  $0 < \text{CFL} \leq 1$ .

In the case of **RK3** both the convective and linear terms need to be taken into account. Stability requires that

$$\Delta t = \text{CFL} \cdot \sqrt{\frac{3}{k_{max}^2(\bar{u}_1 + \bar{u}_2 + \bar{u}_3)^2 + \left(\frac{1}{Re} k_{max}^2\right)^2}} \quad (A.12)$$

with  $0 < \text{CFL} \leq 1$ . As can be seen by comparing Eqs (A.11) and (A.12) the explicit discretization of the linear terms results in a smaller time step  $\Delta t$ , especially if the Reynolds number  $Re$  is small.

Both stability criteria give only an estimate of the order of magnitude of the time step required for a stable time integration procedure. The actual choice of CFL has to be made empirically.

## Appendix B

---

### Interpolation

Interpolation is used in the Lagrangian point-particle model to compute both the fluid velocities at the instantaneous particle positions and the particle feedback forces at the grid points. In the simulations presented the top hat function or the tent function was used to distribute the particles' feedback forces to the grid points. For the evaluation of the fluid velocity at the particle positions trilinear interpolation, cubic Lagrange polynomials, and spectral summation were employed alternatively.

**Top hat function.** The top hat function is defined as

$$w_i^{(\square)}(\mathbf{x}) = \begin{cases} 1 & \text{if } -0.5 \Delta x_i \leq x_i \leq 0.5 \Delta x_i \\ 0 & \text{else} \end{cases} \quad (\text{B.1})$$

with  $\Delta x_i$  being the grid spacing in direction  $i$ . Thus, the top hat function defines the “area of influence” of a particle to be a volume equal to the grid cell volume with the particle located in the volume center. This is equivalent to attributing the full feedback force of particle  $j$  to the closest grid point in its vicinity.

**Tent function.** The tent function is defined as

$$w_i^{(\wedge)}(\mathbf{x}) = \begin{cases} 1 + x_i & \text{if } -\Delta x_i \leq x_i \leq 0 \\ 1 - x_i & \text{if } 0 \leq x_i \leq \Delta x_i \\ 0 & \text{else} \end{cases} \quad (\text{B.2})$$

The tent function covers an “area of influence” equal to eight grid cell volumes, in which the feedback force decreases linearly from the center to its boundary. This is equivalent to distributing the feedback force of particle  $j$  among the eight closest grid points in the particle’s vicinity.

**Linear Lagrange interpolation (LIN).** In each direction the fluid velocities are linearly interpolated between the two grid points adjacent to the instantaneous particle location. The corresponding Lagrange polynomial reads

$$P_{1,i}(\mathbf{x}) = (1 - \xi_i) y_{i,0} + \xi_i y_{i,1} \quad (\text{B.3})$$

with  $\xi_i = (x_i - x_{i,0})/\Delta x_i$ . The position vectors  $x_{i,0}$  and  $x_{i,1}$  denote the grid points adjacent to  $x_i$ , the function values  $y_{i,0}$  and  $y_{i,1}$  are the fluid velocities at these grid points.

**Cubic Lagrange interpolation (CUB).** Here, in each direction  $i$  the function values (velocities) given at the four grid points  $x_{i,j}$ ,  $j = 0, 1, 2, 3$ , closest to the location  $\mathbf{x}$  enter the Lagrange polynomial. The interpolation point (particle position) lies between  $x_{i,1}$  and  $x_{i,2}$ .

$$\begin{aligned}
 P_{3,i}(\mathbf{x}) &= \frac{1}{6}(-2\xi_i + 3\xi_i^2 - \xi_i^3) y_{i,0} \\
 &+ \frac{1}{2}(2 - \xi_i - 2\xi_i^2 + \xi_i^3) y_{i,1} \\
 &+ \frac{1}{2}(2\xi_i - 3\xi_i^2 - \xi_i^3) y_{i,2} \\
 &+ \frac{1}{6}(-\xi_i + \xi_i^3) y_{i,3}
 \end{aligned} \tag{B.4}$$

with  $\xi_i = (x_i - x_{i,1})/\Delta x_i$ .

**Spectral interpolation (SPE).** The fluid velocities are interpolated by evaluating the full Fourier series at the particle positions. This method is exact within the spectral resolution, i.e. any function that can be split into a series of sine- and cosine-functions with wavenumbers  $k_i \leq k_{i,max} = N_i/2 - 1$  is exactly represented on the entire domain (on and in between grid points). The fluid velocity is computed at the instantaneous particle position  $Y_i(t)$  according to Eq. (2.16) in section 2.2.1. Since the interpolated velocity  $u_i(\mathbf{x})$  is a real function, the complex Fourier coefficients  $\hat{u}_i(\mathbf{k})$  obey the relation  $\hat{u}_i(-\mathbf{k}) = \hat{u}_i^*(\mathbf{k})$ , where  $*$  denotes the complex conjugate. In this case the sum in Eq. (2.16) can be simplified to yield

$$\begin{aligned}
 u_i(\mathbf{x}) &= \Re[\hat{u}_i(\mathbf{0})] + i \Im[\hat{u}_i(\mathbf{0})] \\
 &+ 2 \cdot \sum_{k_i=1}^{\frac{N_i}{2}-1} (\Re[\hat{u}_i(\mathbf{k})] \cos(\mathbf{k} \cdot \mathbf{x}) + \Im[\hat{u}_i(\mathbf{k})] \sin(\mathbf{k} \cdot \mathbf{x})) \tag{B.5}
 \end{aligned}$$

where  $\Re[\cdot]$  and  $\Im[\cdot]$  denote the real and imaginary part, respectively.  $\Im[\hat{u}_i(\mathbf{0})]$  turns out to be zero, such that the interpolated velocity  $u_i(\mathbf{x})$  is purely real.

## Appendix C

---

### Determination of forcing parameters

Based on a simple model for the Navier–Stokes equations (for  $\hat{a}_k$  in Eq. (2.50)) Eswaran & Pope (1988) provide an estimation procedure to obtain a set of forcing input parameters for a desired resolution  $k_{max}\eta$  and a microscale Reynolds number  $Re_\lambda$ . The procedure is outlined in the following.

The forcing input parameters are

- $k_0$  and  $k_{max}$ , the smallest and largest wavenumber, respectively (given for a specified grid resolution),
- $\nu$ , the viscosity (to be specified),
- $\Delta t$ , the time step (given, equal to time step of time integration),
- $K_F$ , the upper limit of the forced wavenumber band (to be specified),
- $T_L$ , the forcing timescale (to be specified),
- and  $\varepsilon_L$  (to be specified).

To find appropriate values for the parameters that need to be specified the following steps are taken.

1. Specify the grid size  $N$  and obtain  $k_{max}$ .
2. Specify a desired resolution  $k_{max}\eta_T$  to obtain a minimum Kolmogorov length  $\eta_T$ .
3. Specify the viscosity (e.g.  $\nu = 0.025$ ) and compute the predicted dissipation rate  $\varepsilon_T = \nu^{3/4}/\eta_T^4$ .
4. Specify the desired (and realizable) Reynolds number  $Re_\lambda$  and compute the number of forced wavenumber vectors from  $N_F \approx (8.5/(\eta_T^{5/6} Re_\lambda))^{4.5}$ .
5. Find the wavenumber band radius  $K_F$  such that  $N_F$  is met as close as possible.

6. Specify  $T_L$  and compute the reference dissipation rate  $\varepsilon_L = \varepsilon_T(1 + T_L(N_F)^{1/3}/0.8)/(4N_f)$ .
7. Confirm a posteriori if these parameters yield the desired Reynolds number  $Re_\lambda$  and resolution  $k_{max}\eta$ .

For grid sizes of  $32^3$  and  $64^3$  grid points different input parameter sets are given in Eswaran & Pope (1988). For higher grid resolutions the input parameters have to be determined by the estimation procedure outlined above. Unfortunately, it was found that for higher grid resolutions this procedure does not always yield satisfactory parameter sets. Therefore, another simple and straightforward estimation procedure was applied, which is based on the extrapolation of the forcing parameters used by Wang & Maxey (1993), who also employed the ESPO scheme.

Wang & Maxey did simulations with up to  $96^3$  grid points. They used fixed parameters  $\varepsilon_L = 16.997$ ,  $T_L = 0.038$ , and  $K_F = \sqrt{2}$  and varied only the viscosity  $\nu$ . From their data we found that the relation between the viscosity and the number of grid points can be approximated by a powerlaw ( $\log \nu = \alpha \cdot \log N$  with  $\alpha = -1.333$  and  $\beta = 1.7847$ ). The powerlaw was then used to determine the viscosity for higher grid resolutions  $N = 128, 160$ , and  $192$ . Fig. C.1 shows the powerlaw in a log-log plot. The resolution of the turbulent flow generated with these parameters turned out to be  $k_{max}\eta \approx 1.25$  in all cases. The microscale Reynolds numbers obtained for the different grid resolutions are  $Re_\lambda = 82$  ( $N = 128$ ),  $Re_\lambda = 93$  ( $N = 160$ ), and  $Re_\lambda = 109$  ( $N = 192$ ).

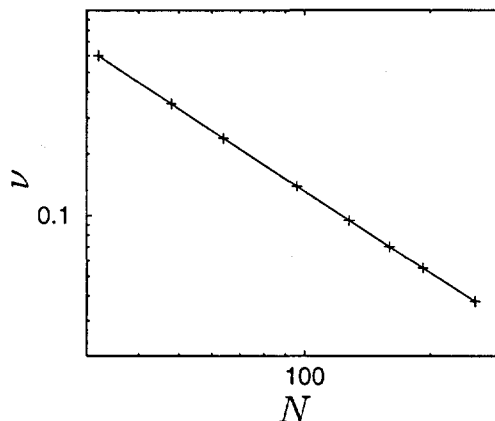


Figure C.1: Relation between the viscosity  $\nu$  and the number of grid points  $N$  for sufficiently resolved turbulence simulations ( $k_{max}\eta \approx 1.25$ ).

## Appendix D

---

### Definitions of turbulent quantities

The statistical quantities used to describe turbulent flow properties are briefly discussed in the following. For a detailed derivation of these quantities see e. g. Pope (2000) and Tennekes & Lumley (1972).

The smallest turbulent scales are characterized by the Kolmogorov length, velocity and time, respectively,

$$\eta = (\nu^3/\varepsilon)^{1/4} \quad (D.1)$$

$$u_\eta = (\varepsilon\nu)^{1/4} \quad (D.2)$$

$$t_\eta = (\nu/\varepsilon)^{1/2} \quad (D.3)$$

with  $\nu$  being the kinematic viscosity and  $\varepsilon$  the dissipation.

The turbulent kinetic energy is given by

$$q = \frac{1}{2} \overline{u_i u_i} = \int_0^\infty E(k) dk \quad (D.4)$$

with  $u_i$  being the velocity fluctuations,  $k = |\mathbf{k}|$  the magnitude of a wavenumber vector, and  $E(k)$  the three-dimensional power spectrum. The over-bar indicates an ensemble average. Assuming homogeneous and isotropic conditions this is equivalent to a spatial average. The energy content associated with shells of radius  $k$  in Fourier space is computed as

$$E(k) = \sum_{|\mathbf{k}| \in [k, k+dk]} \frac{|\hat{\mathbf{u}}(\mathbf{k}, t)|^2}{2}. \quad (D.5)$$

The turbulent kinetic energy can be split into three fractions according to the three velocity components. For example, in  $x_1$ -direction we have

$$q_1 = \frac{1}{2} \overline{u_1^2}, \quad (D.6)$$

such that

$$q = q_1 + q_2 + q_3 = 3q_1 = 3q_2 = 3q_3. \quad (D.7)$$

Here, the last three equalities only hold in perfectly isotropic turbulence. In numerical simulations the energy content will usually be different in different spatial directions.

The dissipation rate is defined as

$$\varepsilon = \nu \overline{\frac{\partial u_i}{\partial x_j} \frac{\partial u_i}{\partial x_j}} = \int_0^\infty D(k) dk = \int_0^\infty 2\nu k^2 E(k) dk \quad (\text{D.8})$$

with  $D(k)$  being the three-dimensional dissipation spectrum.

Large eddies are characterized by the eddy length scale  $l_e$ , the velocity scale  $u'$  and the eddy turnover time  $t_e$ . The root-mean-square (RMS) velocity is defined as

$$u' = u_{rms} = \left( \frac{1}{3} \overline{u'_i u'_i} \right)^{1/2} = \sqrt{\frac{2}{3}} q. \quad (\text{D.9})$$

The eddy length scale is defined as

$$l_e = \frac{u'^3}{\varepsilon}, \quad (\text{D.10})$$

and the eddy-turnover time is then given by

$$t_e = \frac{l_e}{u'} = \frac{u'^2}{\varepsilon}. \quad (\text{D.11})$$

As an alternative to characterize large-scale motion the integral length scale  $l_I$  is obtained from the three-dimensional energy spectrum,

$$l_I = \frac{\pi}{2 u'^2} \int_0^\infty \frac{E(k)}{k} dk. \quad (\text{D.12})$$

Accordingly, the integral time scale is

$$t_I = \frac{l_I}{u'}. \quad (\text{D.13})$$

Using the integral scales a turbulence Reynolds number can be defined as

$$Re_T = \frac{u' l_I}{\nu}. \quad (\text{D.14})$$

The Taylor microscale  $\lambda$  characterizes eddies of medium size and is used, together with  $u'$ , to form the Taylor microscale Reynolds number

$$Re_\lambda = \frac{u' \lambda}{\nu}. \quad (\text{D.15})$$

In homogeneous, isotropic turbulence Eq. (D.8) can be simplified using  $u'$  and  $\lambda$ :

$$\varepsilon = 15 \nu \frac{u'^2}{\lambda^2}. \quad (\text{D.16})$$

For comparisons with turbulence measurements it is advantageous to define one-dimensional spectra. The longitudinal spectrum in direction 1 is defined from

$$2 q_1 = \overline{u_1^2} =: \int_{-\infty}^{\infty} E_{11}(k_1) dk_1. \quad (\text{D.17})$$

Accordingly, longitudinal spectra  $E_{22}(k_2)$  and  $E_{33}(k_3)$  can be defined for the other two directions. Again, in perfectly isotropic conditions we have

$$E_{11}(k_1) = E_{22}(k_2) = E_{33}(k_3), \quad (\text{D.18})$$

such that

$$q = \sum_i q_i = \frac{3}{2} \int_{-\infty}^{\infty} E_{11}(k_1) dk_1. \quad (\text{D.19})$$

The energy content associated with  $E_{11}(k_1)$  can be computed in Fourier space according to

$$E_{11}(k_1) = \overline{|\hat{u}_1(k_1)|^2}^{23}, \quad (\text{D.20})$$

where the over-bar  $\overline{(\cdot)}^{23}$  denotes an average over directions 2 and 3 in Fourier space. Accordingly, we have

$$E_{22}(k_2) = \overline{|\hat{u}_2(k_2)|^2}^{13} \quad \text{and} \quad E_{33}(k_3) = \overline{|\hat{u}_3(k_3)|^2}^{12}. \quad (\text{D.21})$$

In the computer code HIT developed for this dissertation the above definitions are used to compute various turbulent quantities.

Seite Leer /  
Blank leaf

## Appendix E

---

### Settling of single particles

The parametric particle equation of motion, Eq. (2.5), requires the fluid velocity  $u_i$  to be known at the instantaneous particle location  $Y_i(t)$ . The fluid velocity  $u_i$  is that of the *undisturbed* flow field, i. e. the velocity at the particle position in a flow field with the particle *not* present, but under otherwise identical conditions (cf. Maxey & Riley (1983)). In a simulation with two-way coupling this velocity is not available since every particle exerts a feedback force onto the fluid, which modifies the fluid velocity field. As an approximation for the fluid velocity of the undisturbed flow field, the velocity of the disturbed flow field interpolated onto the particle position is commonly used in two-way coupled simulations. Therefore, independently of the accuracy of the interpolation technique employed, the fluid velocity  $u_i$  contains a self-induced, erroneous contribution (hereafter referred to as the “parasitic error”).

The Lagrangian point-particle model was originally designed for the simulation of dilute particle suspensions, in which the particles are much smaller than the smallest relevant scales of the fluid motion (see e. g. Crowe *et al.* (1977)). The two-way coupling regime is the specific situation where the collective effect of the particles involves a modification of the flow characteristics, whereas an individual particle has a negligible influence on the fluid flow. Thus, the point-particle model with two-way coupling has primarily been employed in simulations with large numbers of particles. It is clear that the influence of the parasitic error is decreased the more particles are used in the simulation, because the contribution of an individual particle to the disturbed flow field decreases compared with the contribution of all other particles.

However, even in simulations with large numbers of particles there may be regions where the particle concentration is very low. For example, several studies have revealed that in a turbulent flow small, heavy particles accumulate in regions of low vorticity and high pressure (see e. g. Wang & Maxey (1993), Truesdell & Elghobashi (1993), Eaton & Fessler (1994), section 4.1 in this dissertation). In regions of low particle concentration the parasitic error may become important. Therefore, as a preliminary study, we examined the settling velocity of a single particle in still fluid in a two-way coupled simulation. In this limiting case the

particle is expected to settle at the Stokes settling velocity

$$U_p = |v_3(u_i = 0, t \rightarrow \infty)| = \tau_p g \left(1 - \frac{\varrho}{\varrho_p}\right), \quad (\text{E.1})$$

where  $\tau_p = m_p / 6\pi\mu r$  is the particle response time.

The situation of a single spherical particle settling in a fluid under gravity is entirely defined by five quantities. The fluid is characterized by its density  $\varrho$  and the dynamic viscosity  $\mu$  and the particle is described by its density  $\varrho_p$  and its radius  $r$  (or, alternatively, by its mass and its volume). The gravitational constant  $g$  defines the acceleration due to gravity. According to the Buckingham  $\Pi$  Theorem we can derive two dimensionless parameters sufficiently characterizing the flow problem. We choose these to be the particle Reynolds number

$$Re_p = \frac{U_p r}{\nu}, \quad (\text{E.2})$$

(cf. Eq. (2.33)) and the particle Stokes number

$$St_p = \frac{\tau_p U_p}{r} = \frac{2}{9} \frac{\varrho_p}{\varrho} Re_p. \quad (\text{E.3})$$

From these a particle Froude number can be derived yielding

$$Fr_p = \sqrt{\frac{2}{9} \left( \frac{\varrho_p}{\varrho} - 1 \right) Re_p}. \quad (\text{E.4})$$

To non-dimensionalize the governing equations as explained in section 2.1 we choose the reference quantities  $U_{ref} = U_p$  and  $L_{ref} = r$  such that

$$Re = Re_p, \quad St = St_p, \quad Fr = Fr_p. \quad (\text{E.5})$$

Due to the implementation of the two-way coupling term (Eq. (2.27)) there is an additional (numerical) parameter to be specified. The feedback force of the particle is distributed to the surrounding grid points by some interpolation technique (top hat or tent interpolation, see Appendix B). Thus, the ratio of the particle radius to the grid spacing  $r/\Delta x$  defines an “area of influence” of the particle. For example, one and the same particle can be simulated using either a  $32^3$  grid or a  $64^3$  grid. In the second case the particle feedback force is “smeared out” over a volume of only one eighth of that in the first case (assuming tent

interpolation). As will be shown below the ratio  $r/\Delta x$  has a significant influence on the parasitic error.

To examine the influence of the Reynolds number  $Re_p$ , the Stokes number  $St_p$ , and the ratio  $r/\Delta x$  on the parasitic error, three sets of simulations were performed. In each set one of these parameters was varied over a representative range while the other two were kept constant. For the particle equation of motion, Eq. (2.5), to be valid the Reynolds number  $Re_p$  is required to be much smaller than unity. Also, the resulting density ratio  $\varrho_p/\varrho$  should be much larger than unity, but not unrealistically large ( $\max(\varrho_p/\varrho) \lesssim 5000$ ). Within these restrictions we chose  $0.001 \leq Re_p \leq 0.1$ ,  $0.1 \leq St_p \leq 10$ , and  $0.001 \leq r/\Delta x \leq 0.5$ . The simulations were done using the combined Runge–Kutta Crank–Nicolson (RK3CN) time integration scheme. The particle feedback force was computed using spectral interpolation of the fluid velocity and tent interpolation for the feedback force (see Appendix B).

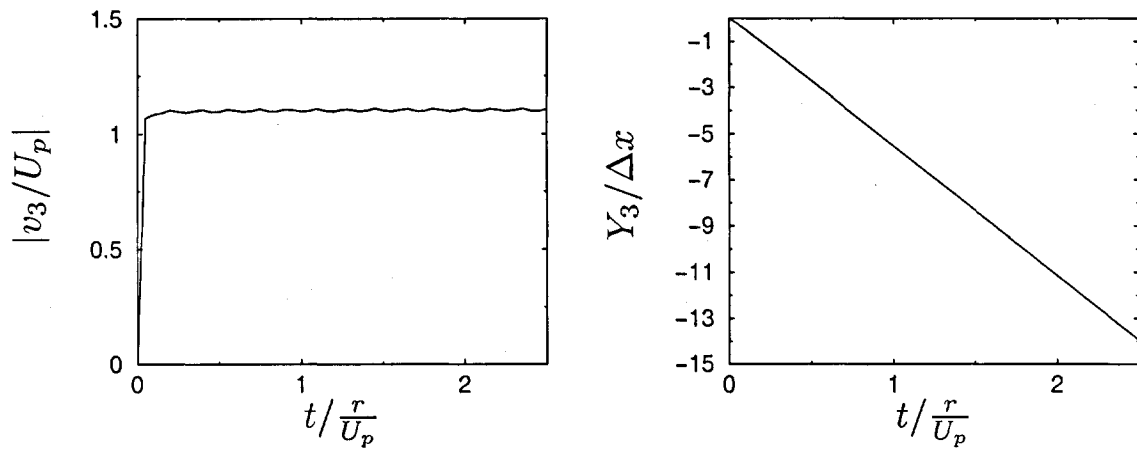


Figure E.1: Settling velocity (left) and distance (right) for a single particle falling under gravity.  $Re_p = 0.01$ ,  $St_p = 1$ ,  $r/\Delta x = 0.05$ . The settling distance has been normalized by the grid spacing to indicate the number of grid cells passed by the particle.

Fig. E.1 shows an example of the time evolution of the settling velocity and distance of a single particle falling under gravity ( $Re_p = 0.01$ ,  $St_p = 1$ ,  $r/\Delta x = 0.05$ ,  $N = 32$ ). The settling velocity experiences small fluctuations as seen in the left plot of the figure. Therefore, a quasi-stationary terminal settling velocity was computed as a time average after transient effects had died out, i.e. for  $1 \leq t/(r/U_p) \leq 2.5$ . The period of the fluctuations corresponds to the particle passing through

one grid cell. This can be seen by comparing the number of fluctuations over a period of time with the distance traveled by the particle during that period (right plot in Fig. E.1). The fluctuations are due to an interpolation error introduced by the tent interpolation (the spectral summation used to evaluate the fluid velocity at the particle position is accurate within the spectral resolution).

The computed settling velocities, together with the corresponding parameters, are given in Tables E.1, E.2, and E.3. The variation of  $Re_p$  and  $St_p$  do not show any influence on the parasitic error. The ratio  $r/\Delta x$ , however, has a significant effect. The parasitic error increases with increasing  $r/\Delta x$ . This relation is approximately linear within the parameter range investigated as shown in Fig. E.2. For example, the relative error  $(v_3 - U_p)/U_p$  is about 20% for  $r/\Delta x = 0.1$  and decreases to about 2% for  $r/\Delta x = 0.01$ . To keep the parasitic error below 1 % the ratio  $r/\Delta x$  should be less than about 0.005. In all subsequent simulations of suspension drops and particles in homogeneous turbulence this restriction was imposed whenever possible. It is emphasized however, as mentioned above, that the parasitic error decreases if the number of particles is enlarged. Hence, the error associated with a single settling particle is a worst case scenario and a ratio  $r/\Delta x > 0.005$  may still yield reliable results.

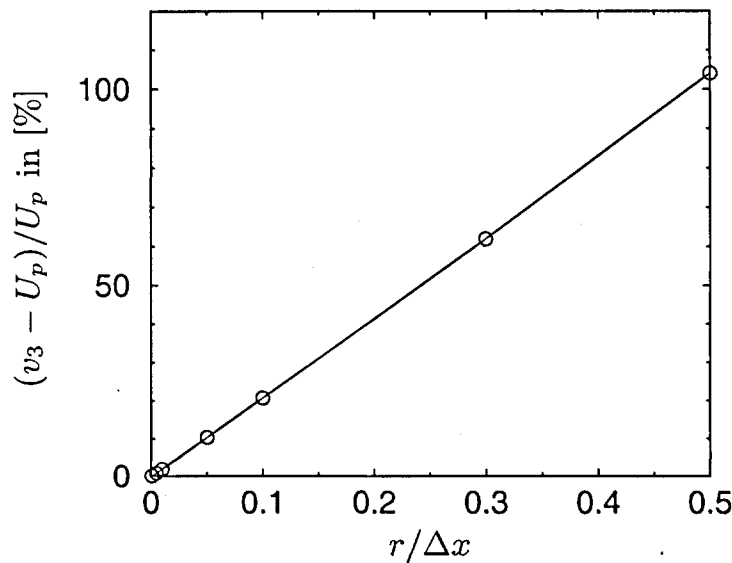


Figure E.2: Parasitic error (in percent) as a function of the ratio of particle radius to grid spacing  $r/\Delta x$ . Data from Tab. E.3.

$St_p$	10	1	0.1	$St_p$	10	1	0.1
$Re_p$		0.1		$Re_p$		0.1	
$Fr_p$	3.162	0.999	0.313	$Fr_p$	3.162	0.999	0.313
$r/\Delta x$		0.05		$r/\Delta x$		0.005	
$\varrho_p/\varrho$	4500	450	45	$\varrho_p/\varrho$	4500	450	45
$ v_3/U_p $	1.103	1.103	1.103	$ v_3/U_p $	1.008	1.008	1.008

Table E.1: Variation of the Stokes number with fixed  $Re_p = 0.1$ . Left:  $r_p/\Delta x = 0.05$ ; right:  $r_p/\Delta x = 0.005$ .

$Re_p$	0.1	0.01	0.001	$Re_p$	0.1	0.01	0.001
$St_p$		1		$St_p$		1	
$Fr_p$		0.999		$Fr_p$		0.999	
$r/\Delta x$		0.05		$r/\Delta x$		0.005	
$\varrho_p/\varrho$	45	450	4500	$\varrho_p/\varrho$	45	450	4500
$ v_3/U_p $	1.078	1.103	1.104	$ v_3/U_p $	1.002	1.008	1.010

Table E.2: Variation of the particle Reynolds number with fixed  $St_p = 1$ . Left:  $r_p/\Delta x = 0.05$ ; right:  $r_p/\Delta x = 0.005$ .

$r_p/\Delta x$	0.5	0.3	0.1	0.05	0.01	0.005	0.001
$Re_p$				0.01			
$St_p$					1		
$Fr_p$						0.999	
$\varrho_p/\varrho$							450
$ v_3/U_p $	2.041	1.620	1.207	1.103	1.018	1.008	1.001

Table E.3: Variation of the ratio  $r_p/\Delta x$  with fixed  $Re_p = 0.01$  and  $St_p = 1$ .

The identification of the ratio  $r/\Delta x$  as the crucial parameter affecting the parasitic error is in accordance with a theoretical argument by Boivin *et al.* (1998). They did simulations of turbulence modification by particles using the same Lagrangian point-particle model as in this dissertation. Their estimate of the parasitic error is based on the analytical

expression for the fluid velocity around a single particle in Stokes flow given by Saffman (1973),

$$u_i = \tilde{u}_i + \frac{3d}{4|r|} \left[ w_i + w_j \frac{r_i r_j}{|r|^2} \right]. \quad (\text{E.6})$$

Here,  $\tilde{u}_i$  is the velocity of the undisturbed flow,  $d$  is the particle diameter, the vector  $r_i = x_i - Y_i$  denotes the radial distance from the particle's center and  $w_i = v_i - \tilde{u}_i$  is the velocity difference between the particle and the undisturbed flow field. The second term on the right-hand side of Eq. (E.6) is called a Stokeslet and is identified by Boivin *et al.* as the error  $u_i - \tilde{u}_i$  introduced if the velocity of the disturbed flow  $u_i$  is used in the computation of the Stokes drag term instead of the velocity of the undisturbed flow  $\tilde{u}_i$ . In the simulation the distance  $|r|$  between the particle and the grid nodes is of the order of  $d/\Delta x$ . Thus, in order to keep the error small, the particle diameter should be much smaller than the grid spacing according to the reasoning of Boivin *et al.*. It should be noted, however, that due to the implementation of the two-way coupling the Stokeslet in Eq. (E.6) does not enter the actual computation of the fluid velocities in the simulations. Here, the reasoning of Boivin *et al.* is not consistent, which thus emphasizes the need to examine the influence of the different parameters on the parasitic error as discussed above.

## Bibliography

---

AIDUN, C. K. & LU, Y.-N. 1995 Lattice Boltzmann simulation of solid particles suspended in fluid. *J. Stat. Phys.* **81**, 49–61.

ALISEDA, A., CARTELLIER, A., HAINAUX, F. & LASHERAS, J. C. 2002 Effect of preferential concentration on the settling velocity of heavy particles in homogeneous isotropic turbulence. *J. Fluid Mech.* **468**, 77–105.

BALACHANDAR, S. & MAXEY, M. R. 1989 Methods for evaluating fluid velocities in spectral simulations of turbulence. *J. Comput. Phys.* **83**, 96–125.

BAUMANN, N., JOSEPH, D. D., MOHR, P. & RENARDY, Y. 1992 Vortex rings of one fluid in another in free fall. *Phys. Fluids* **A4**, 567–580.

BEHREND, O. 1995 Solid–fluid boundaries in particle suspension simulations via the Lattice Boltzmann method. *Phys. Rev. E* **52**, 1164–1175.

BOIVIN, M., SIMONIN, O. & SQUIRES, K. D. 1998 Direct numerical simulation of turbulence modulation by particles in isotropic turbulence. *J. Fluid Mech.* **375**, 235–263.

BRADY, J. F. & BOSSIS, G. 1988 Stokesian dynamics. *Ann. Rev. Fluid Mech.* **20**, 111–57.

CANUTO, C., HUSSAINI, M. Y., QUARTERONI, A. & ZANG, T. A. 1988 *Spectral methods in fluid dynamics*. Springer, Berlin.

CHANDRASEKHAR, S. 1961 *Hydrodynamic and hydromagnetic stability*. Clarendon Press, Oxford.

CHEN, S. & DOOLEN, G. D. 1998 Lattice Boltzmann method for fluid flow. *Annu. Rev. Fluid Mech.* **30**, 329–364.

CLIFT, R., GRACE, J. R. & WEBER, E. 1978 *Bubbles, drops and particles*. Academic Press, New York.

CLIMENT, E. & MAXEY, M. R. 2003 Numerical simulation of random suspensions at finite Reynolds numbers. *Int. J. Multiphase Flow* **29**, 579–601.

CROWE, C. T., SHARMA, M. P. & STOCK, D. E. 1977 The particle-source-in-cell (PSI-cell) model for gas-droplet flows. *J. Fluids Eng.* **99**, 325–332.

CROWE, C. T., SOMMERFELD, M. & TSUJI, Y. 1998 *Multiphase Flows with Droplets and Particles*. CRC Press LLC, Boca Raton.

CSANADY, G. T. 1963 Turbulent diffusion of heavy particles in the atmosphere. *J. Atmos. Sci.* **20**, 201–208.

DANCE, S. L. & MAXEY, M. R. 2003 Incorporation of lubrication effects into the force-coupling method for particulate two-phase flow. *J. Comput. Phys.* **189**, 212–238.

DREW, D. A. 1983 Mathematical modeling of two-phase flow. *Ann. Rev. Fluid Mech.* **15**, 216–291.

DREW, D. A. & LAHEY JR, R. T. 1993 *Particulate Two-phase Flow*, chap. Analytical modeling of multiphase flow, pp. 509–566. Butterworth-Heinemann, Oxford.

DRUZHININ, O. A. & ELGHOBASHI, S. 1999 On the decay rate of isotropic turbulence laden with microparticles. *Phys. Fluids* **11**, 602–610.

DURLOWSKY, L. J. & BRADY, J. F. 1989 Dynamic simulation of bounded suspensions of hydrodynamically interacting particles. *J. Fluid Mech.* **200**, 39–67.

EATON, J. K. & FESSLER, J. R. 1994 Preferential concentration of particles by turbulence. *Int. J. Multiphase Flow* **20**, 169–209.

ELGHOBASHI, S. 1994 On predicting particle-laden turbulent flows. *Appl. Sci. Res.* **52**, 309–329.

ELGHOBASHI, S. 2000 On the two-fluid and trajectory approaches for DNS of turbulent particle-laden flows. Part II: On the approximation of the two-way coupling terms in the trajectory approach. In *Theoretical and experimental modelling of particulate flow* (ed. J.-M. Buchlin), *VKI Lecture Series*, vol. 6.

ELGHOBASHI, S. & DRUZHININ, O. A. 1998 Direct numerical simulations of bubble-laden turbulent flows using the two-fluid formulation. *Phys. Fluids* **10**, 685–697.

ELGHOBASHI, S. & TRUESDELL, G. C. 1992 Direct simulation of particle dispersion in a decaying isotropic turbulence. *J. Fluid Mech.* **242**, 655–700.

ELGHOBASHI, S. & TRUESDELL, G. C. 1993 On the two-way interaction between homogeneous turbulence and dispersed solid particles. I: Turbulence modification. *Phys. Fluids* **A5**, 1790–1801.

ESWARAN, V. & POPE, S. B. 1988 An examination of forcing in direct numerical simulations of turbulence. *Comp. Fluids* **16**, 257–278.

FALLON, T. & ROGERS, C. B. 2002 Turbulence-induced preferential concentration of solid particles in microgravity conditions. *Exp. Fluids* **33**, 233–241.

FERRANTE, A. & ELGHOBASHI, S. 2003 On the physical mechanisms of two-way coupling in particle-laden isotropic turbulence. *Phys. Fluids* **15**, 315–329.

FERRY, J. & BALACHANDAR, S. 2001 A fast Eulerian method for disperse two-phase flow. *Int. J. Multiphase Flow* **27**, 1199–1226.

FERRY, J., RANI, S. L. & BALACHANDAR, S. 2003 A locally implicit improvement of the equilibrium Eulerian method. *Int. J. Multiphase Flow* **29**, 869–891.

GLOWINSKI, R. 2003 Finite element methods for incompressible viscous flow. In *Handbook of numerical analysis* (ed. P. G. Ciarlet & J. L. Lions), chap. 8 and 9. North-Holland, Amsterdam.

GLOWINSKI, R., PAN, T. W., HESLA, T. I., JOSEPH, D. D. & PERIAUX, J. 2001 A fictitious domain approach to the direct numerical simulation of incompressible viscous flow past moving rigid bodies: Application to particulate flow. *J. Comput. Phys.* **169**, 363–426.

HÄRTEL, C. 2001 Model analysis of aspects of the flow field ahead of a density current. *Eur. J. Mech. B/Fluids* **20**, 415–425.

HÄRTEL, C., CARLSSON, F. & THUNBLOM, M. 2000a Analysis and direct numerical simulation of the flow at a gravity-current head. Part 2. The lobe-and-cleft instability. *J. Fluid Mech.* **418**, 213–229.

HÄRTEL, C., MEIBURG, E. & NECKER, F. 2000b Analysis and direct numerical simulation of the flow at a gravity-current head. Part 1. Flow topology and front speed for slip and no-slip boundaries. *J. Fluid Mech.* **418**, 189–212.

HASIMOTO, H. 1959 On the periodic fundamental solutions of the Stokes equations and their application to viscous flow past a cubic array of spheres. *J. Fluid Mech.* **5**, 317–328.

HIRSCH, C. 1988 *Numerical computation of internal and external flows*. J. Wiley, New York.

HU, H. H. 1996 Direct simulation of flows of solid–liquid mixtures. *Int. J. Multiphase Flow* **22**, 335–352.

HU, H. H., PATANKAR, N. A. & ZHU, M. Y. 2001 Direct numerical simulations of fluid–solid systems using the arbitrary Lagrangian–Eulerian technique. *J. Comput. Phys.* **169**, 427–462.

HUNT, J. C. R., BUELL, J. C. & WRAY, A. A. 1987 Big whorls carry little whorls. *Stanford Univ. Proc. of the Summer Program 1987* pp. 77–94.

JOSEPH, D. D. & RENARDY, Y. Y. 1993 *Fundamentals of two-fluid dynamics, vol. II*, chap. IX. Springer, Berlin.

KERR, R. M. 1985 Higher-order derivative correlations and the alignment of small-scale structures in isotropic numerical turbulence. *J. Fluid Mech.* **153**, 31–58.

KITAGAWA, A., MURAI, Y. & YAMAMOTO, F. 2001 Two-way coupling of Eulerian–Lagrangian model for dispersed multiphase flows using filtering functions. *J. Multiphase Flow* **27**, 2129–2153.

KOH, C. J. & LEAL, L. G. 1989 The stability of drop shapes for translation at zero Reynolds number through quiescent fluid. *Phys. Fluids* **A1**, 1309–1313.

KOHNEN, G., RÜGER, M. & SOMMERFELD, M. 1994 Convergence behavior for numerical calculations by the Euler/Lagrange method for strongly coupled phases. *ASME FED* **185**, 191–202.

KOJIMA, M., HINCH, E. J. & ACRIVOS, A. 1984 The formation and expansion of a toroidal drop moving in a viscous fluid. *Phys. Fluids* **27**, 19–32.

LADD, A. J. C. 1994a Numerical simulations of particulate suspensions via a discretized Boltzmann equation. Part 1: Theoretical foundations. *J. Fluid Mech.* **271**, 285–309.

LADD, A. J. C. 1994b Numerical simulations of particulate suspensions via a discretized Boltzmann equation. Part 2: Numerical results. *J. Fluid Mech.* **271**, 311–339.

LOMHOLT, S. & MAXEY, M. R. 2003 Force-coupling method for particulate two-phase flow: Stokes flow. *J. Comput. Phys.* **184**, 381–405.

MACHU, G., MEILE, W., NITSCHE, L. C. & SCHAFLINGER, U. 2001 Coalescence, torus formation and breakup of sedimenting drops: experiments and simulations. *J. Fluid Mech.* **447**, 299–336.

MAXEY, M. R. 1987a The gravitational settling of aerosol particles in homogeneous turbulence and random flow fields. *J. Fluid Mech.* **174**, 441–465.

MAXEY, M. R. 1987b The motion of small spherical particles in a cellular flow field. *Phys. Fluids* **30**, 1915–1928.

MAXEY, M. R. & PATEL, B. K. 2001 Localized force representations for particles sedimenting in Stokes flow. *J. Multiphase Flow* **27**, 1603–1626.

MAXEY, M. R., PATEL, B. K., CHANG, E. J. & WANG, L.-P. 1997 Simulations of dispersed turbulent multiphase flow. *Fluid Dyn. Res.* **20**, 143–156.

MAXEY, M. R. & RILEY, J. J. 1983 Equation of motion for a small rigid sphere in a non-uniform flow. *Phys. Fluids* **26**, 883–889.

MICHAELIDES, E. E. 1997 Review – The transient equation of motion for particles, bubbles, and droplets. *J. Fluids Eng.* **119**, 233–246.

MO, G. & SANGANI, A. S. 1994 A method for computing Stokes flow interactions among spherical objects and its application to suspensions of drops and porous media. *Phys. Fluids* **6**, 1637–1652.

MURRAY, S. P. 1970 Settling velocities and vertical diffusion of particles in turbulent water. *J. Geophys. Res.* **75**, 1647–1658.

NECKER, F., HÄRTEL, C., KLEISER, L. & MEIBURG, E. 2002 High-resolution simulations of particle-driven gravity currents. *Int. J. Multiphase Flow* **28**, 279–300.

NECKER, F., HÄRTEL, C., KLEISER, L. & MEIBURG, E. 2003 Simulation of sedimentation and mixing in deeply-submerged gravity currents. In *Sedimentation and Sediment Transport* (ed. A. Gyr & W. Kinzelbach), pp. 195–200. Kluwer Academic Publishers, Dordrecht.

NITSCHE, J. M. & BATCHELOR, G. K. 1997 Break-up of a falling drop containing dispersed particles. *J. Fluid Mech.* **340**, 161–175.

ORSZAG, S. A. 1971 Numerical simulation of incompressible flows within simple boundaries: I. Galerkin (spectral) representations. *Stud. Appl. Math.* **50**, 293–327.

PAN, T. W., JOSEPH, D. D. & GLOWINSKI, R. 2001 Modelling Rayleigh–Taylor instability of a sedimenting suspension of several thousand circular particles in a direct numerical simulation. *J. Fluid Mech.* **434**, 23–37.

PARTHASARATHY, R. N. & FAETH, G. M. 1990 Turbulence modulation in homogeneous dilute particle-laden flows. *J. Fluid Mech.* **220**, 485–514.

PISMEN, L. M. & NIR, A. 1978 On the motion of suspended particles in stationary homogeneous turbulence. *J. Fluid Mech.* **84**, 193–206.

POPE, S. B. 2000 *Turbulent flows*. Cambridge Univ. Press, Cambridge.

POZRIKIDIS, C. 1990 The instability of a moving viscous drop. *J. Fluid Mech.* **210**, 1–21.

PROSPERETTI, A. 1997 Ensemble averaging techniques for disperse flow. In *Particulate flows: Processing and rheology* (ed. D. Drew, D. Joseph & S. L. Passman), pp. 99–136. Springer, Berlin.

RANI, S. L. & BALACHANDAR, S. 2004 Preferential concentration of particles in isotropic turbulence: a comparison of the Lagrangian and the equilibrium Eulerian approaches. *Powder Techn.* **141**, 109–118.

REEKS, M. W. 1977 On the dispersion of small particles suspended in an isotropic turbulent fluid. *J. Fluid Mech.* **83**, 529–546.

REEKS, M. W. 1991 On a kinetic equation for the transport of particles in turbulent flows. *Phys. Fluids* **A3**, 446–456.

RILEY, J. J. & PATTERSON, G. S. 1974 Diffusion experiments with numerically integrated isotropic turbulence. *Phys. Fluids* **17**, 292–297.

SAFFMAN, P. G. 1973 On the settling speed of free and fixed suspensions. *Stud. Appl. Math.* **LII** (2), 115–127.

SANGANI, A. S. 1987 Sedimentation in ordered emulsions of drops at low Reynolds numbers. *J. Appl. Math. Phys. (ZAMP)* **38**, 542–557.

SANGANI, A. S. & ACRIVOS, A. 1982 Slow flow through a periodic array of spheres. *Int. J. Multiphase Flow* **8**, 343–360.

SCHRECK, S. & KLEIS, S. J. 1993 Modification of grid-generated turbulence by solid particles. *J. Fluid Mech.* **249**, 665–688.

SCHUMANN, U., GRÖTZBACH, G. & KLEISER, L. 1980 Direct numerical simulation of turbulence. In *Prediction methods for turbulent flows* (ed. W. Kollmann), pp. 123–258. Hemisphere Publishing Corp., New York.

SHAN, X. & CHEN, H. 1993 A lattice Boltzmann model for simulating flows with multiple phases and components. *Phys. Rev. E* **47**, 1815–1819.

SIGGIA, E. D. & PATTERSON, G. S. 1978 Intermittency effects in a numerical simulation of stationary three-dimensional turbulence. *J. Fluid Mech.* **86**, 567–592.

SIMONIN, O., DEUTSCH, E. & MINIER, J. P. 1993 Eulerian prediction of the fluid/particle correlated motion in turbulent flows. *Appl. Sci. Res.* **51**, 275–283.

SNYDER, W. H. & LUMLEY, J. L. 1971 Some measurements of particle velocity autocorrelation functions in a turbulent flow. *J. Fluid Mech.* **48**, 41–71.

SQUIRES, K. D. & EATON, J. K. 1990 Particle response and turbulence modification in isotropic turbulence. *Phys. Fluids* **A2**, 1191–1203.

SQUIRES, K. D. & EATON, J. K. 1991a Measurements of particle dispersion obtained from direct numerical simulations of isotropic turbulence. *J. Fluid Mech.* **226**, 1–35.

SQUIRES, K. D. & EATON, J. K. 1991b Preferential concentration of particles by turbulence. *Phys. Fluids* **A 3**, 1169–1178.

STOKES, G. G. 1851 On the effect of the internal friction of fluids on the motion of pendulums. *Trans. Phil. Soc. Cambridge* **IX**, 8–106.

SUNDARAM, S. & COLLINS, L. R. 1999 A numerical study of the modulation of isotropic turbulence by suspended particles. *J. Fluid Mech.* **379**, 105–143.

TENNEKES, H. & LUMLEY, J. L. 1972 *A first course in turbulence*. MIT Press, Cambridge.

TRUESDELL, G. C. & ELGHOBASHI, S. 1993 On the two-way interaction between homogeneous turbulence and dispersed solid particles. II. Particle dispersion. *Phys. Fluids* **6**, 1405–1407.

WALTHER, J. H. & KOUMOUTSAKOS, P. 2001 Three-dimensional vortex methods for particle-laden flows with two-way coupling. *J. Comput. Phys.* **167**, 39–71.

WANG, L.-P. & MAXEY, M. R. 1993 Settling velocity and concentration distribution of heavy particles in homogeneous isotropic turbulence. *J. Mech. Fluids* **256**, 27–68.

WANG, L.-P. & STOCK, D. E. 1993 Dispersion of heavy particles by turbulent motion. *J. Atmos. Sci.* **50**, 1897–1913.

WELLS, M. R. & STOCK, D. E. 1983 The effect of crossing trajectories on the dispersion of particles in a turbulent flow. *J. Fluid Mech.* **136**, 31–62.

YANG, C. Y. & LEI, U. 1998 The role of the turbulent scales in the settling velocity of heavy particles in homogeneous isotropic turbulence. *J. Fluid Mech.* **371**, 179–205.

YANG, T. S. & SHY, S. S. 2005 Two-way interaction between solid particles and homogeneous air turbulence: particle settling rate and turbulence modification measurements. *J. Fluid Mech.* **526**, 171–216.

YEUNG, P. K. & POPE, S. B. 1988 An algorithm for tracking fluid particles in numerical simulations of homogeneous turbulence. *J. Comput. Phys.* **79**, 373–416.

YUDINE, M. I. 1959 Physical considerations on heavy-particle diffusion. *Adv. Geophys.* **6**, 185–191.

ZHANG, D. Z. & PROSPERETTI, A. 1997 Momentum and energy equations for disperse two-phase flows and their closure for dilute suspensions. *Int. J. Multiphase Flow* **23**, 425–453.

ZICK, A. A. & HOMSY, G. M. 1982 Stokes flow through periodic arrays of spheres. *J. Fluid Mech.* **115**, 13–26.

# Curriculum vitae

<b>Name</b>	Thorsten Bosse
<b>Date of birth</b>	March 2, 1973
<b>Place of birth</b>	Braunschweig, Germany
<b>Nationality</b>	German
<b>Feb. 2000 to Jan. 2005</b>	PhD student and research assistant under supervision of Prof. L. Kleiser at the Institute of Fluid Dynamics, ETH Zürch
<b>March 2002 to July 2002</b>	Visiting researcher in the group of Prof. E. Meiburg at UC Santa Barbara, CA, USA
<b>May 1999 to Nov. 1999</b>	Internship in the R&D department 'Vibrations' of Eurocopter, Marignane, France
<b>Oct. 1993 to Apr. 1999</b>	Undergraduate and graduate studies in Mechanical Engineering at the University of Karlsruhe, Germany
<b>June 1997 to Aug. 1997</b>	Internship at Daimler-Benz Research and Technology North America (RTNA), Palo Alto, CA, USA
<b>Aug. 1996 to May 1997</b>	Exchange student at the Department of Mechanical Engineering at the University of Massachusetts, Amherst, MA, USA
<b>Oct. 1992 to Sep. 1993</b>	Military service, Braunschweig
<b>May. 1992</b>	"Abitur" (graduation from high school), Wilhelm-Gymnasium, Braunschweig